Elastic Tunable Grating Powered by MEMS Actuators for Fluorescence Spectroscopy Applications

by

Steven C. Truxal

A dissertation submitted in partial fulfillment
of the requirements for the degree of
Doctor of Philosophy
(Mechanical Engineering)
in The University of Michigan
2009

Doctoral Committee:

Associate Professor Katsuo Kurabayashi, Chair
Associate Professor Shuichi Takayama
Assistant Professor Nikolaos Chronis
Assistant Professor Kenn Richard Oldham

To my grandfather, John Truxal.

Table of Contents

List of Figures

Figure

List of Appendices

Appendix

Abstract

In fields such as cell biology, fluorescent markers have become increasingly valuable tools for studying cellular interactions. Many of these tags have signature spectral emissions, and measuring light intensity as a function of wavelength allows the simultaneous use of multiple fluorescent tags to study multiple parameters. Unfortunately, fluorescent signals are often very weak. Researchers must employ complex and costly optical systems and photodetectors in order to measure different wavelengths separately. A need exists for a less complicated optical system capable of making the same types of measurements.

This research designs and implements a microelectromechanical system (MEMS) optical component to meet this challenge. A tunable optical grating is created by implementing elastomer-silicon hybrid MEMS technology. This method allows for polymer microstructures to be seamlessly integrated into silicon MEMS devices. The tunable grating is a suspended polymer microbridge that is elastically stretched by MEMS electrostatic actuators. The generated high strain dramatically changes the period of the grating pattern on the polymer bridge's top surface. The MEMS devices can displace over 50 μm to alter the grating period from 700 nm up to 820 nm. The devices can cycle this large range at speeds up to 2 kHz, a feat very difficult for other tunable grating technologies. This tuning of a submicron grating period at high strain and fast speeds creates the necessary tunable optical component needed for the fluorescence spectroscopy applications.

This work describes the design, fabrication, characterization, and implementation of this device. After characterization proving the device's utility, the MEMS optical component is paired with a single photomultiplier tube detector to take spectral measurements at fast speeds and high sensitivity. These components are then implemented as the detection system for a fluorescence microscope. Spectral flow

cytometry measurements are taken as a demonstration of applications. Fluorescent beads are run through a microfluidic channel, and the detection system takes spectral readings at kHz speed in order to distinguish beads by their spectral profile. The development of this MEMS device and its optical system can help several fields of research reduce the dependency on complex optics needed for high speed, highly sensitive fluorescent measurements.

Chapter I

Introduction

1.1 Research Introduction and Background

The field of spectroscopy plays a critical role in numerous fields of scientific research. Simply put, spectroscopy is the study of breaking up an optical signal into its wavelength components and measuring the intensity as a function of wavelength. The measuring of light in this manner can lead to valuable information about the source of the light emission. With numerous applications in fields such as astronomy, it has also been an important tool in chemistry and biology to identify a substance by analyzing the spectral profile either emitted or absorbed. In fields such as cell biology, fluorescent markers have become increasingly valuable tools for studying cellular environments as well as intercellular interactions. An essential part of this type of research is accurately measuring these fluorescent tags, not only their intensities but also the spectral profiles. As many of these fluorescent markers have signature spectral emissions, measuring peaks in intensity at particular wavelengths allows for simultaneous multianalyte measurements. The method of using multiple fluorescent tags each signifying a particular parameter of a cellular sample is vital for studying dependency between parameters. Obtaining this type of information is the key to fully understanding cellular responses and is the future for several fields of scientific research.

Several problems occur when dealing with these types of spectroscopy measurements. Often times fluorescent signals are very weak, and high sensitivity photodetectors are required. The most sensitive types of detectors are expensive and incapable of discriminating wavelength. In order to measure multiple wavelengths

simultaneously, researchers use a series of detectors, filters, and mirrors, with each detector responsible for measuring a certain range of wavelengths. This type of setup and other alternatives quickly become complex and costly. A need exists for a less complicated optical system that is capable of making the same type of measurements.

A substitute to having a series of multiple detectors is to implement tunable optical components that can manipulate and control the optical signal before detection. The components could direct the signal towards a single detector and vary the wavelength measured with time in order to take a spectral sweep of the signal. The grating which is responsible for diffracting the optical signal and separating wavelength components can be varied over time in order to change the wavelength incident onto the detector. The challenge of this technique is being able to tune the grating at appreciable speeds. Fast acquisition and high throughput are desired for many types of fluorescent measurements, and a full spectral measurement would only be as fast as the tuning of the grating.

A viable solution to these challenges is to implement microelectromechanical systems (MEMS). Created as a complement to integrated circuit (IC) computer chips, the field of MEMS encompasses the miniaturized movable components needed for sensors or small displacement actuations. The speed of tuning a macro-sized grating is limited by the inertia of the component. Miniaturizing down to the micro-scale reduces this limitation and allows for the high speed tuning required. Developed from the same fabrication processes of IC and complementary metal–oxide–semiconductor (CMOS) technology, most MEMS are made with silicon, silicon dioxide, thin metal layers, and other standard CMOS materials. These stiff and rigid materials are optimal in many cases, but often they are the limiting factor for large displacement and motion capabilities. The integration of flexible and elastic materials can yield new possibilities that transcend these limitations.

Because of these addressed applications and challenges, we have developed an elastic tunable optical grating operated by MEMS actuators. Using MEMS actuators is the solution to creating tunable optical components with the necessary high speeds, but traditional MEMS are too limiting in the movements needed for a large tuning range. The integration of elastic polymer microstructures with silicon MEMS can eliminate these limitations. The development of this type of MEMS device is the key to achieving

fluorescence spectroscopy measurements without dramatically increasing the complexity and cost of the optical system. To expand on this key idea, the following sections give a brief background the two main branches of this research, spectroscopy and polymer MEMS.

1.1.1 Fluorescence Spectroscopy

The phenomenon of fluorescence has been studied for over a century [1]. The emission of luminescence from a material is due to electrons of excited states falling to lower orbitals and creating emitted photons. The field of fluorescence spectroscopy is the study of measuring these fluorescence emissions. Spectroscopy measures the intensity of light as a function of the light's wavelength. Photodetectors are the transducers responsible for absorbing light and generating a measureable electrical signal. Most photodetectors are incapable of determining an optical signal's wavelength composition, and spectroscopy measurements require that the optical signal be separated by wavelength before detection. A standard spectrometer has several key components, with the most important ones being a dispersive element, a collimation element, and the detector [2]. Figure 1.1 illustrates the general layout of a spectroscopic device [3]. The dispersive element separates the optical signal spatially by wavelength so that the intensity of individual segments of the spectrum can be detected. The optical signal can leave through an exit slit in order for a narrow bandwidth of the spectrum to be measured, or a spatial detector such as charged-coupled device (CCD) camera with a pixilated array can detect a large range of the diffracted signal.

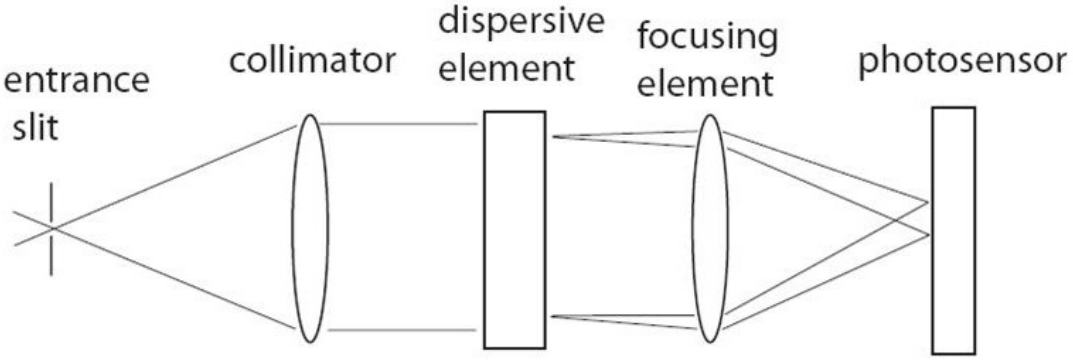

Figure 1.1: General components and layout of a spectroscopic device [3].

In recent years fluorescence spectroscopy has become valuable in biology applications for the simultaneous detection of multiple fluorescent markers in cellular samples [4-6]. More studies are finding that wavelength discrimination of multiple fluorescent color signatures is essential for multiplexed biological sensing, imaging, and diagnostics [7-12]. Detecting multiple wavelengths correlates to achieving simultaneous assays of a sample and generating more data for scientists to analyze and derive relationships between analyzed factors. These types of unique measurements have made fluorescence spectroscopy one of the primary tools for biochemistry, biophysics, cellular imaging, flow cytometry, as well as other disciplines [1].

1.1.2 Polymers within MEMS

The field of MEMS has substantially grown over the decades, and applications range from airbag deployment sensors in automobiles to high definition projectors and cell phone gyroscopes. The fabrication of MEMS devices typically involves using ultraviolet lithography to pattern silicon or other deposited materials to create movable structures through layers of processing. These structures have dimensions on the scale of microns, and the reduction in size allows for unique physical phenomena to become apparent. The movable structures can act as transducers to convert mechanical movement into electrical energy, or vice versa, and fundamental forces such as gravity and forces due to inertia are no longer dominant [13].

The further development of polymers integrated into microsystems is field of research with vast potential. Within the last decade polymers have become a much more attractive material within certain MEMS fields, and the research branch of polymer MEMS is increasing rapidly. Polymers and elastic materials hold promise to pave the way for a new wave of innovative transducers that exploit the pliability and manipulation of softer materials [14]. Compared to the more rigid inorganic CMOS materials, polymers can be mechanically compliant, more responsive, easily processed, potentially biocompatible and biodegradable, and often low cost. Polymer-based on-chip functional structures capable of high deformation and volume change in response to external stimuli are

attractive sources of new functionalities for biomimetic sensing and actuation [15-21]. However, sole use of these active polymer structures for practical devices still faces their shortcomings such as slow dynamic response, low actuation speed, or poor charged-carrier mobility [22-24]. Only through the integration of polymers with standard MEMS materials can the advantages of both types of materials be utilized and the disadvantages overcome.

1.2 Motivation for Research

The primary motivation of this research is to develop a solution to the optical detection difficulties within fluorescence spectroscopy measurements for multianalyte studies. The central problem is the high complexity and cost associated with the optical systems needed for detection. Traditional benchtop spectrometers typically have low sensitivity or slow acquisition times compared to the needs of many of the fluorescence measurement applications. Larger scale spectroscopy setups that can transcend these limitations become too complex and expensive, limiting their uses to the select few. However, the results that come from these high cost setups are often very high impact and may be the solution to many of today's biological studies. A definite need exists for a system that has the capability of weak signal, multianalyte detection without costs and size dramatically increasing.

The secondary motivation for this research is to reduce the limitations on the integrations of polymers within microsystems. Many fields of MEMS devices rely on stiff, rigid materials often limiting their applications. MEMS that do incorporate elastic materials are often built with their entire structures made out of the material and loose the advantages of silicon based systems that have developed over several decades. A system that can integrate both types of materials at the scale of microsystems can take advantage of both material properties. As an example of the capabilities that may be possible, we can look at macro scale devices. Developing a complex machine when limited to just rigid or compliant materials can be difficult or even impossible. It is the combination of these materials for specific pieces of the machine that create maximum effectiveness.

Microsystems can be viewed in the same manner. Being able to have certain joints or sections made from elastic material opens up the possibility of new designs that will expand how MEMS structures are built and function.

These two problems in fluorescence spectroscopy and microsystem technology are the motivations of this research. Optical setups are incapable of multiwavelength detection for multianalyte biological studies without a dramatic increase in the cost of detection equipment. To reduce the dependence on advanced detectors, tunable optical components are needed to manipulate the signal before detection. We propose solving these problems by implementing MEMS as the tunable optical components. To accomplish this goal requires the development of MEMS devices that transcend traditional MEMS capabilities by utilizing both rigid and soft materials.

1.3 Thesis Objectives

This research has four sequential goals that are driven by the motivations above and address the shortcomings of current technology. The first objective is to outline how a MEMS device can be implemented into a spectroscopy setup to create an optical system with advantages over the standard fluorescence detection technologies. The second objective is to further develop the field of MEMS devices that incorporate elastic materials with rigid structures. The progression of this hybrid MEMS technology is an integral step towards achieving the primary research goal. The third objective is to implement this new technology and create a MEMS tunable grating with capabilities that match or exceed the application requirements. The tunable grating must utilize the integration of polymers in microsystems in order to surpass other MEMS technologies and meet these requirements. The final objective is to develop an optical system capable of fluorescent spectroscopy for multiwavelength detection capabilities. This objective addresses the primary motivation of the research by implementing the MEMS tunable grating to dramatically improve the system requirements needed for fluorescence spectroscopy. These sequential objectives are the drivers of the research presented in this thesis.

1.4 Thesis Outline

The work accomplished in order to complete these thesis objectives is organized into five branches. Each division is a chapter within the thesis. The ensuing chapters are summarized as follows:

Chapter II – Review of Related Studies: This chapter reviews other research related to this project. Included in this review is work that provided essential information for the completion of this project as well as competing technologies with similar goals and applications. The review is broken down into three main categories: (1) spectroscopy research and applications, (2) tunable gratings, and (3) polymer microsystems. These three categories cover the influences of our MEMS design and its applications.

Chapter III – Design of Spectroscopy System: This chapter covers the design of our spectroscopy optical system using the MEMS tunable grating. The design concept is first covered, showing the initial vision of how a unique MEMS tunable grating can be implemented for high impact spectroscopy measurements. Next discussed are the criteria of a spectroscopy system and the design of our system to maximize its capabilities. With the specifications outlined, the design of the hybrid MEMS tunable grating is then described. Mechanical models and design parameters for the MEMS device are given.

Chapter IV – Fabrication and Characterization Measurements: This chapter discusses the process for MEMS fabrication and the experiments run for proof of concept measurements. The section on fabrication outlines in detail the steps taken to accomplish the PDMS-silicon integration of microstructures. Completed devices are shown. Optical experiments are then run to measure the design's capabilities. Comparisons to the analytical models are given along with an in-depth look into the material science factors that must be addressed when operating with the polymer PDMS. The MEMS device is then fitted into the spectroscopy setup for demonstrations of high speed, high sensitivity measurements. All of the criteria outlined in the previous chapter are measured and analyzed.

Chapter V – Applications of Technology for Fluorescence Measurements: This chapter discusses applying the MEMS spectroscopy setup for fluorescent measurement applications. The goal of this section is to complete the primary research objective and

create a system capable of the high speed and sensitivity needed for fluorescence detection applications but with reduced dependency on photodetector cost and complexity. The opening of the chapter covers the device's integration with a fluorescence microscope and the advantages gained with this arrangement. An analysis of the system's capabilities is covered and includes the entire optical system surrounding the MEMS device. A newer MEMS layout made specifically for the microscope integration is designed and fabricated. Spectral measurements are then taken with the use of a microfluidic cytometry device for high throughput measurements.

Chapter VI – Conclusions and Future Work: The final chapter summarizes the impact of the presented research and discusses future potential research. The future work is broken down into three branches: (1) spectral measurements for the designed MEMS-microscope integration system, (2) future plans for the MEMS tunable grating in different optical systems, and (3) other potential applications for the developed polymer-silicon microscale integration.

Chapter II

Review of Related Studies

In order to accomplish the thesis objectives, a review of related research studies is first completed. These studies give insight to the motivations and applications of our research as well as study competing technologies. Our work plans to make an impact on fluorescence spectroscopy detection technologies by using a polymer MEMS tunable grating to dramatically reduce detection equipment requirements. To accomplish this goal, we research several fields that relate to our plan. The review is divided into three sections: (1) spectroscopy research and applications, (2) tunable gratings, and (3) polymer microsystems. Each section details why the review of this material is relevant and provides multiple examples of current work achieved on the topic.

2.1 Spectroscopy Research and Applications

Spectroscopy deals with the measurement of an optical signal's intensity as a function of wavelength. The applications for spectroscopy cover a large variety of fields, but this report covers different fields of fluorescence spectroscopy that coincide with our research motivations. Applications often include multicolor fluorescence for multianalyte studies, found in fields such as spectral flow cytometry. Other presented research is geared towards designing unique spectroscopy systems, especially ones integrating MEMS or micromachining as our design is not the first to conceive this idea. Research is also directed towards improving the photodetection technologies for better detectors within spectrometers. The following sections review all of these spectroscopy topics relevant to our research.

2.2.1 Multianalyte Research

A recurring need in many biological studies is the ability to examine multiple analytes from a single sample. In fields such as clinical medicine, repeated sampling can become dangerous to the patient's health. Multianalyte studies reduce the amount of testing, increase throughput, and provide more information on variable dependencies [25]. Certain studies array analytes from a sample and design optical techniques for measuring different analytes spatially [4, 5]. More recent research, however, has pushed towards multicolor detection techniques to distinguish analytes. These type of measurements are difficult, and several complex optical systems have been designed for multispectral fluorescence detection [26]. An example of this type of research is the detection of biomolecules inside a cell using fluorescence. Schönle et al. [27] demonstrate using cyanine dyes within cells for fluorescence nanoscopy. Multicolor images with spatial resolution on the order of nanometers are generated by exploiting the special dyes with photoswitchable properties. Their detection technique involves using two CCD cameras with a dichroic mirror, and detection of the three different fluorophores is based on the ratio of intensities between the cameras. This technique is compared to the work of Bates et al. [28] who use the sequencing of multiple excitation sources to gain selectivity in the detection of multiple colors. Both techniques are illustrated in Figure 2.1 [27].

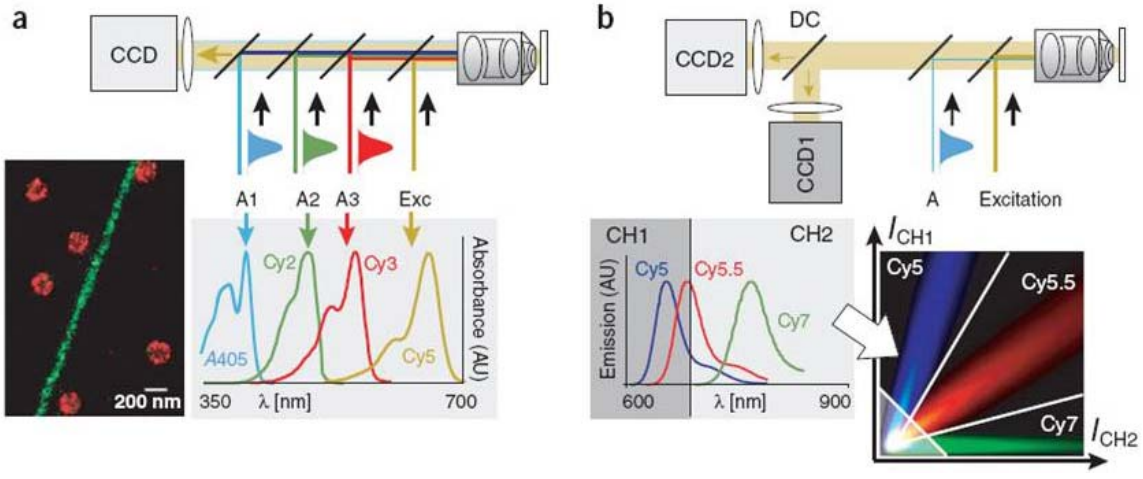

Figure 2.1: Illustrations of two types of detection techniques for multianalyte studies using high resolution multicolor imaging. (a) A sequence of different excitation light sources determines which known fluorophore is excited for detection with a CCD camera. (b) Two CCD cameras image a cell with three fluorophores of varying spectral emission, and the intensity ratio determines the detected fluorophore [27].

Another similar study was conducted by Bossi et al. [6]. Two electron multiplying charged coupled device (EM-CCD) cameras are used in a setup similar to the setup of Schönle et al. Different types of rhodamine amides were detected within mammalian cells. Figure 2.2 shows the emission spectra of the fluorescent isomers used in the study. The detection technique was used for nanometer resolution imaging that gives precise information on the location of fluorophore within the cell. Possible applications of this technology include studying antibodies labeled with multiple colors.

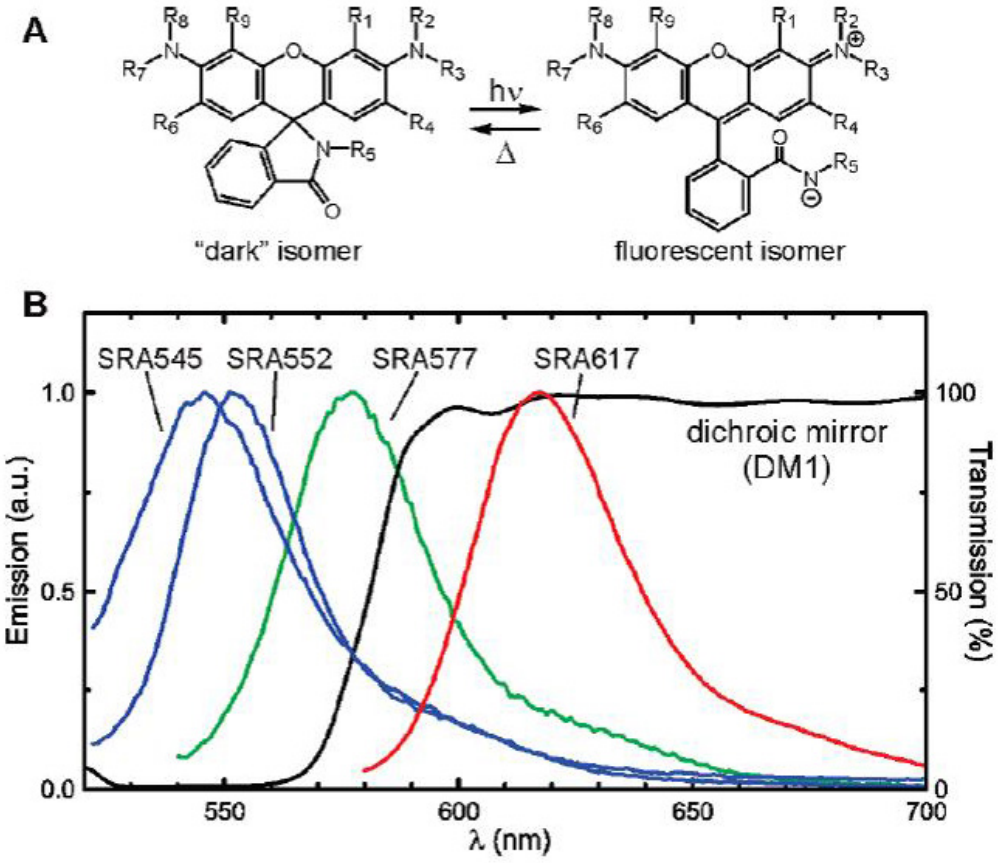

Figure 2.2: Rhodamine fluorophores used for multicolor measurements within cells. (a) Molecular representation of the polychromatic switching between dark and fluorescent states. (b) Emission spectra of different fluorophores and the transmission spectra of the dichroic mirror [6].

The work of all these studies shows that a large need exists for detection technologies that can measure fluorescence of varying spectral emission. The simultaneous measurement of multiple colors is an essential technique for abstracting as much information as possible from samples. Unfortunately, to accomplish these detection

capabilities requires multiple high powered photodetectors along with significant data processing.

2.2.2 Spectral Flow Cytometry

Another example of polychromatic detection is in spectral flow cytometry [7, 29, 30]. Flow cytometry is a scientific tool used for high throughput analysis of a large collection of cells or other similar sized particles. The particles are run through a fluidic channel in single file at high speeds, and optical measurements of each particle are taken. Multispectral flow cytometry is capable of measuring multiple emitted colors simultaneously. Flow cytometers have become essential tools in research fields such as immunology where multi-parameter, high throughput experiments are required.

While advances in flow cytometry include substantial studies on the fluidics [31] and the electronics [32], the main field of improvement research involves the optics. Polychromatic measurements of the high speed, low intensity fluorescence cannot be achieved with a standard spectrometer. Typical spectrometers use a CCD camera as its detector, which can have trouble with rapid, weak signals. The problem with detecting an entire spectral range spatially is that each wavelength is only read by a very small pixel of the camera. If the signal is constant, it can be integrated over time for detection, but quick readings of high speed fluorescent elements are not feasible. The alternative is single point detectors such as a photomultiplier-tube (PMT) or a single-photon avalanche photodiode (SPAD) which can greatly amplify the weakest of signals [33]. Because of the signal amplification physics of these detectors, it is very difficult to array them closely enough to measure separate wavelengths of the spectrum. These detectors lack spatial resolution, and alternative methods such as filters and slits are used to determine the wavelength. Multianalyte studies require that multiple colors be detected, and a PMT alone is incapable of wavelength discrimination. The setup used instead is an octagon of PMTs with specific filters and reflectors in front of each, so that only a band of the electromagnetic spectrum is analyzed. Careful calibration steps are also taken for any of the spectral overlap incident on each PMT. Figure 2.3 shows an example of this octagon configuration. This setup is large, expensive, and requires expertise for tuning.

However, the results from this research are helping make great progress in fields such as immunology. For example, Chattopadhyay et al. [7] used multicolor flow cytometry to determine patterns in phenotypes for antigen-specific T-cell populations. The success is due to the simultaneous multianalyte processing that helps determine the cause and effect of stimulants.

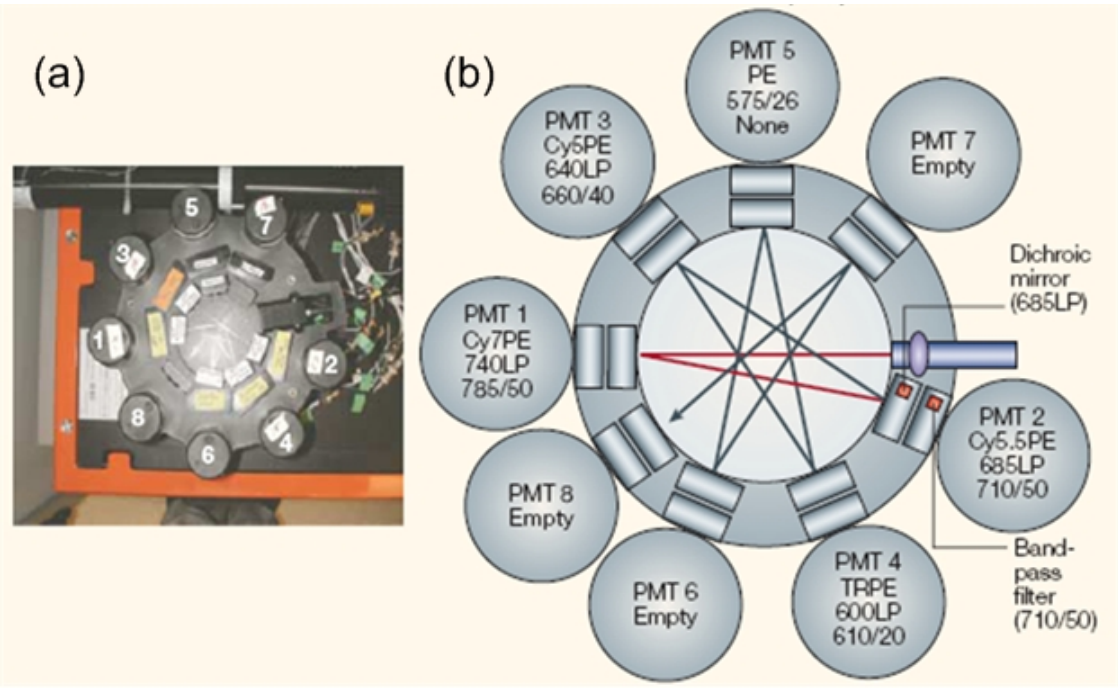

Figure 2.3: Laser geometry and fluorescence-emission detection system of a multi-parameter flow cytometer. (a) A photograph of the octagon assembly. (b) Graphical representation of this assembly showing a series of PMTs, filters, and reflectors [29].

2.2.3 Single Molecule Spectroscopy

Other research where single point detectors are utilized is single molecule spectroscopy [33, 34]. This relatively new field of research has become a powerful technique for observing the behavior of nanoscale molecules in a variety of environments. By studying exactly one molecule at a time, the ensemble averaging of emitted signals is removed and more detailed conclusions of the molecule's interactions can be made. The process of detecting the emission of a single molecule inherently requires a highly sensitive single point detector or a costly, high powered spatial detector such as an EM-CCD camera. Another option is the use of a relatively new type of

detector called a multianode PMT. This detector is able to array multiple PMTs directly next to each other so that spatial measurements can be taken with the sensitivity of a PMT [35]. A multianode PMT does not bin the detected signals for processing like a CCD, and separate readout connections are needed for each of the anodes. For a multianode PMT with 32 anodes, the readout connections and equipment can become costly.

2.2.4 Unique Spectroscopy Systems

Many other types of spectroscopy systems have been developed for the purpose of fluorescence detection. Our work is also not the first system to employ MEMS devices or silicon micromachining technology. Previous studies demonstrated key components for a MEMS-based spectrometer, which can be integrated with a microfluidic platform. For example, Goldman et al. [36] demonstrated a miniaturized planar waveguide spectrometer for chemical analysis. Their device consisted of a waveguide deposited on a glass substrate with an etched grating, where collected light travels through the waveguide while interacting with chemical samples. The resulting spectra are dispersed depending on their wavelengths at the grating and analyzed using an array of photodiodes. Mohr et al. [37] developed another type of planar waveguide spectrometer. This device introduced detected light into a polymer waveguide through an optical fiber and dispersed it at a reflection grating, which has been fabricated using reactive ion etching. A similar approach was implemented for the device by Sander and Muller [38], where a SiON layer was utilized as the waveguide. Yee et al. [39] combined silicon micromachined gratings with a CCD camera and used them in a hybrid system for operation as a spectrometer. More recently, Schmidt et al. [40] have demonstrated a chip size spectrometer integrated with a microfluidic platform by employing a linear variable band-pass filter and a CMOS camera.

One of the difficulties in integrating microfabrication technology is the incorporation of a focusing element. If miniaturized components are used, the focusing lens or concave refractive mirror must be precise. These elements are also difficult to fabricate on the microscale if a full microfabricated system is attempted. Not having a focusing element

affects the resolution, or wavelength discrimination, of the spectral measurements. To counter this problem, some studies have designed alternatives. Traut et al. [41] developed an array of microlenses with a grating pattern on the top surface. The result was a dispersive and focusing element built into one layer suitable for a miniaturized spectrometer array. Grabarnik et al. [3] designed a miniaturized full system spectrometer that utilized a second grating as its focusing element. The entire system is one of the smallest to date and can be seen in Figure 2.4.

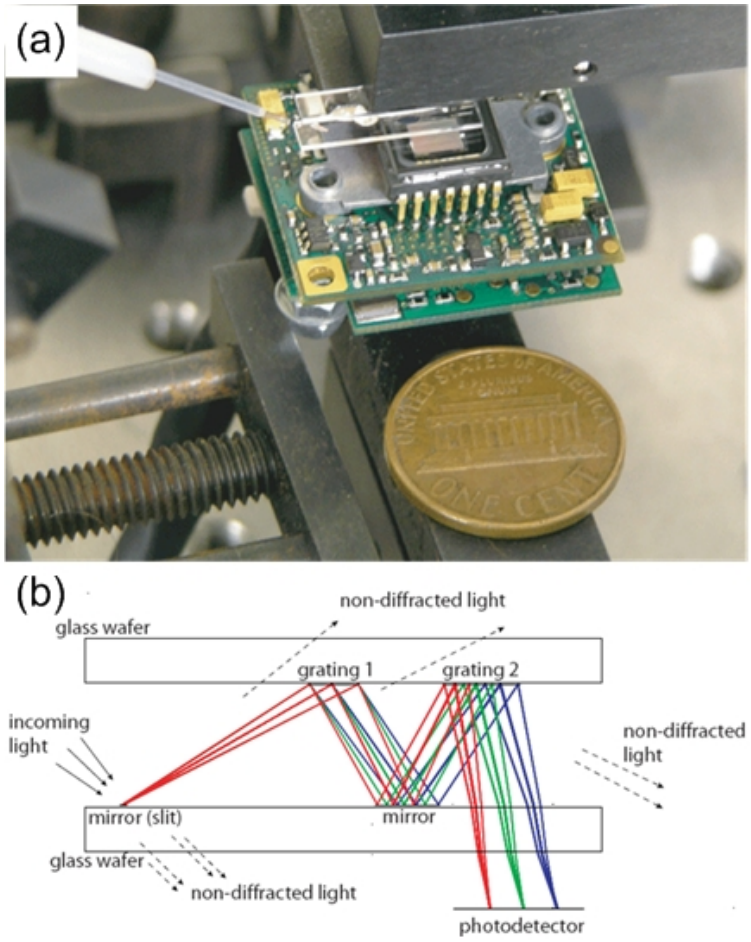

Figure 2.4: A micro-spectrometer. (a) Image of the experimental setup including two transparent glass slides mounted over the image sensor. (b) Illustration of the ray tracing of a double grating setup for diffraction and focusing [3].

Wolfenbuttal [42, 43] discussed more MEMS-based spectrometer setups that typically utilize smaller gratings and ignore the focusing element at the cost of wavelength resolution. Most detectors are composed of custom built photodiode arrays to spatially detect the diffracted signal. Minas et al. [44, 45] designed on-chip Fabry-

Perot optical channels in which only a specific wavelength band would not be filtered for each different sized channel. The filtered signals were then read by photodetectors underneath the channels.

Other unique systems have specialized setups for the detection of fluorescence in a microfluidic channel. Damean et al. [46] set up microlenses and a grating above a microfluidic channel. The optical signal after diffraction was collected with a benchtop microscope and read with a CCD camera. With this system they demonstrated resolving in space and time the fluorescence within a microfluidic system. Figure 2.5 shows their measurements of a microfluidic channel as the fluid changes from sulforhodamine B to fluorescein. A shift in the spectral peaks is apparent over time. Yee et al. [47] also demonstrated a similar setup for biochemical analyses.

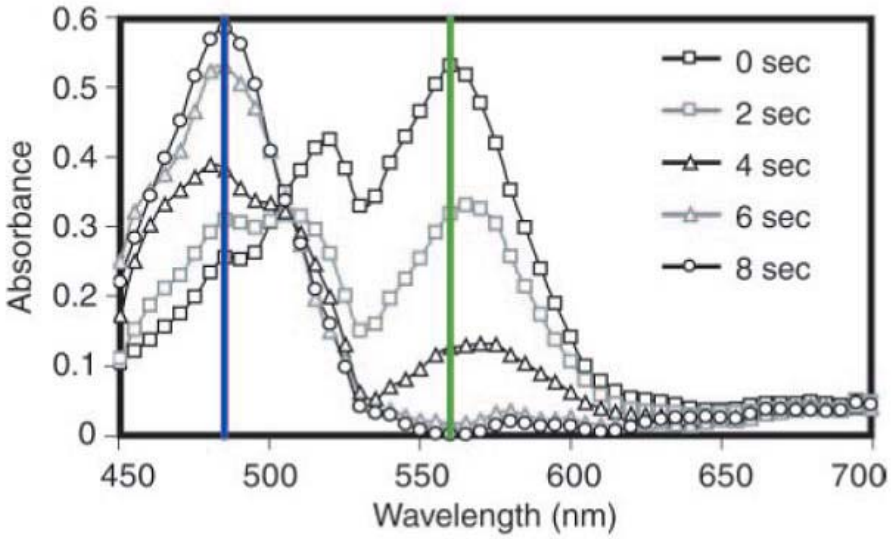

Figure 2.5: Fluorescent spectral measurements of a microfluidic channel as the fluorescent fluid changes over time. Solid lines mark the spectral peaks of each fluid [46].

These unique spectroscopy developments as well as studies in other fields such as spectral flow cytometry and single molecule spectroscopy demonstrate a wide variety in different techniques and applications for spectral measurements. The most important conclusion to come from this spectroscopy review is that a definite need exists for different types of polychromatic measurements, because multicolor detection yields more information and more possibilities.

2.2 Tunable Gratings

A tunable grating can be implemented as the critical component to dramatically decrease the number of high sensitivity detectors needed for weak spectral emissions. The technology developed in this research utilizes a MEMS tunable grating with a single high sensitivity detector to significantly save the running cost, volume, and power consumption of fluorescence spectroscopy. A tunable grating has the capability to change the diffraction angle of light and alter the wavelength that is measured by the detector. While gratings can be rotated to alter the diffraction angle [48], standard gratings are typically around a square inch in size, and their inertia prevents them from being repeatedly tilted at appreciable speeds. One example is in time-resolved laser induced fluorescence spectroscopy (tr-LIFS) [49, 50] where fluorescence decay is measured, and an entire spectrum is measured by scanning the grating of a monochromator. The time for each trace at a specific wavelength is approximately 200 ms, and the limiting factor is the time required for grating rotation.

A MEMS grating avoids this limitation and can tune a grating at frequencies over 1 kHz. The last decade has seen many different MEMS tunable grating designs, all varying in their speed, tuning range, and groove density. Liu et al. [51] created a rotational grating using a rotary comb-drive to develop a tunable laser. The grating structure was formed from the side walls of a deep reactive ion etch (DRIE) into silicon. The grating could rotate 1.6° and create a 0.1 nm shift in laser wavelength. Figure 2.6(a) and 2.6(b) shows scanning electron microscope (SEM) images of the MEMS design. Another style of creating a tunable grating is to alter the period of the grating. Several designs have used thin silicon beams each connected by a silicon spring and stretched by electrostatic actuators. The actuator displacement is distributed among the silicon beam array as each beam separates slightly more from adjacent beams. An illustration of this design is seen in Figure 2.6(c) [52]. Shih et al. [53] fabricated a grating with a 12 μm beams, and a comb-drive actuator changed the period by 57 nm. Tormen et al. [54] was able to generate a more significant shift, and could alter the grating period of 6 μm by 2.5% with a theoretical resonant frequency of 28.5 kHz, seen in Figure 2.6(d). Yang et al. [52]

created a similar design with electrostatic actuators and also included a tunable blaze angle of the grating structure, seen in Figure 2.6(e).

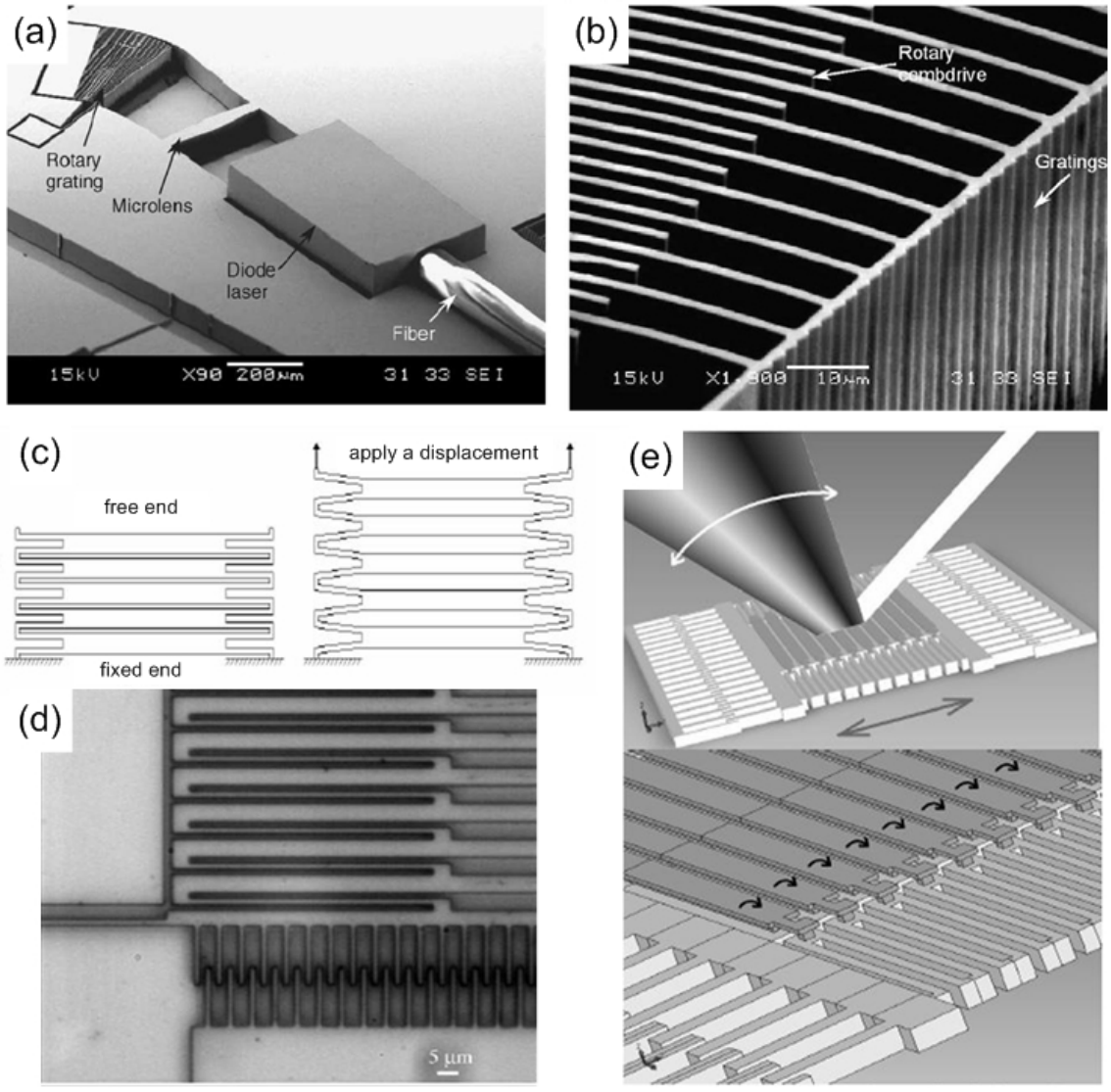

Figure 2.6: MEMS tunable gratings with electrostatic actuation. (a) Rotational tunable grating designed for a tunable laser. (b) Closer view of the grating and rotary comb-drive [51]. (c) Concept drawing of creating a tunable grating through thin beams connected by hinge springs in which the grating period changes with actuator displacement. (d) Close up image of the springs and comb-drive of a tunable grating [54]. (e) Concept images of a tunable grating in which the blaze angle is also adjustable [52].

Other designs have been fabricated with different MEMS actuators as well. Zhang et al. [55] created a novel thermal actuator to vary the spacing of the grating. Each silicon beam within the grating was connected to a diamond shaped structure made from other silicon beams, as seen in Figure 2.7(a) and 2.7(b). With a current applied through the diamond shape, the beams would thermally expand and alter the spacing between grating

beams. Electron beam lithography was used during fabrication to decrease the grating period to less than 1 μm. A grating period shift from 700 nm to 1140 nm was demonstrated. One problem with thermal actuators, however, is slow response time, especially during cooling to return to its initial state. The small silicon beams are also susceptible to burning up if too much actuation current is applied. Other actuators include piezoelectric, which generally have fast switching times but low tunable ranges. Wong et al. [56] used piezoelectric actuators to strain a microbridge that included a grating structure, seen in Figure 2.7(c). The strain induced was 0.2% with an actuation time of 19.6 μs. Lo et al. [57] used piezoelectric actuators to tilt an optical grating with a seesaw-like movement. The actuators were capable of a 3.05° tilt at a 4.3 kHz resonant frequency. The design built for a microspectrometer could cover a 100 nm range with the maximum tilting angles. The device seemed to have complications with fabrication and optical flatness.

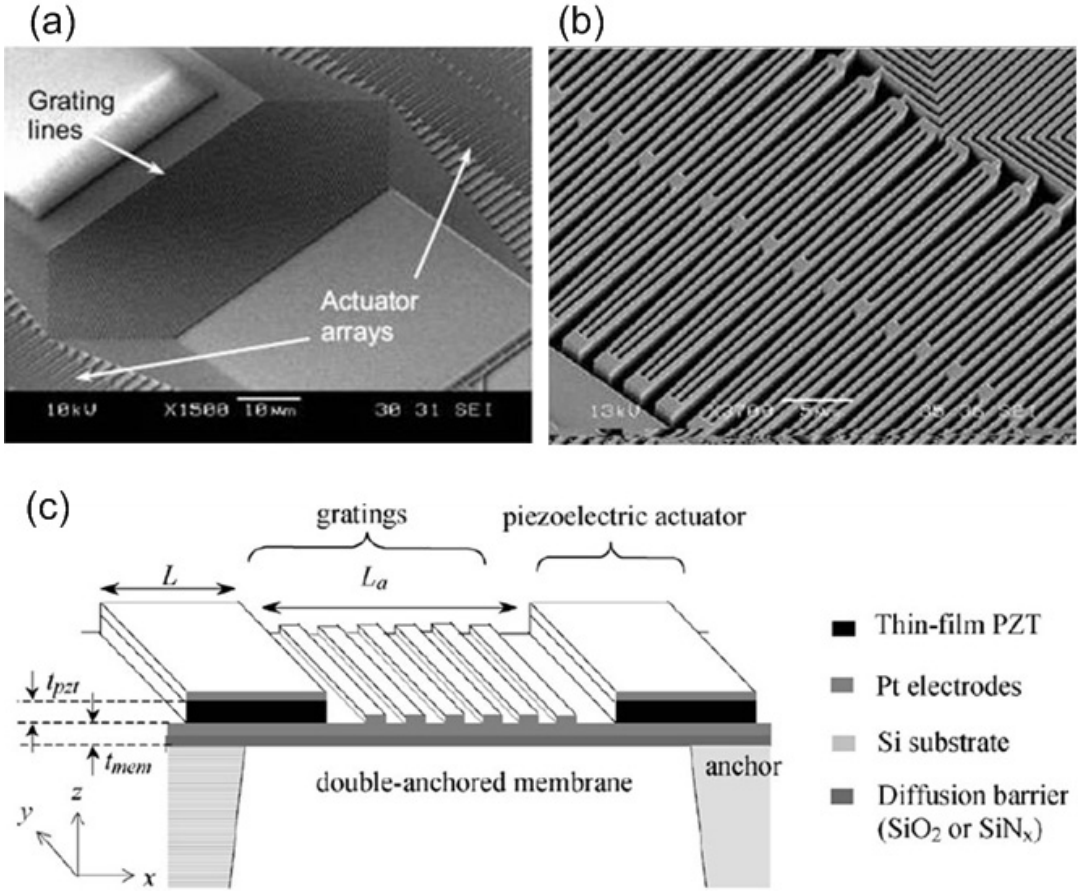

Figure 2.7: MEMS tunable gratings with thermal and piezoelectric actuation. (a) Submicron grating structure tuned by thermal actuators. (b) Close up of the actuator units [55]. (c) Schematic for a tunable grating driven by piezoelectric actuators [56].

Polymers have also been utilized to create tunable gratings, both at micro and macro sizes. Hosokawa et al. [58] created an array of microfluidic channels from PDMS that acted as an optical grating. As the pressure in the channels varied, the bulging of the channels would change the grating efficiency. The period of the grating remained the same however, and the application of this device was to measure the pressure and not to create a tunable grating for other purposes. Aschwanden et al. [59] used a dielectric elastomer actuator that increased in volume with an applied electrical voltage. A tuning range of 32% of the grating period was demonstrated with the application of 4.5 kV. The tuning speed is theorized to be over 1 kHz but is not demonstrated and power supply limitations are not taken into consideration. Simonov et al. [60] created a tunable polymer grating on the macro scale. A slab of PDMS polymer is imprinted with a 4.46 μm grating and strained up to 20% using a voice coil actuator. A frequency of 1 kHz is demonstrated, but the device must operate well over the resonant frequency at ~200 Hz, and it is not told how much strain is possible at this higher speed.

Many different studies have looked at creating a tunable grating. Particular interest has been given to MEMS actuators to tune an optical grating due to their inherent fast actuation speeds. Still, very few designs have been able to achieve speeds over 1 kHz with tunable ranges over 10%. Those that are capable often have undesirable characteristics such as difficult fabrication, frailty, and low optical flatness.

2.3 Polymer Microsystems

Of all the tunable grating designs, the ones with the most potential may be those designed with polymers. Many polymers have high strain capabilities, and stretching a polymer grating can create a large range of tunability. Combining these material characteristics with the advantages of MEMS can lead to an ideal tunable grating for spectroscopy applications. A review of different MEMS devices which incorporate polymers is conducted to better understand these possibilities.

For microsystem applications, polymers have found uses in fields such as microfluidics, packaging, optics, dielectric layers, lithography, as well as others. One of

the most prominent examples is in microfluidics and is the creation of microfluidic pumps and valves using overlapping channels made from poly(dimethylsiloxane) (PDMS) [61]. Controlling the pressure in one of the channels forces a thin PDMS membrane between the overlapping channels to stretch and close off the underlying channel. When controlled in succession with adjacent channels, this style of valve closing can be used to displace the fluid and pump the flow of the underlying channels. This technique for pumping microfluidics has become widespread and is possible due to the pliability of the PDMS material. Another example in microfluidics is the development of tunable nanochannels that can dynamically change size for the sorting and trapping of nanoparticles and DNA strands [62]. The channel width is controlled by the pressure within the nanochannel, as a higher pressure can expand the soft material. Another utilization of polymer properties in microfluidics is the use of PDMS's optical transparency and good transmission of visible light, which permits on-chip optofluidic fluorescence detection in microfluidic systems [63, 64].

Other microsystem applications include the formation of conjugated polymer actuators. Jager et al. [20] created actuators capable of large out-of-plane movements due to the polymer's compliancy. A polypyrrole-gold bilayer was formed into fingers that could curl and grab objects as well as containers that could fold over and trap their liquid contents. Figure 2.8 displays an illustration and optical image of these actuators. Along with actuators, the feasibility of sensors such as accelerometers composed of PDMS has been researched [65].

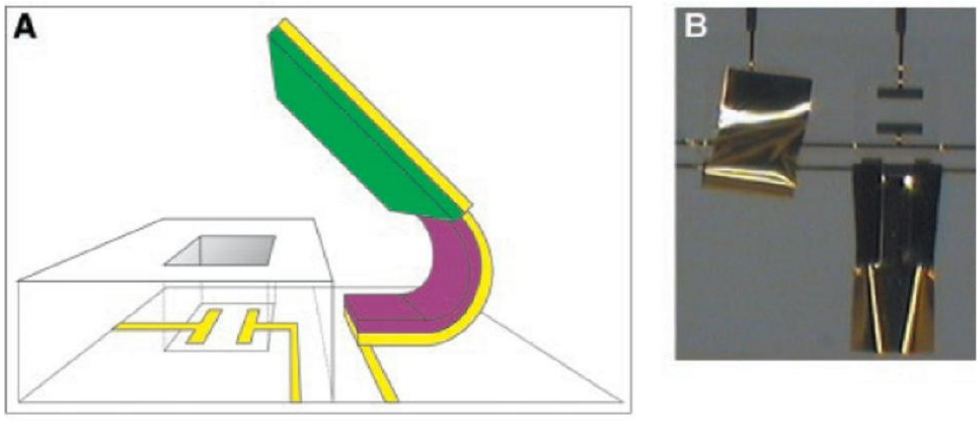

Figure 2.8: Example of micro-actuators implementing polymer layers. (a) A schematic picture of a cell clinic consisting of a microcavity (100 μm by 100 μm) that can be closed with a lid (green and yellow) activated by polypyrrole hinges (purple and yellow). (b) Picture of two cell clinics, one closed and one open [20].

Researchers have also found uses for polymers in optical and photonic microsystems. Replicate pattern capabilities and elasticity have enabled unique designs such as a compound lens resembling an insect eye [66]. Nanoimprinting [67] and soft lithography [68] of polymers have created optical grating structures on the submicron scale. Photonic crystals can benefit from elasticity in their structures. The formation of a photonic bandgap is heavily dependant on the periodicity of the structure, and a post fabrication reversible tunability through mechanical strain is highly desirable [69, 70]. Figure 2.9 shows the concept of a tunable photonic crystal made possible through elastic polymers. Polymeric optical ring resonators have also gained recent interest, and submicron waveguide gaps along with thermooptic tuning capabilities have been demonstrated [71]. One concern with tuning polymer optical components is the alteration in material's optical properties such as the refractive index. Hoshino et al. [72] studied the use of PDMS as a tunable microlens and measured the effects of the change in refractive index. Their work concluded that the shape deformation was dominant over possible birefringence in determining the optical path of a signal.

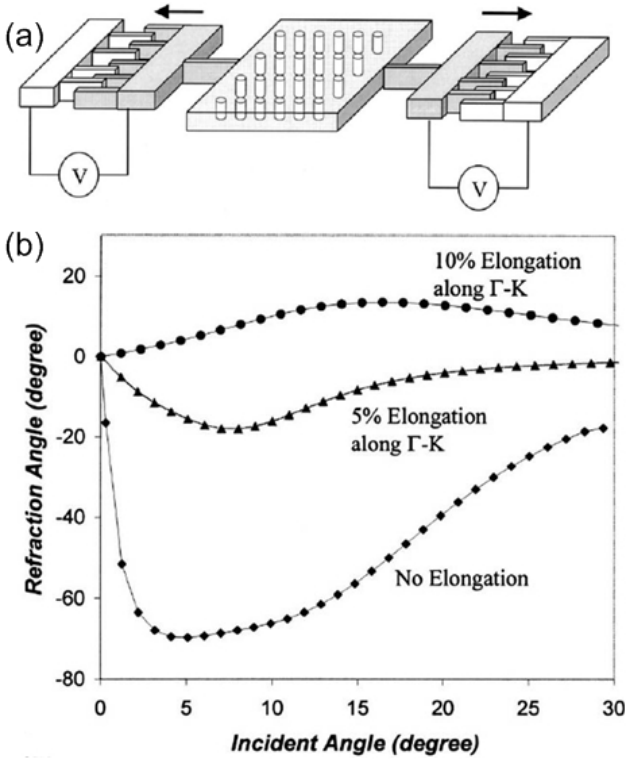

Figure 2.9: A tunable photonic crystal fabricated from polymer. (a) Schematic of flexible photonic crystal composed of Si pillars in a flexible polymer film and controlled by MEMS actuators. (b) Refraction angles calculated by dispersion curves showing the effects due to high strain capabilities [70].

Previous research from our group developed a PDMS bridge spanning across two silicon comb-drives [73-75], as seen in Figure 2.10. The microbridge had a submicron grating pattern on the top surface fabricated from soft lithography. The elastic material allowed for straining of the bridge with forces from the comb-drive actuators. The grating period on the top surface would vary with the strain. This type of tunable grating allowed for a high groove density without the frailty of hundreds of silicon beams placed in sequence. The elasticity of PDMS allowed for strain without the high forces needed for straining rigid materials. The design reached strain values of 1.5% and had a calculated resonant frequency near 3 kHz. The limitation of the speed and strain range was dependent on the MEMS actuators and not the passive PDMS bridge.

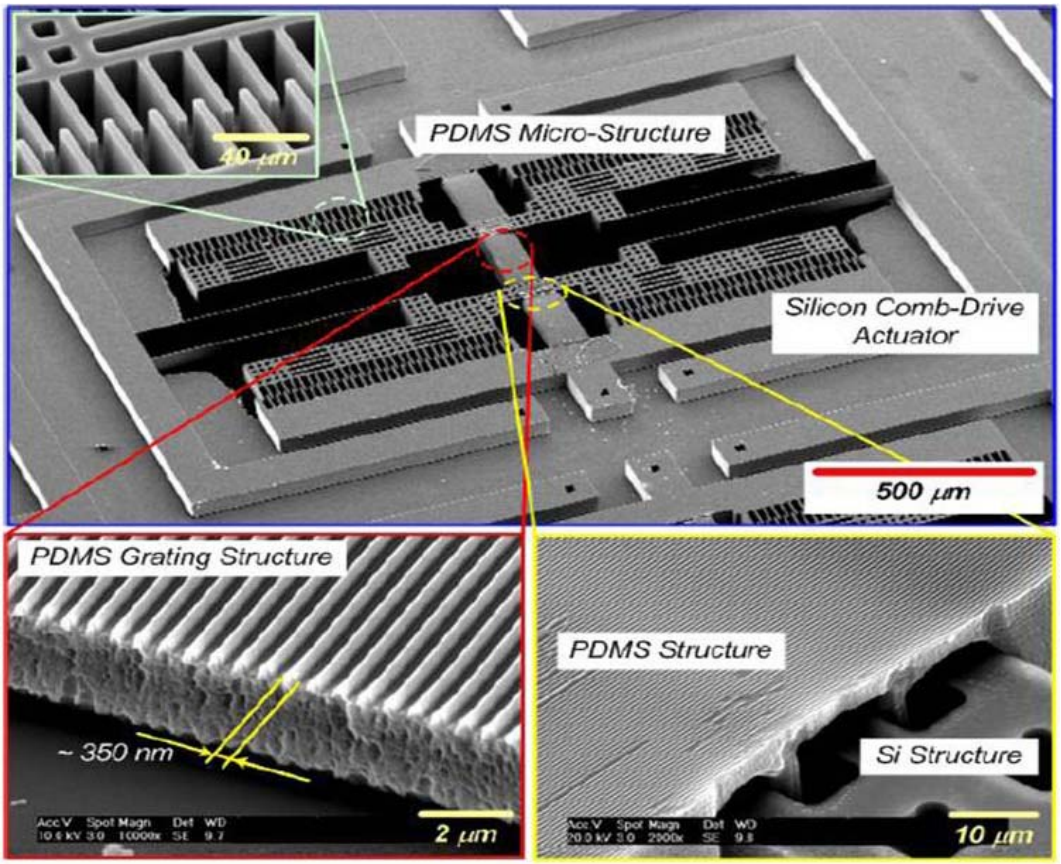

Figure 2.10: SEM images of the reconfigurable micro-optical grating [75].

It is clear from these studies and others that polymers have their place within MEMS and other microsystems due to their unique material properties. A polymer tunable grating using MEMS technology is the best option for our required tunable optical component. These polymer studies along with the other reviewed research exemplify the

need for simple multiwavelength detection systems and the technology needed to accomplish this task.

Chapter III

Design of Spectroscopy System

3.1 Concept

Due to the motivations and limitations of current technology described above, the need for a new spectroscopy system exists. A design with high sensitivity, high speeds, and a simple compact optical setup can have immediate applications in multiple fields. To meet this demand, a spectroscopy system with a MEMS tunable grating is designed. The device design is a PDMS microbridge connected on one side to a silicon MEMS actuator with the other side connected to fixed silicon. The microbridge contains a nanoimprinted grating pattern on the top surface, creating an effective optical transmission grating. The MEMS actuator is an electrostatic comb-drive design. Applying a voltage difference across the comb-drive generates a force that mechanically stretches the microbridge, altering the grating spacing on the top surface. The grating can elastically stretch and tune the grating period at the high speeds of the MEMS actuator. By utilizing the hybrid properties of the device, our tunable grating has a large range, fast actuation speed, and groove density that other MEMS tunable gratings may lack. With the application of an innovative tunable grating, spectral measurements can be taken in a sub-millisecond time window with the sensitivity of a single point detector such as a PMT.

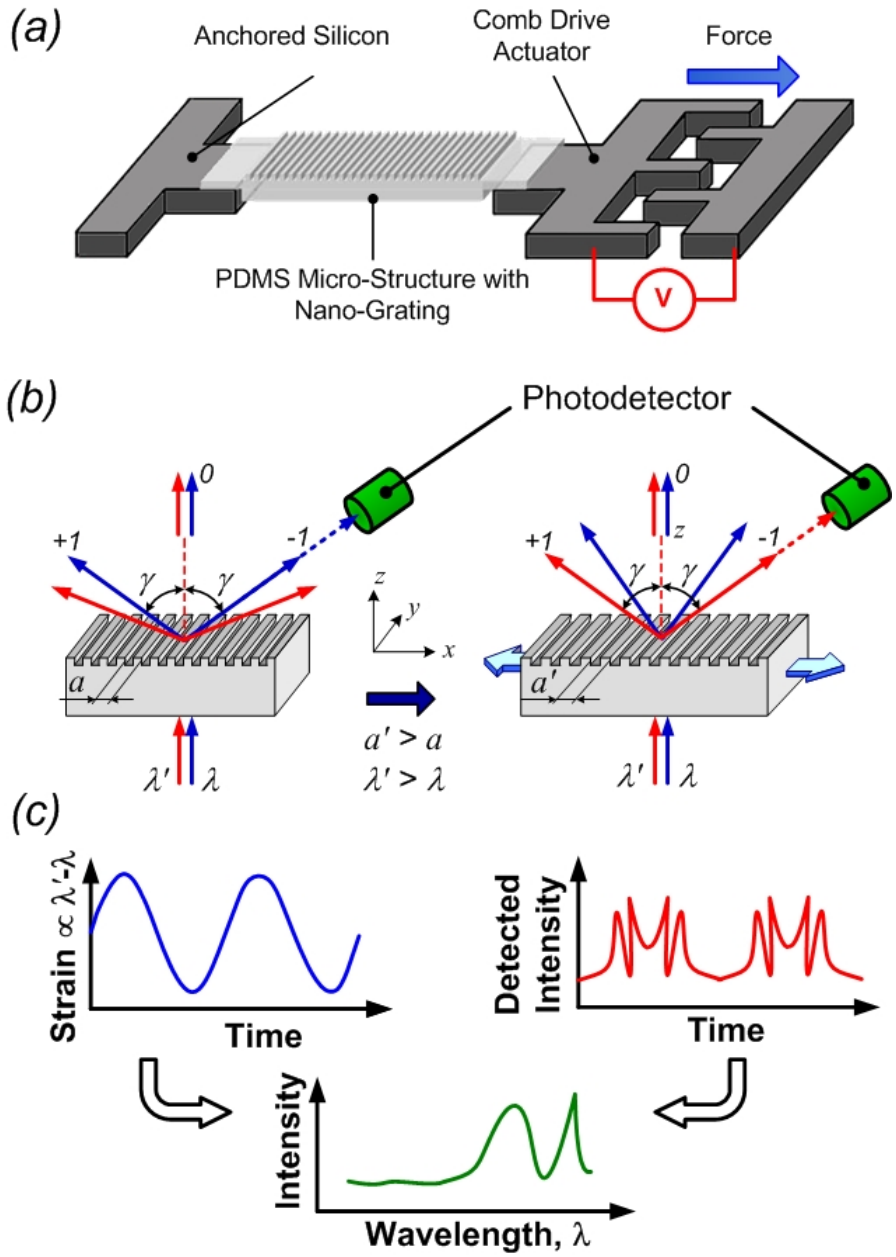

Figure 3.1: Schematic of strain-tunable nano photonic device with elastomeric nanostructures integrated. (a) Device concept. (b) Grating operational principle. (c) Spectrum data acquisition.

Figure 3.1 illustrates the principle of the device operation. Figure 3.1(a) is the MEMS device including the flexible polymer bridge with nanograting. A wavelength scan for incident fluorescence signals is performed by repeatedly varying the PDMS grating pitch with the silicon comb-drives driven by an AC actuation voltage signal. The intensity of a particular optical spectrum is detected at a non space-resolving single detector. Figure 3.1(b) shows the principle of the device operation for the incident light

normal to the grating plane. A transmission optical grating with a spatial period a lies in the xy-plane, and a light source with a broad wavelength spectrum is incident to the z-direction. The grating equation of a transmission grating is the following:

$$m\lambda = a(\sin\gamma + \sin\beta), \tag{3.1}$$

where m is the diffraction order, λ is the incident light wavelength, a is the grating period, γ is the diffraction angle, and β is the incident angle [76]. At the first diffraction order ($m = 1$), with the incident angle at the normal of the grating ($\beta = 0$), Equation 3.1 is simplified to

$$\lambda = a\sin\gamma. \tag{3.2}$$

When introducing a mechanical strain to elongate the spatial period of the grating to a', the wavelength of the first order diffraction at the same angle γ shifts to λ'. The corresponding mechanical strain ε can be defined as

$$\varepsilon = \frac{a' - a}{a} = \frac{a'}{a} - 1. \tag{3.3}$$

Then, the relation between the wavelength shift $\lambda' - \lambda$ and the mechanical strain can be given by

$$\lambda' - \lambda = a\varepsilon\sin\gamma = \lambda\varepsilon. \tag{3.4}$$

From this relation, the wavelength shift of the first order diffraction at the angle γ is linearly proportional to the mechanical strain introduced to the grating structure. Consequently, the peak wavelength of the diffracted light detected at a specific angle can be tuned by controlling the mechanical strain while maintaining the linear strain-diffraction angle relation. It follows that we can obtain plots of emission spectra by mapping the detected intensity and actuation voltage (as seen in Figure 3.1(c)) following

$$\lambda' - \lambda \propto \varepsilon \propto F = C_M V^2, \tag{3.5}$$

where F is the actuator force, V is the actuation voltage, and C_M is a value determined by the design parameters of the MEMS device. This method requires no complicated spectrum-plot construction and signal processing algorithms that can take time in other spectroscopy setups. With a fast enough detector, the speed of the acquisition of a range of wavelengths is only dependent on the speed of the MEMS actuator. The detector is

also not limited to weaker detectors that spatially map the diffracted signal. Only a single point detector is needed, which can be highly sensitive. Figure 3.2 illustrates the concept of this MEMS device incorporated with a PMT setup. A detector such as a PMT which is only a couple inches in length could be incorporated with the MEMS device and readout circuitry for a spectroscopic system similar in complexity to other commercial spectrometers but with significantly higher sensitivity levels.

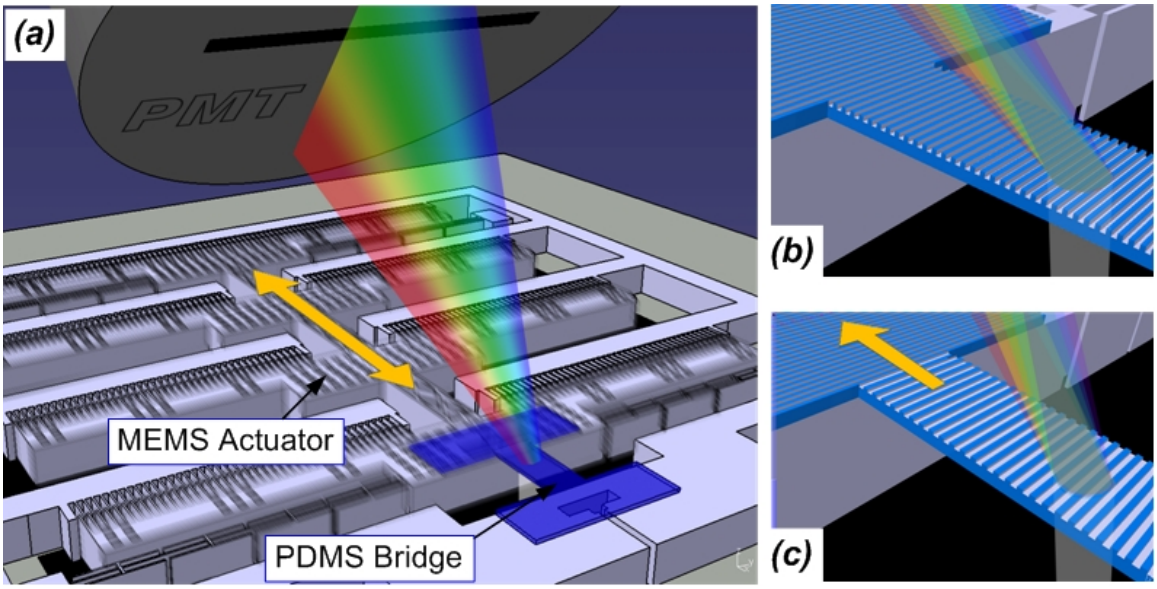

Figure 3.2: Illustrations of the device operation for spectroscopic measurements. (a) The MEMS comb-drive actuators stretch the elastomeric grating causing the optical diffraction angle to dynamically vary. The slit in front of the detector only allows the intensity of a narrow spectral band of the dispersed light to be detected. (b) Image of the microbridge with grating imprint at initial state. (c) Image of the microbridge stretched to alter the grating spacing.

3.2 Spectroscopy Criteria

All spectroscopy measurements have certain parameters that determine the quality of the system and usability for certain applications. Our spectroscopic design must take into consideration all of these criteria in order to fit the targeted need in technology. The criteria we take into consideration are spectral resolution, wavelength range, dynamic response, detector sensitivity, and grating efficiency.

3.2.1 Spectral Resolution

One of the performance indicators is the spectral resolution as it determines the device's capability of wavelength discrimination. It is defined in terms of "chromatic resolving power" given by $R = \lambda / \Delta\lambda$, where λ is the wavelength of interest, and $\Delta\lambda$ is the limit of resolution, or the difference in wavelength between two lines of equal intensity that can be distinguished. The limit of resolution is determined by diffraction theory based on the Rayleigh criterion, which claims that two wavelengths are just resolved when the maximum of one lies at the first minimum of the other. When the dispersed optical spectra are detected at a position far enough to exceed the Rayleigh distance [77], it is shown that

$$R = \frac{\lambda}{\Delta\lambda} = mN_g \tag{3.6}$$

where m is the order of the diffraction, and N_g is the total number of grating grooves [78]. To ensure that we can still use the far-field diffraction theory for our grating design, we calculate the Rayleigh distance given by

$$D = N_g{}^2 a^2 \big/ \lambda, \tag{3.7}$$

which is approximately 6.3 cm for a grating with $a = 700$ nm and a length of 200 μm. If we use the first-order mode $m = 1$ that yields the highest intensity for the dispersion operation, our MEMS grating device should yield $R = N_g = 287$. For the typical visible wavelengths between 450 nm and 650 nm, the theoretical upper bound for $\Delta\lambda$ is smaller than 2 nm. This preliminary design indicates that the nanometer-scale grating feature is critical for our device to achieve high spectral resolution at this level. The expected value of R for our device is an order of magnitude larger than that of other MEMS-based spectrometers [46, 77].

3.2.2 Wavelength Range

The range of wavelengths for the spectroscopy measurements employing our device is determined by the maximum strain level caused to the PDMS grating structure. Most

commercial CCD based spectrometers designed for the visible spectrum have a range greater than 300 nm, but often for spectral measurements, the critical information lies within a 75 nm band. To achieve this scan range, we designed the comb-drive actuators and the PDMS structure such that the maximum strain can be more than 10% with an actuation voltage near 150 V. This strain value translates into the need for displacement of at least 20 μm generated by the comb-drive end of the PDMS grating structure. The displacement and force generated are directly related to the number of comb finger electrodes, the stiffness of the silicon suspension beams, and the elasticity of PDMS. Two approaches can be taken to meet the strain requirement. First, we limit the thickness of the PDMS grating structure to less than 10 μm. Due to the softness of PDMS with such a small Young's modulus (~750 kPa), achieving the aimed strain level with actuation force smaller than 100 μN is possible. Second, we carefully designed the suspension springs of the comb-drives to generate sufficiently large displacement with good stability.

3.2.3 Dynamic Speed

For spectral measurements using a CCD camera, the speed of acquisition is typically inversely proportional to the sensitivity. Acquisitions in shorter time frames means less integration time of the signal. Most benchtop spectrometers have programmable integration times ranging from several milliseconds to seconds. For the applications discussed, the required measurement speeds vary. Several applications, such as flow cytometry require readings every millisecond without a loss of sensitivity. If the designed setup can take measurements at 1 kHz, many of the application speed requirements will be met.

For our setup, the speed of the spectrum acquisition is primarily governed by the dynamic bandwidth of our device as the bandwidth of the single point optical detector is typically much larger. An analytical mass-spring system model can guide our design of the MEMS device. The primary mass is the silicon comb-drive structure, which can be estimated with the volume and silicon density. The device system has two spring components: (1) the silicon suspension beams that guide the lateral motion of the rotor and (2) the PDMS grating bridge structure itself. Their spring constants can be calculated

using solid mechanics theory. If the MEMS device is designed so that the resonance frequency is higher than 1 kHz, the spectrum acquisition can be completed within a millisecond or shorter.

3.2.4 Optical Signal Sensitivity

Sensitivity is one of the main advantages of our design compared to standard spectrometer setups, due to needing only a single point photodetector instead of a pixilated detector. Sufficiently high sensitivity is also required for the photodetector to allow for the fast spectrum acquisition mechanism based on "single-shot" optical detection during a single period of the MEMS actuators. For this study we use a PMT which is capable of very high sensitivity and speeds but has no spatial recognition like the pixilated array of a CCD camera. Optical sensitivity is determined in terms of the minimum detectable power emitted from the sample.

Suppose for our spectral measurements, 100 different wavelength values need to be evaluated in 1 ms. These values translate to each wavelength value having a 10 μs window in which light is collected from a PMT. The number of counts of photo-induced electrons in the PMT is a function of the light intensity. Based on standard PMT specifications (P30CWAD5-01, Electron Tubes Inc.), we estimate that approximately 10 counts should be accumulated for every 10 μs interval to obtain a signal-to-noise ratio of 10. With the known optical power needed at the PMT entrance, the power is back calculated to the sample. Assuming an ideal slit and a grating efficiency of 70%, the optical power needed before the grating is approximately 4 pW. The light entering the grating comes from lenses that collect light from the sample. For a sample that emits light in free space equally in all directions, 20% is typically the amount of collected light from an ideal lens. The sample must then be emitting 20 pW of power to adhere to our design specifications for a single period of the MEMS actuators. In previous flow cytometry studies from our group [64], weak signals from fungus (*S. cerevisiae*) cells labeled by commercial fluorescent markers, such as Syto 62 and Syto 44 (Molecular Probes), were successfully detected using the same level of sensitivity. Therefore, the

expected sensitivity of our system should be large enough for the single-shot rapid spectrum acquisition.

3.2.5 Grating Efficiency

One of the aspects of improving the minimum detectable signal is the grating efficiency. Efficiency is defined as the ratio of the power of monochromatic light diffracted into the order being measured relative to the power of incident light. In general, grating efficiency varies with wavelength as well as with the spectral order and is highly affected by the grating profile. The profile of our grating is determined by the grating master mold that we copy using soft lithography (discussed further in Section 4.1). The master mold grating available for our process is a square shape profile with 700 nm period. GSolver software is used to determine the efficiency of the grating. Figure 3.3(a) shows the results of the simulation showing a first order efficiency of 13-23% for our wavelength range of interest. As the device is actuating, the grating period is also changing, and another simulation is run to determine how this change affects efficiency. Figure 3.3(b) shows minimal change as the grating period is shifting.

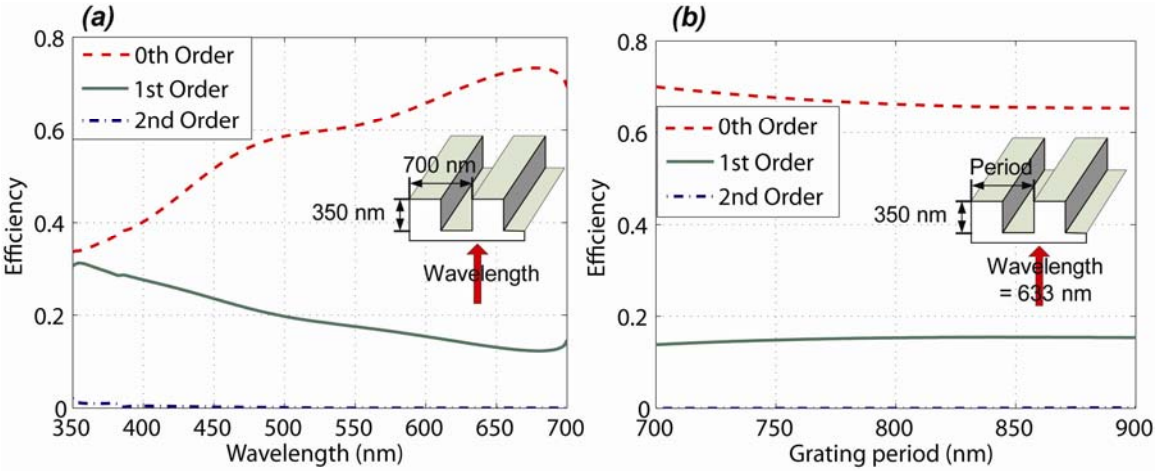

Figure 3.3: Grating efficiency simulations run on GSolver. (a) Efficiency for the visible spectrum wavelengths of interest. (b) Change in efficiency as the grating period shifts with tuning.

The efficiency of this grating is relatively low, but should still be sufficient for spectral measurements. An increase in efficiency can be accomplished by implementing a new master mold grating in our fabrication process. A Bragg-condition transmission

grating with surface modulated patterns of fine pitch that is comparable to the optical wavelength can be utilized. Gratings of this type usually deliver high (~ 90%) first order efficiency almost completely free from polarization effects at a high diffraction angle. The fine grating pitch serves to maintain the high efficiency for a wide wavelength range [48]. Previous research [79] indicates that the first-order diffraction efficiency of Bragg-condition transmission gratings is given by

$$\eta_1 = \sin^2\left(\sqrt{\nu_1^2 + \xi_1^2}\right)\left[1 + \left(\xi_1/\nu_1\right)^2\right]^{-1} \tag{3.8}$$

where the non-dimensional parameters ν_1 and ξ_1 are determined by the grating groove depth, grating period, the refractive index of the grating material, and the incident angle. Based on a model approximating the grating profile to be sinusoidal, the efficiency is above 90% when the aspect ratio of the grating groove becomes nearly 2 for the index of PDMS ~1.45. Following this guideline, we could design the profile of the gratings and fabricate the silicon template used in the device processing. This higher value of grating efficiency could increase the overall sensitivity of our spectral measurements.

3.3 MEMS Design

For the tunable grating described above, the device must be capable of producing high strain of the microbridge at fast speeds. A large strain value of at least 10% will lead to a significant tunable range of the grating period needed to cover a large range of wavelengths in the single point detector setup. Several MEMS actuators [80] were investigated to supply the required level of force, displacement, and speed. Thermal actuators do not provide sufficient speeds and could damage the PDMS with heating. Piezoelectric actuators do not have enough throw and typically actuate out of the plane of the wafer making the grating strain less efficient. Electrostatic comb-drive actuators are the most suitable fit for these actuation requirements and also generate desirable in plane movement. Magnetic actuators are another plausible option, but they require more power, and complex fabrication. A comb-drive's actuation speed is limited by its spring stiffness and mass, which make speeds over 1 kHz easily possible for an appropriately

designed system. Several components of the MEMS design are discussed in further detail in the following sections.

3.3.1 Comb-Drive

The electrostatic actuator chosen in this study is the comb-drive. Many studies have been done on comb-drive designs for relatively large displacement (5-150 μm), high actuation forces and fast speeds [81-85]. The force of an electrostatic comb-drive in the lateral deflection direction is given by

$$F_e = \frac{1}{2}\frac{\partial C}{\partial x}V^2 = \frac{N\varepsilon_0 t}{g}V^2 \tag{3.9}$$

where C is the capacitance, x is the displacement in the desired longitudinal direction, N is the number of electrode fingers, V is the voltage, t is the in-depth thickness, and g is the gap between fingers. To maximize the force, the comb-drive is fabricated from a silicon-on-oxide (SOI) wafer allowing for 50 μm thick single crystal silicon. The gap, g, is set to a minimal distance that does not affect side instability at large displacements. The maximum practical voltage actuation for our device is 150 V. The number of comb fingers can then be calculated for the needed force, keeping in mind that adding more fingers increases the size and may possibly require another set of silicon springs.

3.3.2 PDMS Bridge

The tunable grating structure is fabricated from the polymer PDMS for several important reasons. PDMS is has a relatively low Young's Modulus of 750 kPa to 2 MPa depending on the curing process and mixing ratio of curing agent to base. High elastic strains are also possible allowing for a large tunable range of the grating with minimal force. The bridge is attached to the top of the comb-drive. While being stretched, the bridge itself acts as a spring in the mechanical system and resists the displacement. The force required to stretch the PDMS can be calculated as the following using structural mechanics:

$$F_P = k_P x = \frac{A_c E_P}{L_P} x \tag{3.10}$$

Where k_P is the spring constant of the PDMS bridge, x is the distance the bridge has stretched, A_c is the cross sectional area of the PDMS bridge, E_P is the Young's Modulus, and L_P is the length of the bridge. To minimize the force needed the thickness is fabricated to the smallest thickness possible that does not create additional fabrication difficulties. The length and width are important parameters because they determine the overall grating area for the optical signal. A larger area gives a better optical resolution seen in Equation 3.6, but more force and larger displacements are needed. The length of 200 μm and width of 100 μm is decided as the optimal dimensions with sufficient resolution and minimal required force.

3.3.3 Silicon Springs

Perhaps the most important element of the MEMS design is the silicon springs. These springs provide structural rigidity and rotational stiffness to prevent the snap-in failure of the comb-drives. Electrostatic forces also exist on the teeth of a comb-drive in the lateral direction. Figure 3.4 illustrates the direction of lateral movement. Normally, these forces balance out and minor disturbances are not enough to overtake the silicon springs. However, with higher voltage and increased deflection, the forces become larger, and a small disturbance can create instability causing a catastrophic failure as the teeth are pulled together. To achieve large displacements and avoid snap-in, the springs must be very compliant in the desired longitudinal direction of movement while stiff in the lateral direction.

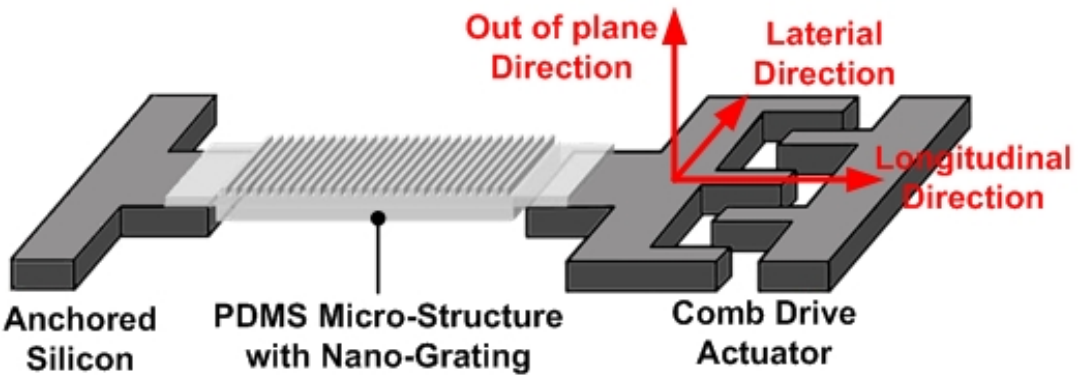

Figure 3.4: Illustration of the MEMS design with the labeled directions of movement.

To meet these requirements, several studies have investigated folded flexures, crab leg configurations, and tilted folded beams [82, 83, 85]. For this MEMS design, the PDMS bridge also plays an important role in spring selection. With the bridge attached on top of the silicon, its spring force is off center and does not act at the center of the comb-drive thickness. The spring force tries to pull the actuator out of the plane of the wafer. Therefore, the silicon springs must be stiff in the out-of-plane rotational direction as well. The PDMS bridge may also be slightly misaligned with the center of the comb-drive in the lateral direction. If the springs are not stiff enough in the lateral direction, misalignment of 1 or 2 μm can be enough to pull the comb-drive off the direct center displacement and lead to snap in failure.

The silicon springs selected for the MEMS comb-drive are sets of straight clamped-clamped beams. With the beams in sets, the combined springs create a structure that is stiff in the lateral and out-of-plane directions. The beams are fabricated as long (800 μm) and as thin (5 μm) as is allowed from the fabrication process. For small displacements the silicon spring constant can be derived from structural mechanics and is calculated as

$$k_{Sx} = \frac{2E_S t b^3}{l^3} \times N_S \tag{3.11}$$

Where E_S is the Young's modulus of silicon, b is the beam thickness, t is the height, l is the length of the beam, and N_S is the number of silicon spring sets. For larger displacements, however, the springs begin to behave nonlinearly. Extensional axial forces develop in the beam and create a nonlinear force-displacement relationship. The stiffness dramatically increases with increasing displacement. The displacement-force

relationship is calculated by modeling them as a clamped-clamped beam with a force on the center.

The derivation for this model can be found in [86]. The relationship between force and displacement for a single beam is given by the equations:

$$F_S = \frac{8E_S I(2I/A)^{1/2}}{l^3} u^3 \left(\frac{3}{2} - \frac{1}{2}\tanh^2 u - \frac{3}{2}\frac{\tanh u}{u} \right)^{-1/2} \tag{3.12}$$

$$\delta = 2\left(\frac{2I}{A} \right)^{1/2} (u - \tanh u) \left(\frac{3}{2} - \frac{1}{2}\tanh^2 u - \frac{3}{2}\frac{\tanh u}{u} \right)^{-1/2} \tag{3.13}$$

for

$$u = \frac{l}{2}\sqrt{\frac{S}{E_S I}} \tag{3.14}$$

where F_S is applied force, δ is the displacement, I is moment of inertia of the beam, A is cross-sectional area of beam, and S is the internal axial force considered constant along the bar. With S unknown, Equation 3.12 and 3.13 must be solved simultaneously for varying values of u to determine the force-displacement relationship.

The cross section of the silicon beams is designed to be rectangular with perfectly vertical walls, however, actual fabrication of beams with DRIE can create beams with slanted side walls. This effect is dependent on the specific DRIE process and also the etched pattern. Larger openings etch faster with DRIE creating beams that are thinner at the bottom of the etch pit as apposed to the top. For best uniformity of the sidewall profile, H-fins are placed onto the beams. The H-fins help control the DRIE etching while having minimal effect on the stiffness (increases ~1%) and the moving mass [82]. Even with the H-fins, the beams vertical walls tend to slant slightly inward. This effect changes the moment of inertia as well as the cross sectional area. Calculating the effect of DRIE is given in [87]. The etch profile is difficult to reliably control and is taken into consideration later when comparing our model to experimental results.

3.3.4 Mechanical Model

The force-displacement relationship of both the PDMS bridge and silicon springs is taken into consideration for developing the mechanical model of this MEMS actuator. The total force needed for displacing the system is the addition of the force needed for the silicon springs and the PDMS bridge. It can be calculated by the equation:

$$F_{total} = N_S F_S(\delta) + F_P(x) \tag{3.15}$$

where N_S is the number of silicon springs which are all acting in parallel. However, one problem is that x and δ may not be the same for the system due to the internal stress of the PDMS bridge. When the PDMS is cured, it retains a tensile stress. Once the bridge is released and suspended during fabrication, the volume shrinks, and the length will decrease approximately 2.5% [88]. This internal stress pulls the comb-drive in the opposite direction of actuation, and the silicon springs have an initial displacement behind their rest position, illustrated in Figure 3.5(a). When actuated the suspended silicon moves to a positive deflection point, seen in Figure 3.5(b). The force-displacement relationship of the silicon springs in the opposite direction is the negative of the forward relationship due to symmetry. The force-displacement relationships of the silicon springs, PDMS bridge, and combined system are plotted in Figure 3.5(c) with the offset included, where deflection is measured from the position of the silicon springs being perfectly straight. The graph shows that the forces needed for displacement are mainly due to the PDMS bridge at small displacements and dominated by the silicon springs at larger displacements. The comb-drive is then designed to be able to generate these relatively high forces for large displacement of the total system and also retain the highest actuation speed possible determined by the resonant frequency.

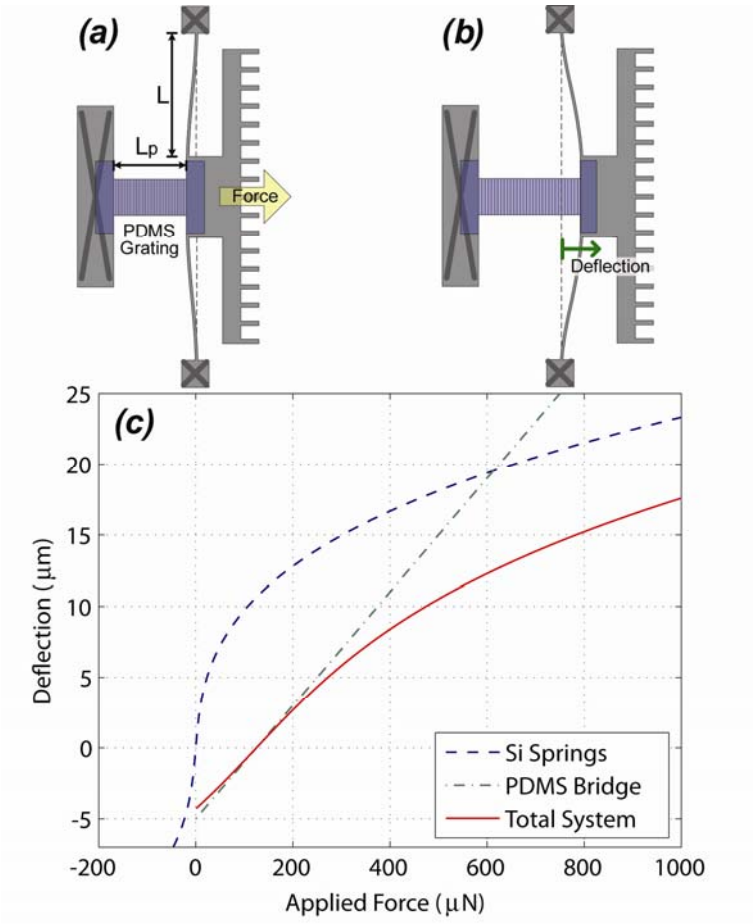

Figure 3.5: Theoretical model of the force-displacement relationship. (a) Illustration of the device at its rest position. (b) Device displacing with actuation. (c) Calculations for the force-displacement of the silicon springs, PDMS grating bridge, and combination of the two. The pitch of the PDMS grating is varied by stretching actuation. The zero deflection point refers to the point where the silicon springs are perfectly straight.

3.3.5 Actuation Frequency

The speed of actuation of the device is limited by the frequencies of the resonant modes. The device can be modeled as a single degree of freedom system, and the fundamental mode in the direction of actuation is calculated by

$$f_0 = \frac{1}{2\pi}\sqrt{\frac{k_x}{m_S}}, \tag{3.16}$$

where k_x is the total spring constant in the longitudinal direction, and m_S is the mass of the moving portion of the actuator. The spring constant k_x is calculated by summing the

spring constants of the silicon springs and the PDMS bridge which all work in parallel. The silicon springs, however, are nonlinear and the spring constant changes with increased deflection. The linear model in Equation 3.16 is used as the lower bound estimate of the resonant frequency. The mass of the device is calculated by multiplying the structural volume times the density of the silicon. The silicon springs and the PDMS mass only partially move but are included in the mass to estimate the lower bound frequency. The resonant frequency is calculated to be 5.54 kHz. A more accurate estimate can be made using finite element analysis [82], but this lower bound value is more than sufficient for the targeted 1 ms cycle time.

This chapter has specified the spectroscopy system and designed the MEMS device to fit these requirements. The concept of how to take spectral measurements with a tunable grating and single detector has been introduced, as well as the advantages of a PMDS-silicon hybrid MEMS device. The next chapter uses this information to fabricate and test the MEMS device.

Chapter IV

Fabrication and Characterization Measurements

This chapter discusses the fabrication and measurements taken with the designed device from the previous chapter. Once the photomasks are laid out using computer-aided design (CAD) software, we fabricate the MEMS devices in a cleanroom facility. All processing is completed at the Lurie Nanofabrication Facility at University of Michigan, Ann Arbor. The next section describes the details of this processing.

4.1 Fabrication

Our PDMS-silicon hybrid microsystem construction method employs a multistep process that fabricates PDMS and silicon structures independently before assembly. The process involves three major steps: (1) formation of the PDMS structures through soft lithography and sandwich micromolding, (2) fabrication of the MEMS structures through standard silicon bulk micromachining, and (3) surface tension-assisted precise alignment/bonding and release of the molded PDMS layer onto the silicon structures. These steps meet the following outstanding technical requirements: (i) the PDMS micromolding process needs to be compatible with silicon MEMS fabrication, (ii) the entire integration process needs to be performed at low temperature to maintain their compatibility with CMOS technology, and (iii) the PDMS-silicon hybrid microstructures need to be assembled in high precision (an alignment error $< \pm 2$ μm) without debonding and delamination. The entire process requires four lithography masks. Two are needed for the PDMS mold fabrication, one for the front side of the MEMS structure, and one for the MEMS backside. A grating mastermold for nanoimprinting is also required.

Figure 4.1 shows the fabrication process of a device. The process starts by first fabricating the top and bottom molds to form the PDMS into the desired microstructure shape. For the top mold in Figure 4.1(a), photoresist is spun onto a transparent glass wafer and then cut into 2 cm square die pieces. The photoresist is nanoimprinted at 170°C and 4500 kPa using a silicon master mold of periodical surface nanopatterns fabricated by electron beam lithography, which can be shaped into an array of gratings, pillars, circular grooves, or any other arbitrary structures. The imprinting is done with a full-wafer universal imprinter (NX-2000, Nanonex). The bottom mold in Figure 4.1(b) is made by a two step DRIE using ultraviolet lithography for patterning. A thin carbon fluoride (CF_x) coating is applied to prevent the PDMS from sticking to the bottom mold.

The top and bottom molds are then configured to create the PDMS microstructures as shown in Figure 4.1(c). PDMS is mixed using the Sylgard 184 silicone elastomer kit (Dow Corning Corporation, 10:1 base-curing agent ratio), and a small drop is placed onto the bottom mold. The top and bottom molds are sandwiched together, and the PDMS is cured at 150°C and 4500 kPa for 45 minutes. As the PDMS cures, it conforms to the shapes of the two molds, taking the form of both the microstructure and the nanoscale surface pattern. Once cured, the bottom mold is removed, and the molded PDMS stays attached to the top mold.

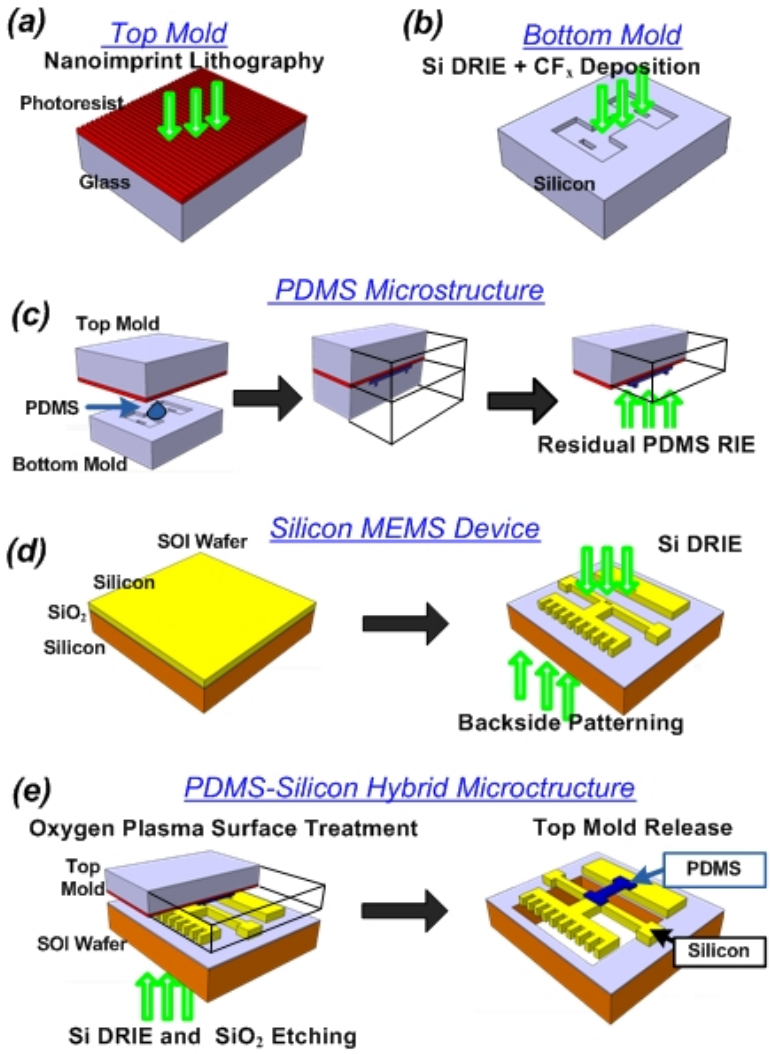

Figure 4.1: Fabrication process of the PDMS-Silicon hybrid microsystem. (a) Photoresist is spun onto glass and nanoimprinted for the top mold. (b) The bottom mold is a two step DRIE of silicon followed by CF_x deposition. (c) The top and bottom mold shape the PDMS microstructure with the submicron grating on the top surface. (d) An SOI wafer is patterned and etched to make the MEMS structures. (e) The top mold and SOI wafer are treated with oxygen plasma, aligned, and bonded. The backside and oxide layer are etched, and the top mold is released by dissolving the photoresist.

On a separate SOI wafer, the silicon MEMS device is fabricated shown in the fabrication step in Figure 4.1(d). The back and front of the wafer are patterned with photoresist, and the front side is etched with DRIE down to the oxide layer. The created MEMS structures are 50 μm thick and made from single crystal silicon. The wafer is cut into 2 cm square dies with approximately 40 MEMS structures on each die. The SOI wafer and the PDMS microstructure attached onto the top mold are next combined to create the PDMS-silicon hybrid microstructures as shown in Figure 4.1(e). Both pieces

are treated with oxygen plasma to activate the surfaces and promote the permanent bonding of PDMS and silicon. A drop of water is placed on the SOI die, and the top mold is positioned on top. The three-dimensional PDMS structure is designed to fit into position holes of the silicon MEMS. The water surface tension assists with alignment until the PDMS falls into the correct location of the MEMS device. Figure 4.2 displays a cross-sectional illustration of the alignment and bonding. The alignment accuracy for this step is approximately 2 μm. After water evaporation, the PDMS is permanently bonded to the silicon by silicon-oxygen covalent bonding [89]. The back side of the SOI wafer is etched through and the oxide layer is removed to suspend the MEMS device. Finally, the photoresist of the top mold is dissolved to release the PDMS microstructures from the top mold. The final device has suspended silicon MEMS structures with PDMS attachments which contain a submicron pattern on the PDMS top surface.

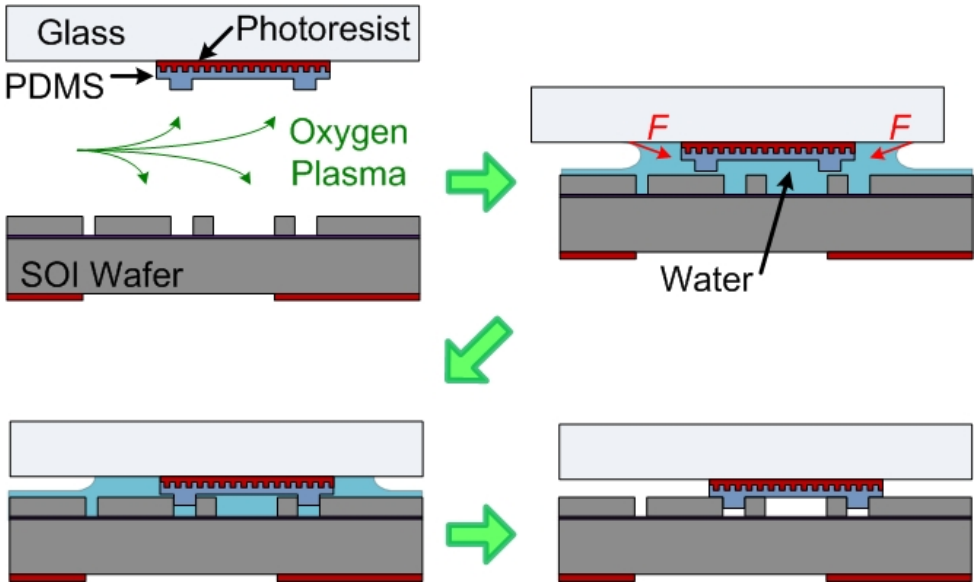

Figure 4.2: PDMS-Silicon alignment and bonding process in fabrication. Si and PDMS structures are treated with oxygen plasma. A drop of water is placed on the bottom mold, and the top mold is placed on top. With the assistance of water surface tension, the structures are aligned. The water is evaporated allowing for permanent bonding between the Si and PDMS.

Figures 4.3(a-c) show the SEM images of the PDMS microbridge connected on one side to a silicon comb-drive with the other side connected to fixed silicon. The microbridge contains a nanoimprinted grating pattern on the top surface as shown in Figure 4.3(d). The entire bridge is 200 μm long, 100 μm wide and 15 μm thick, and the

grating pattern has a period of 700 nm. The devices are next experimentally characterized and tested as high speed tunable gratings.

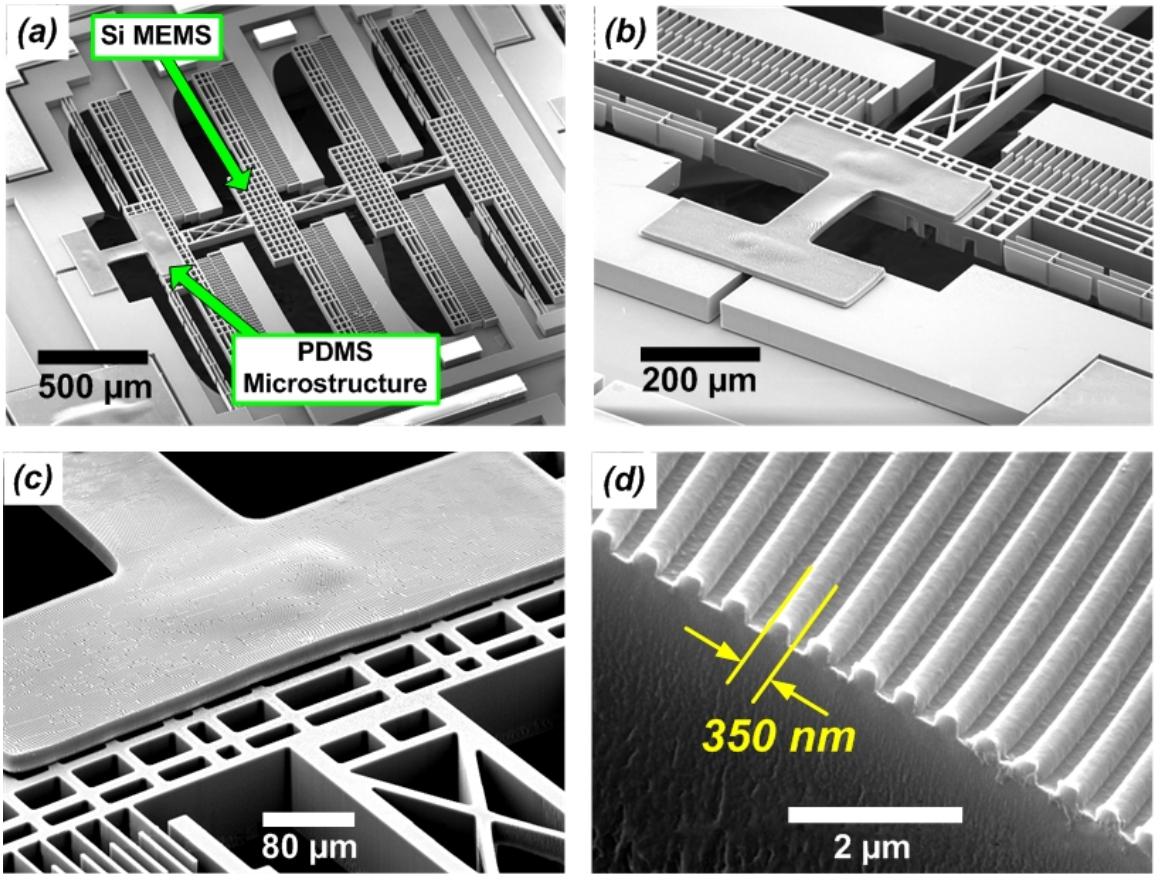

Figure 4.3: SEM images of device. (a) Image of entire MEMS device. (b) Closer view of the suspended PDMS bridge connected to the silicon comb-drive. (c) View of the PDMS-Si attachment interface. (d) Zoomed image of the edge of the PDMS bridge showing the nano grating.

4.2 Experimental Characterization

With successful fabrication, the MEMS devices are tested and characterized. An actuation voltage is applied to the comb-drives and the device's displacement is large enough to visually confirm with an optical microscope. Figure 4.4 shows optical images of the comb-drive at rest and displaced when voltage is applied. The PDMS bridge is extended as designed. Further experiments are conducted to test the devices bond reliability and grating tunability.

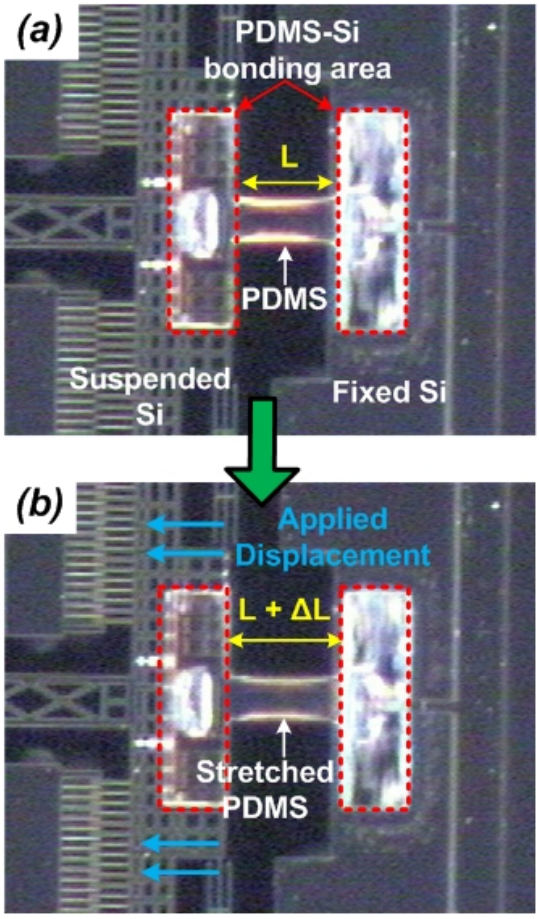

Figure 4.4: Optical images of the MEMS tunable grating. (a) PDMS bridge at initial position. (b) Bridge strained by MEMS actuator.

4.2.1 Bond Reliability

The reliability of the silicon-PDMS bond is tested. A PDMS microbridge is attached to two suspended silicon structures that are pushed apart using probe tips. Optical images are taken, and the PDMS bridge is measured to stretch over 40% without the silicon-PDMS bond breaking as seen in Figure 4.5. The corresponding stretching force is on the order of several millinewtons, which is approximately four times larger than the actuation force used in our normal conditions. The PDMS was then stretched to failure, and the bridge itself ripped before the silicon-PDMS bond was broken. The strong bond also sustained the stretching actuation of the PDMS microbridge by the MEMS actuator for over 100 million cycles.

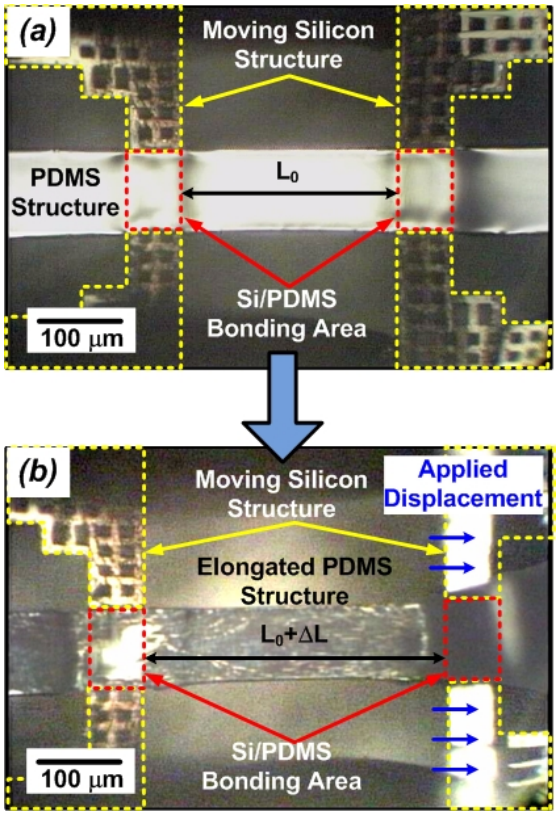

Figure 4.5: Images from the bond reliability test. (a) A test structure at its initial state. (b) The test structure with the PDMS bridge stretched 40% using mechanical probes.

4.2.2 Tunable Grating

Since little data exists for the mechanical behavior of cross-linked PDMS at the size scale of our microsystem, we first set out to study its response to microscale actuation. To test the device, we implemented it into an optical experimental setup illustrated in Figure 4.6, which directed laser light to pass through the transmission grating from the underside of the device. A position sensitive diode (PSD) (C4674, Hamamatsu Photonics) tracked the changing first-order diffraction angle of a monochromatic source and hence the change in grating period. The calculations for this characterization revolve around basic geometry and the transition grating equation. From before, the shortened version of the grating equation given in Equation 3.2 is $\lambda = a \sin \gamma$. Measuring the variations in γ for normally incident monochromatic light through the grating allows us to determine the variation in the grating period, a.

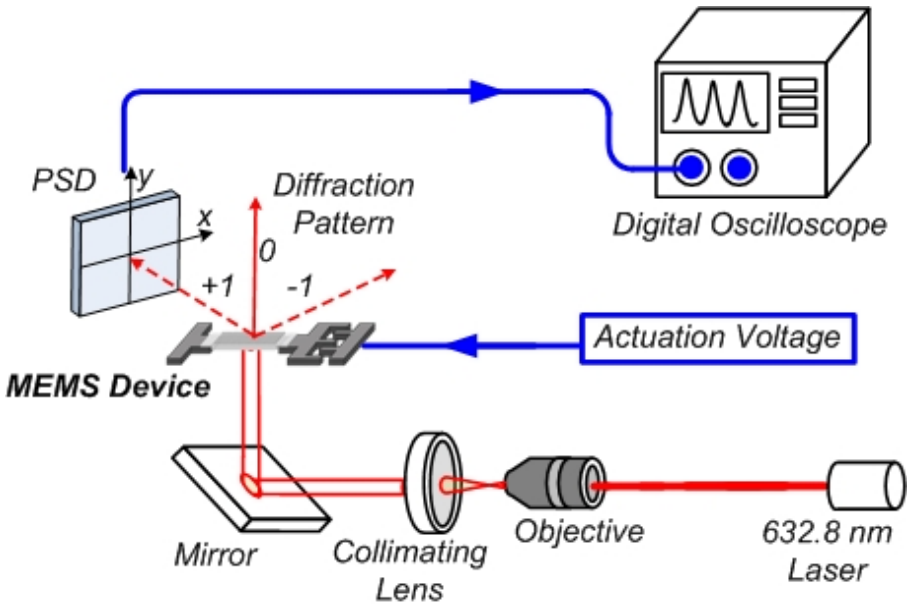

Figure 4.6: The optical setup for device characterization. The PSD measures the movement of the laser spot diffracted at the first order. This data is used to calculate the change in diffraction angle and the shift in grating period.

Using the PSD experimental setup with a 632.8 nm Helium-Neon laser (25-LHP-991-249, Melles Griot), we used the change in a to measure the PDMS engineering strain at quasi-static conditions by applying an sine wave voltage of 0-150 V at 0.1 Hz onto the silicon comb-drives. The PDMS strain varied from 0 to 13% over the voltage cycle. This measurement is compared to our theoretical force-displacement model. The voltage needed to generate the actuator force is calculated by rearranging the comb-drive equation given in Equation 3.9. The resulting equation is the following:

$$V = \sqrt{\frac{F_e g}{N \varepsilon_0 h}} \,. \tag{4.1}$$

The theoretical model generally agrees with strain profile of the experimental results as seen in Figure 4.7. Several possible imprecise values in our theoretical model may lead to slight variations from the experimental results. The Young's Modulus of single crystal silicon can depend on the doping variations of the wafer. The Young's Modulus of PDMS is dependent on the curing process and exactness of the curing agent to base ratio. Also mentioned before, the DRIE etch of the silicon plays a role in the exact profile of the silicon springs. These values are tuned in their acceptable ranges to help fit the model

as best possible to the experimental results and thus have an accurate strain-voltage prediction needed for spectroscopy measurements.

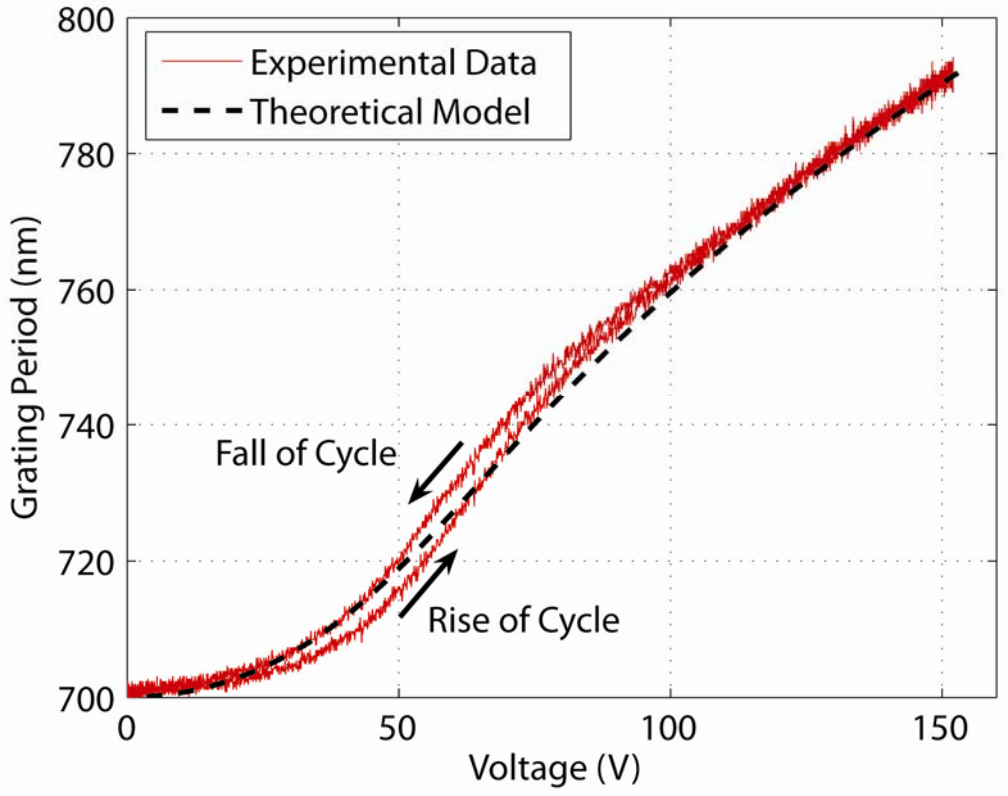

Figure 4.7: A plot of the PDMS bridge's strain verses the actuation voltage of the MEMS device.

Still, discrepancies are present and likely due to the PDMS strain not acting linearly with force. Hysteresis is also evident as the profile differs for the rise and fall of the strain cycle. From these results, it is evident that further experimentation is needed to fully characterize the PDMS's strain response.

4.2.3 PDMS Strain Response

Several experiments were run to further investigate these nonlinear effects in the straining of the microbridge. First, the PDMS grating was held at a constant force over time to see if the material displayed creep behavior. A voltage of 150V was applied and held constant, and the strain of the PDMS was optically measured by tracking the change in first order diffraction. The strain of the PDMS microbridge was plotted over time in

Figure 4.8 and showed change of strain of 3.0×10^{-3} after 20 minutes. For this level of strain creep, the drift in wavelength for spectroscopic measurements is calculated from Equation 3.2. For a wavelength of 633 nm, the drift equates to 1.9 nm. The creep of the PDMS may cause inaccurate spectroscopic measurements and needs to be taken into consideration.

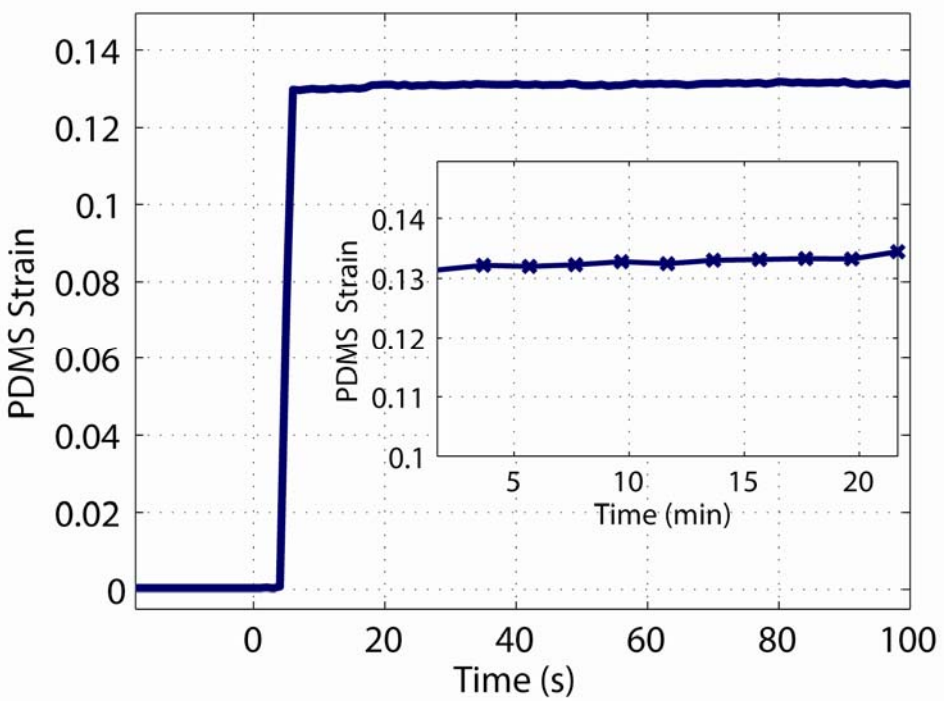

Figure 4.8: Plot of the PDMS strain for an extended time with the actuation voltage increased then held constant. Inset graph shows the data continuation over 20 minutes.

The repeated straining of polymers also has an effect on their stress-strain behavior. A stress-softening phenomenon known as the Mullins effect occurs in many polymers. As the polymer undergoes multiple strain cycles, the response can shift towards a more elastic material. This effect has been studied in PDMS [90] although the polymer physics behind the phenomenon is still not entirely understood [91]. The rate of applied stress on a polymer also has an effect on the strain response. Chen et al. [92] developed a model for rate dependent stress-strain relations, but also came to the conclusion that any elastomer needs to be accurately characterized individually.

Subsequently, an experiment was set up to measure the strain rate effect of the device. PDMS strain during the rise and fall of an actuation cycle of a 20-160 V sine wave at 2, 20, 200, and 2000 Hz was measured to study the dynamic response of our device to

different strain rates. Figure 4.9 shows the results of these experiments. The 2 Hz strain cycle not shown matched the 20 Hz cycle closely. For higher frequencies the maximum strain tends to drop while the asymmetry of the rise and fall cycle becomes more pronounced. With all four frequencies below the calculated resonant frequency of 5.54 kHz for the MEMS device and the electrostatic force being dependant only on voltage amplitude, it is believed that the change in the strain cycle with the frequency should be caused by the PDMS's strain rate-dependent response.

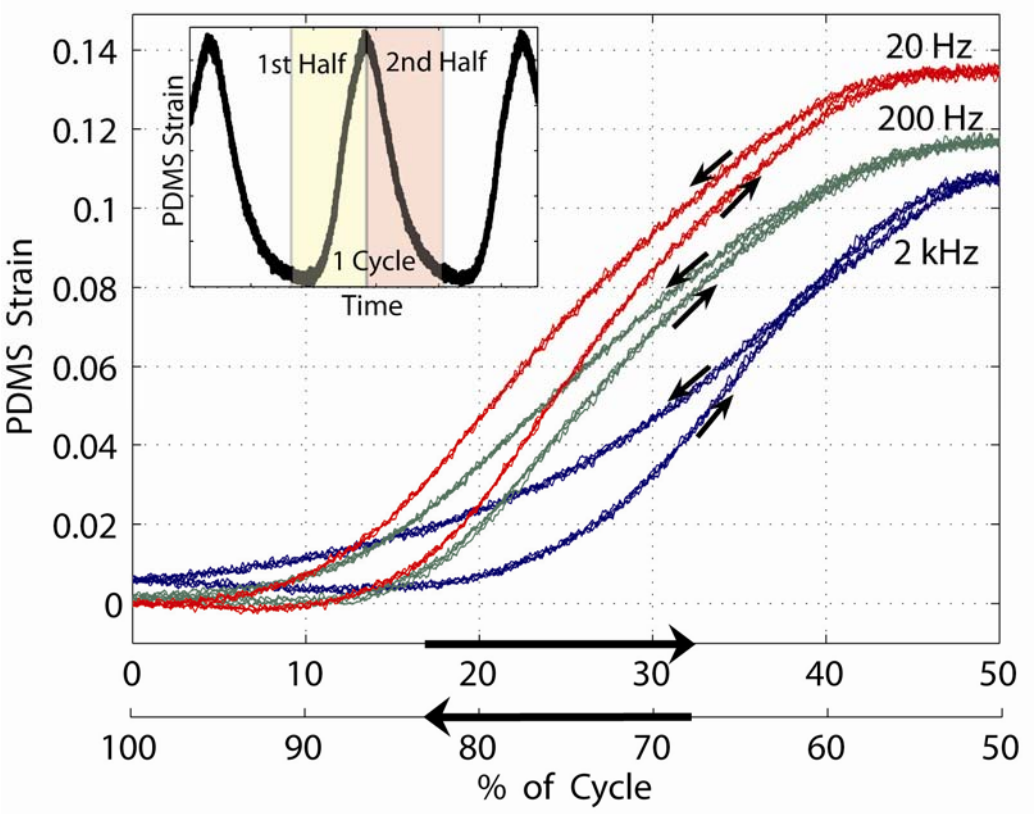

Figure 4.9: Cyclic PDMS strain at varying actuation frequencies. Graph plots the first half of each cycle next to the second half of cycle for comparison. Small arrows indicate the direction of the rise and fall of the cycle. Inset labels the first and second half of each strain cycle.

The device was also tested for drift of the PDMS strain over repeated cycling displayed in Figure 4.10. The device actuation voltage was a 20-160 V sine wave at 200 Hz. The rise and fall strain cycle was measured every 20 minutes for an hour. The maximum deviation between the cycles and the initial cycle was plotted over time. The PDMS strain varied up to 1.7×10^{-3} after one hour of cyclic straining.

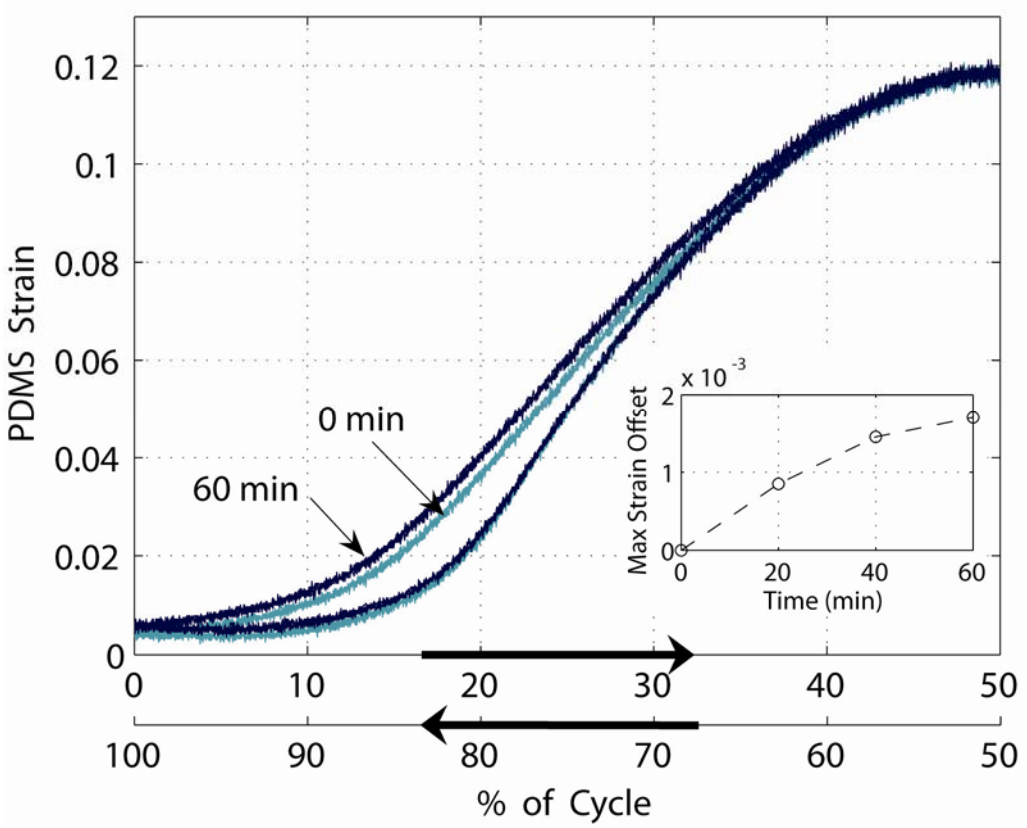

Figure 4.10: The change in PDMS cyclic strain over time. The actuation frequency was 200 Hz. Inset graphs the maximum strain offset from the initial condition at 0 min.

Through our experimentation we have observed a deviation of the device's behavior from the theoretical prediction in Figure 4.7. This is most likely a result of the nonlinear stress-strain behavior of the PDMS microbridge. In particular, elastomers are commonly known to exhibit signs of hysteresis, cyclic softening, and rate-dependence in their mechanical behavior [91, 93, 94]. Our above data indicate these characteristics for the microscale PDMS structure, thus warranting much care for practical operation of the device. Here, the PDMS response to cyclic loading is difficult to predict as a function of voltage amplitude and frequency using the theoretical model. Therefore, we determine the grating period of the PDMS structure as a function of the location within a full cycle at a given voltage amplitude and frequency directly from the experimental data. The very repeatable and predictable dynamic response of the PDMS structure under a fixed condition makes this approach valid. To eliminate errors resulting from the creep or drift of the PDMS over time, a quick calibration measurement is taken after every 10 minutes of actuation using a monochromatic light source and the PSD. While the ultimate

lifetime of the PDMS has not been experimentally measured, one device has seen approximately 50 hours of use and 3.6×10^{8} cycles and is still accurate after calibration.

4.3 Spectral Measurements

After the characterization measurements, the device was next tested for spectroscopic measurement applications. We implemented the device into an optical experimental setup capable of directing laser light to pass through the grating at various wavelengths, intensities, and frequencies. The setup is illustrated in Figure 4.11. A voltage actuation of 20-160 V at 2 kHz was applied to the MEMS actuators. Before our first measurement, the PSD tracked the changing first-order diffraction angle of the -1st order diffraction (Figure 4.11, setup 1). The grating period changing with time is plotted in Figure 4.12(a). This data along with the grating equation (Equation 3.2) can be used to calculate the wavelength incident at a specific angle in the first order diffraction. The results of this calculation are seen on the right ordinate of Figure 4.12(a).

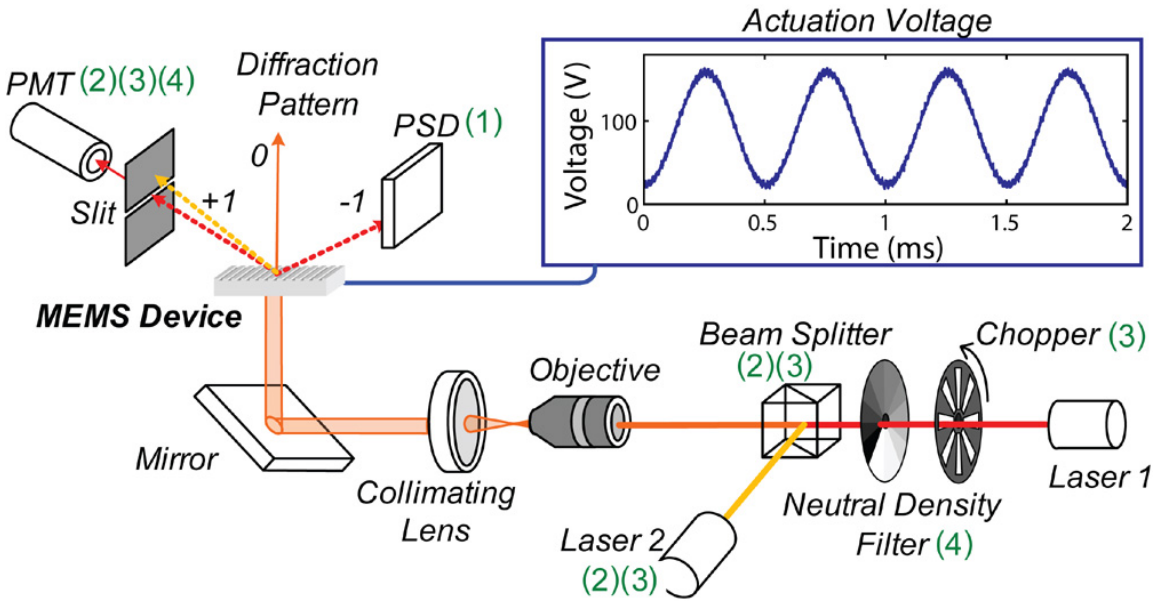

Figure 4.11: The testbed to conduct four separate optical experiments: (1) Dynamic response measurement measures the change in angle of the first order diffraction of the red laser using the PSD. (2) Spectral acquisition measurement implements the PMT and measures the multiwavelength signal of the 632.8 and 593.5 nm lasers. (3) Variable signal measurement uses the chopper wheel to pulse the red laser. (4) Maximum sensitivity measurement measures the red laser passed through neutral density filters to decrease the optical power to the minimum detectable signal.

With the tunable grating period characterized, spectroscopic measurements were subsequently taken by placing a highly sensitive detector at the specific diffraction angle and comparing the detector's measurements with the wavelength incident onto the detector's slit opening. A PMT (H5784-20, Hamamatsu Photonics) was used to take measurements at the first order diffraction of a specific diffraction angle. To simulate a multiwavelength signal with an unknown spectrum, red (λ = 632.8 nm, 25-LHP-991-249, Melles Griot) and yellow (λ = 593.5 nm, Rigel-2, Laserglow Technologies) lasers were both incident onto the underside of the transmission grating (Figure 4.11, setup 2). The PMT detection signal included two peaks corresponding to the two laser inputs for every wavelength range sweep, or half of the MEMS actuation period, as seen in Figure 4.12(b). This signal was directly compared to the incident wavelength data to determine the intensity at each wavelength. The wavelength intensities were plotted in Figure 4.12(c) to give the spectral acquisition measurement within that particular 250 μs timeframe.

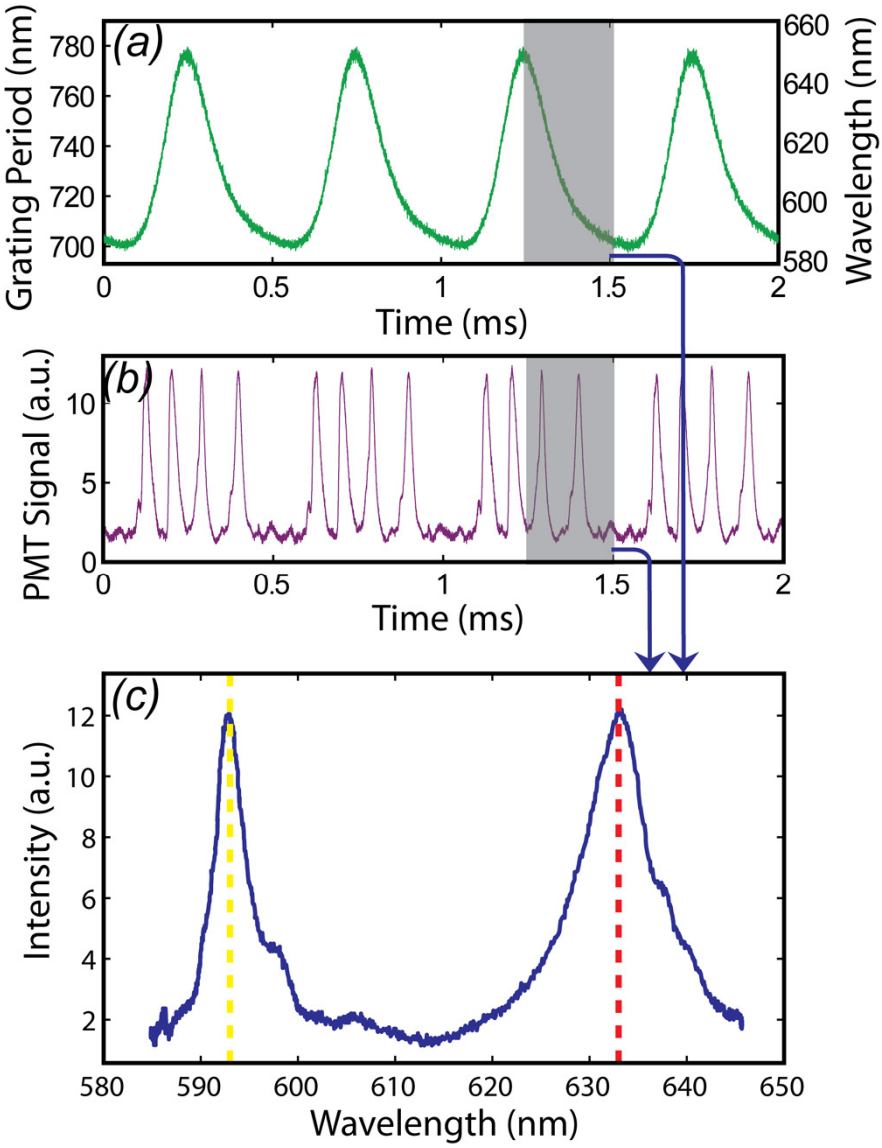

Figure 4.12: Results from the change in grating period and spectroscopy measurements. (a) The time-variation of the grating period calculated from the change in diffraction angle. Right ordinate shows the calculated incident wavelength onto the PMT detector. (b) PMT detection for the two-wavelength signal as the device is being actuated, given in arbitrary units (a.u.). (c) A spectral acquisition taken with one sweep of the device for the two-wavelength signal. Dotted lines mark the exact wavelengths of the lasers being detected.

4.3.1 Variable Signal Measurements

To demonstrate the speed of the spectral measurements, the red laser was pulsed at 1 kHz using an optical chopper (300CD, Scitec Instruments) while the yellow laser remained constant (Figure 4.11, setup 3). Figure 4.13 shows the input signal of the two

lasers measured separately with a photodiode. Each pulse of the red laser lasts 500 μs with a duty cycle of 50%. With this signal incident onto the actuating grating, spectral measurements were taken with the device. The spectral acquisitions were taken twice every millisecond and plotted versus time. The spectral measurements were fast enough to capture the real-time switching of the red laser. Figure 4.14 shows similar data to Figure 4.12 but with multiple cycles taken for spectral measurements. For all four measurements seen in Figure 4.12(c) the yellow laser was detected, and as the red laser was pulsed at 1 kHz, each of the laser's on/off states was still detectable.

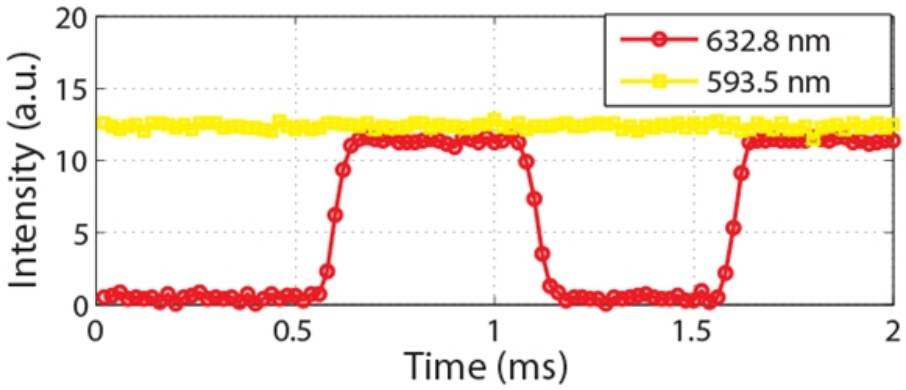

Figure 4.13: Input signals of the red and yellow lasers measured separately. Yellow is constant while red is pulsed at 1 kHz.

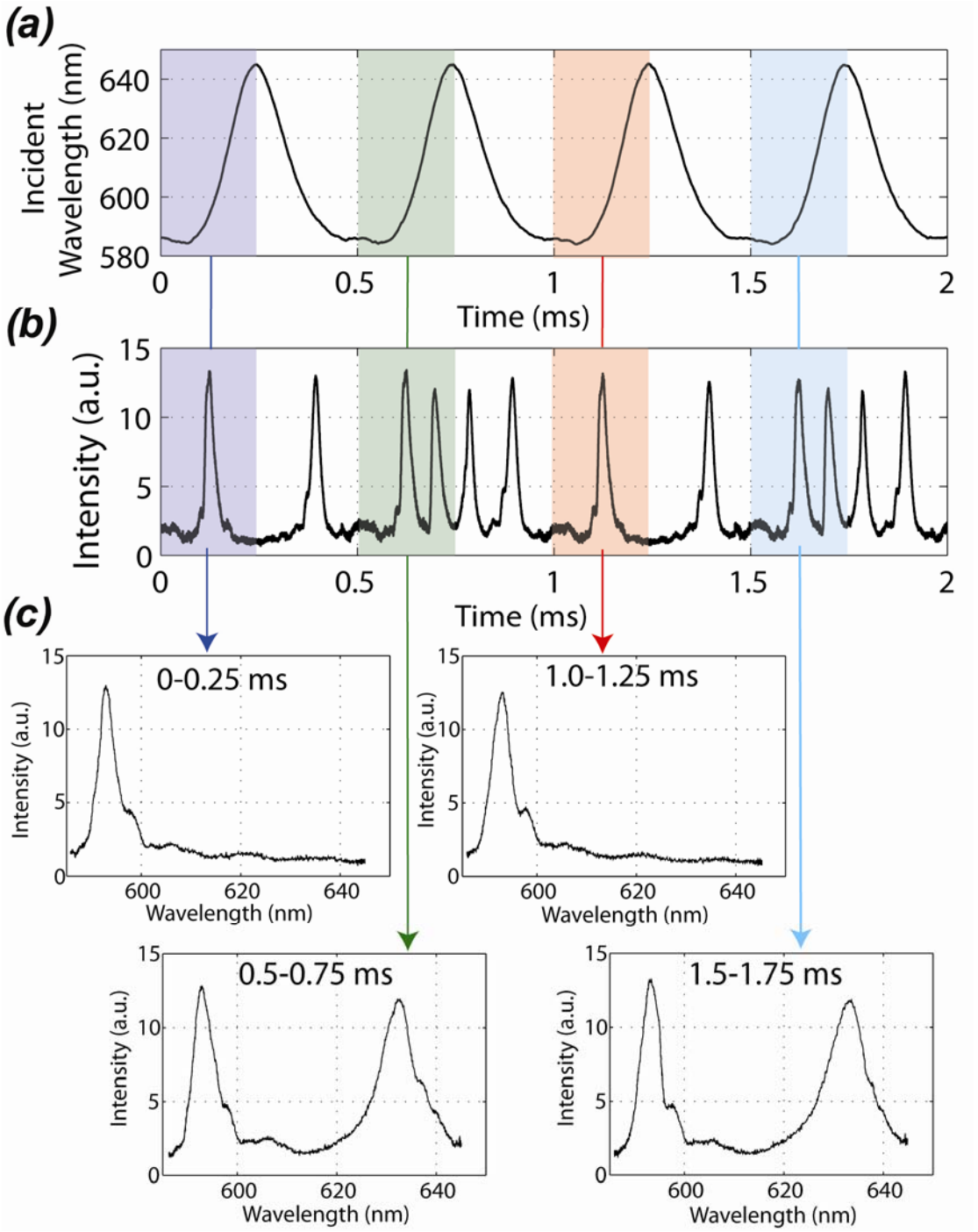

Figure 4.14: Spectroscopy measurements and the corresponding data taken with the MEMS device. (a) The wavelength incident onto the PMT slit calculated from the PSD data and voltage signal. (b) PMT detection for the two-wavelength signal as the device is being actuated. (c) Spectroscopy plots taken by comparing PMT intensity to the incident wavelength. Each graph corresponds to the data in the highlighted regions of graphs (a) and (b). Plots accurately show peaks at the lasers' wavelengths. The plots for different times capture the on/off states of the red laser pulsed at 1 kHz.

To better visualize the measurements taken, the spectral data is plotted versus time along with the two laser inputs. The three-dimensional graph is seen in Figure 4.15. The yellow plane shows the constant yellow laser intensity while the red plane shows the pulsing red laser. The spectral measurements shown in blue accurately detect the yellow laser at all times and the red laser only when a spectral sweep occurs during the "on" state of the laser.

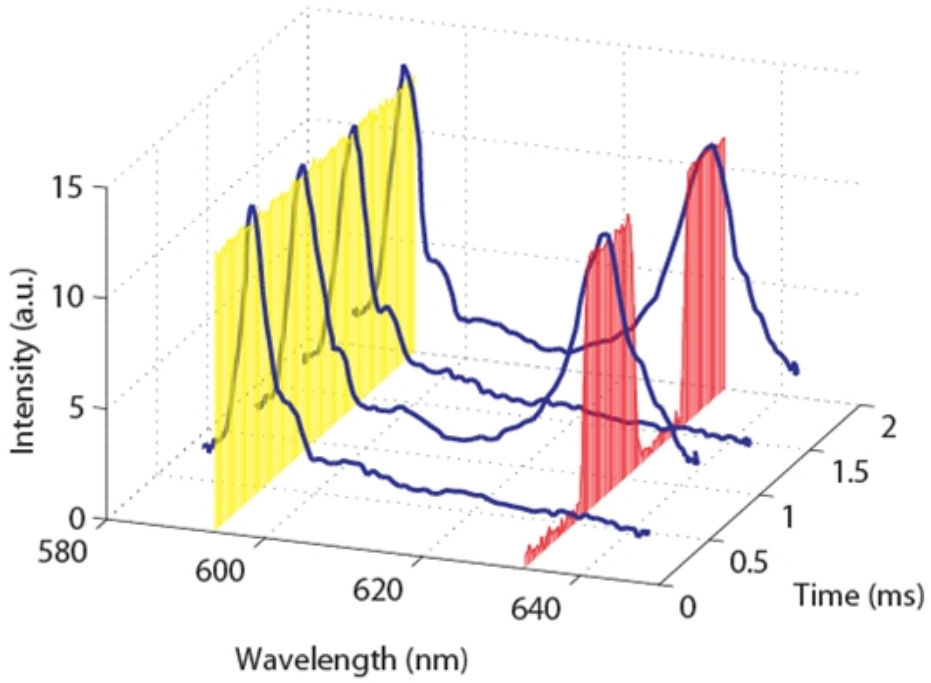

Figure 4.15: Spectral acquisition measurements of input signal plotted versus time.

Other similar spectral measurements are taken for different actuation frequencies and varying spectral signals. With the optical chopper set to 250 Hz, an actuation voltage of 1.5 kHz is applied to the device. A spectral acquisition is taken for every voltage ramp up section of the cycle. The resulting measurement speed is a spectral sweep taken every 667 μs, with a 333 μs acquisition time. Figure 4.16 displays a series of spectral measurements plotted over time. Each blue plane is the resulting measurement of one spectral sweep. The plots correctly show the red laser pulsing at 250 Hz while the yellow laser remains constant.

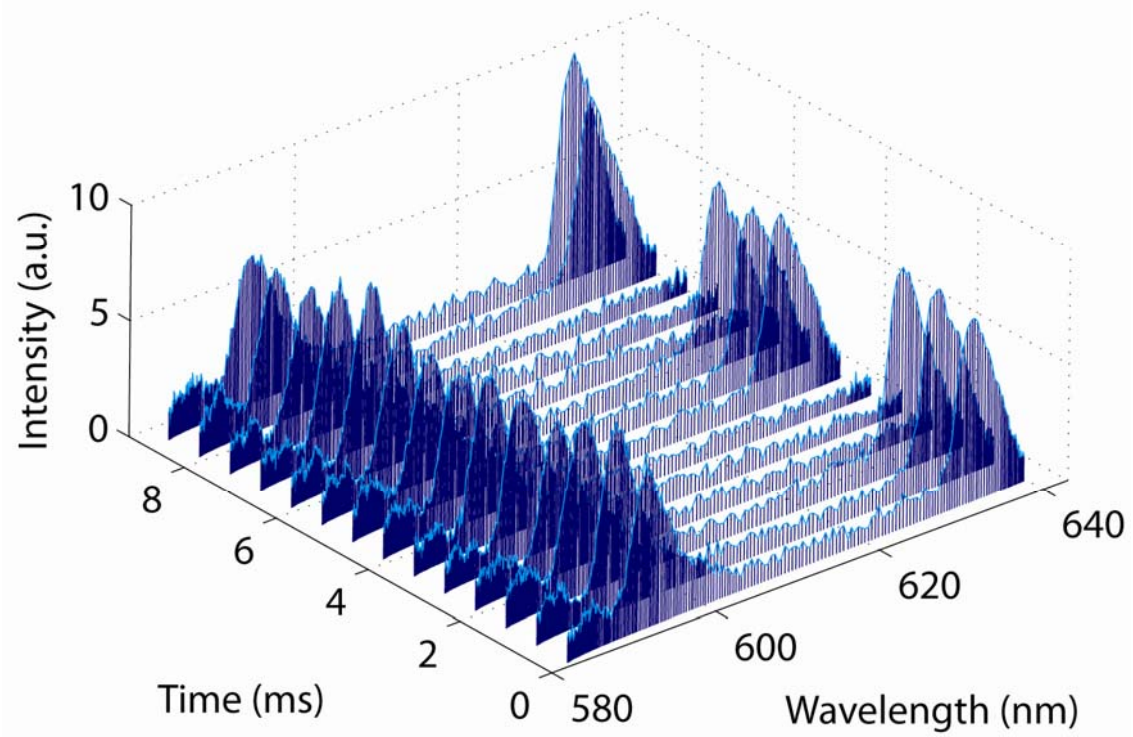

Figure 4.16: Spectroscopy measurements plotted versus time as the red laser was pulsed at 250 Hz and the yellow laser remained constant.

4.3.2 Sensitivity Measurements

To demonstrate the high sensitivity possible with this spectral setup, we calculated and measured the minimum detectable signal (MDS). With the PMT's gain at maximum, the minimum detectable output is determined by the mean plus one standard deviation of the PMT output voltage noise floor [95], which includes dark counts of the PMT, stray light, and other noise sources of the system. The radiant flux that would produce this output value is calculated using the PMT sensitivity and grating efficiency. According to specifications data, the PMT sensitivity at the maximum gain is 78 V/nW. From the grating simulations previously given in Figure 3.2, we determined the grating efficiency to be 13-16% for the first order diffraction for the 595-655 nm wavelength range of interest in this experiment, with negligible variation as the grating period changes from 700-780 nm. The efficiency of the grating was multiplied by the PMT sensitivity and the minimum detectable voltage output to calculate a MDS of 6.49 pW. To demonstrate a detectable signal close to this power level, we dramatically reduced the red laser's

intensity using two neutral density filters (NT54-082, Edmund Optics) and took spectral measurements with the red laser peaks just observable (Figure 4.11, setup 4). Figure 4.17 graphs ten spectral sweeps and shows the red laser peak clearly identifiable in all ten, with the signal average at the laser wavelength being 7.6 dB higher than the noise level. An optical power meter (PDA-750, Terahertz Technologies Inc.) was used to measure the power of the incident laser signal before the grating. A value of 36 pW was measured, which is higher than the calculated MDS value but reaches the lowest level of the incident signal power practically measurable with the power meter. This level of sensitivity is difficult to achieve without the use of a sensitive single point detector or very long integration times of pixel based detectors [33].

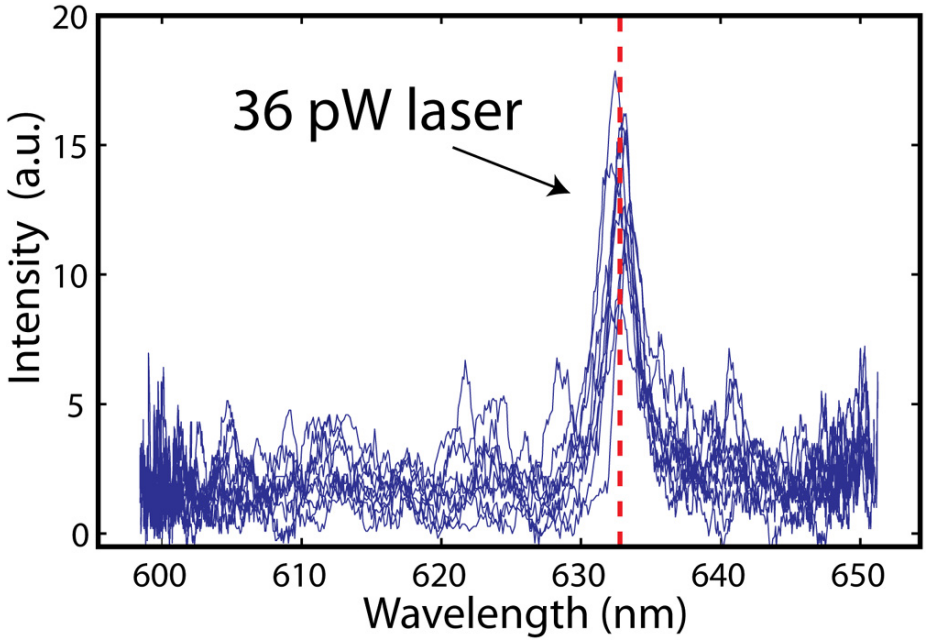

Figure 4.17: Results from the maximum sensitivity measurements. Ten spectral sweeps plotted together. The dotted line indicates the detected laser wavelength at 632.8 nm.

4.4 Spectral Measurement Analysis

4.4.1 Resolution

For these spectral measurements, the resolving power is calculated as $R = \lambda/\Delta\lambda$ from Equation 3.6, where $\Delta\lambda$ is the full-width half-maximum (FWHM) taken at wavelength λ,

and it is assumed that the laser source is perfectly monochromatic. From our results we measured the FWHM for each peak and obtained an R of 119 and 79 for the wavelengths 593 nm and 633 nm respectively. The difference in resolution may be due to the grating tuning, which changes the number of grating grooves the incident beam diameter passes through. For the lower R value of 79, monochromatic peaks in the visible spectrum are resolvable if their wavelengths differ by approximately 5-9 nm. The theoretical spectral resolution limit of $R = mN_g$, where m is the order of diffraction and N_g is the number of grating grooves, is 285.7 for our grating. The current optical setup is purposely kept as simple as possible, but to increase our spectral resolution towards this limit, a focusing element can be inserted after the grating [2]. Better collimation optics before the grating will also increase this resolution.

4.4.2 Speed

The speed of the acquisitions is dependent on the actuation of the MEMS device. A PMT detector does not need signal integration over time, and its measurement capabilities are fast enough that it is not the limiting factor. For the spectral measurements in Figure 4.15 and 4.16, the MEMS device was actuated at 2 kHz and 1.5 kHz, respectively. An actuation speed of 2 kHz translates to the grating going from its rest position to full extension in 250 μs. Every upward cycle was used for the spectral measurements, leading to 2 full measurements taken every millisecond. While the voltage ramp down section of the cycle can also be analyzed for double the acquisitions, a small pause between measurements may be more appropriate in applications to differentiate fluorescence samples in microfluidics.

Because of the nonlinearity of the spring system, the resonant frequency is difficult to measure for this MEMS device, and the maximum speed is unknown. As the actuation frequency increases past 2 kHz, the PDMS strain deviates more and more from the mechanical model. This device, however, was specifically designed for maximum strain within low kHz actuation speed. Other MEMS actuator designs can be made to increase the speed at the expense of strain range if needed for a specific application.

4.4.3 Range

The range of the spectral measurements for this device at the 2 kHz speed is approximately 65 nm. For applications that measure two or three fluorescent colors within close proximity, this range may be sufficient. This range is dependent on the possible strain of the PDMS microbridge, which reaches 11% for this device. The strain is also dependent on the on the particular section of the visible spectrum of interest. To measure different parts of the visible spectrum, the detector angle needs to be adjusted to catch a different section of the first order diffraction. According to Equation 3.2, $\Delta\lambda$ is dependent on the change in period and also the angle. Figure 4.18 shows how a different placement angle of the detector changes the section of the spectrum measured and the spectral range.

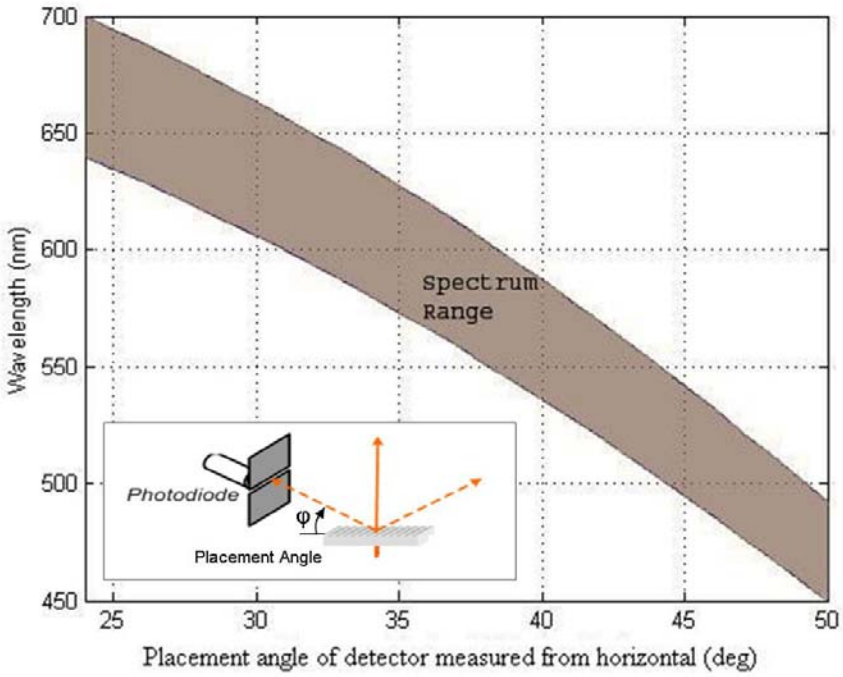

Figure 4.18: Spectral range of the device for a known angle of the photodetector. Inlet figure defines the placement angle.

A higher strain would increase the change in the grating and increase the range of wavelengths swept across the detector slit. The bridge length can also be shortened creating higher strain for the same amount of displacement, but decreasing the bridge length decreases the number of grating grooves and hence the resolution. The easiest

way to essentially double to spectral range is to add another detector at a different angle. Another PMT can be placed in the -1st diffraction order to pick up a separate spectral range of the incident signal. A multianode PMT can also be implemented with only two of the anodes needed.

4.4.4 Sensitivity

To verify the possible high sensitivity of our optical setup, we determined the minimum detectable signal to be 36 pW from a monochromatic source. Fluorescent detectors have an optical power that is spread across a range of wavelengths making it difficult to gauge their minimal detectable signal for a particular wavelength. However, estimates have determined that our device's level of sensitivity is sufficient for detecting many weak fluorescent signals implemented in bioassay labs. In addition, the sensitivity can further be increased by imprinting a grating profile with a higher grating efficiency. The optimization of the slit size will also increase the sensitivity and is discussed in the next chapter.

4.4.5 Complexity

The simplicity of this optical setup also plays a major role in its advantages over other systems. For many optical systems, a direct correlation exists between complexity, cost, and volume. This optical system requires only one photodetector. The high level of sensitivity capable with a PMT is only a fraction of the cost of a CCD array with comparable sensitivity levels. The MEMS device is simple, cost effective, and requires very little power to run due to its electrostatic actuation. Because of the grating's size, the focusing optics before the grating may be the bottleneck of the device's simplicity, but we have demonstrated focusing optics after diffraction are not needed. Even if two detectors are implemented in the setup to increase range, this addition is still conceivably simpler, less expensive, and smaller volume than other techniques.

Chapter V

Applications of Technology for Fluorescence Measurements

With the concept of the tunable MEMS grating for spectroscopic measurements proven to work, the device can now be implemented for actual fluorescent measurements. The previous experiments implemented lasers to simulate multiwavelength measurements. A new optical system is now built to take measurements from samples loaded onto an inverted fluorescent microscope. The chapter describes the advantages of this optical system, the design of its components, newly fabricated MEMS devices, and experimental results showing fluorescent measurements.

5.1 Microscope Integration

A fluorescent microscope as seen in Figure 5.1 [96] is a standard tool for the fluorescent measurements of cells and other microscopic objects tagged with fluorescence. Many forms of fluorescent measurements incorporate this type of microscope for its imaging and light collection capabilities. Example applications include fluorescent resonance energy transfer (FRET) measurements for cell Ca^{2+} concentration studies [97, 98], hyperspectral imaging for determining cancerous cells [99, 100], quantum dot and nanoparticles studies of intercellular processes [9, 101], multispectral systems for imaging live cells [26], and many others. Most measurements are achieved through an attached CCD camera or camera system as seen in the image.

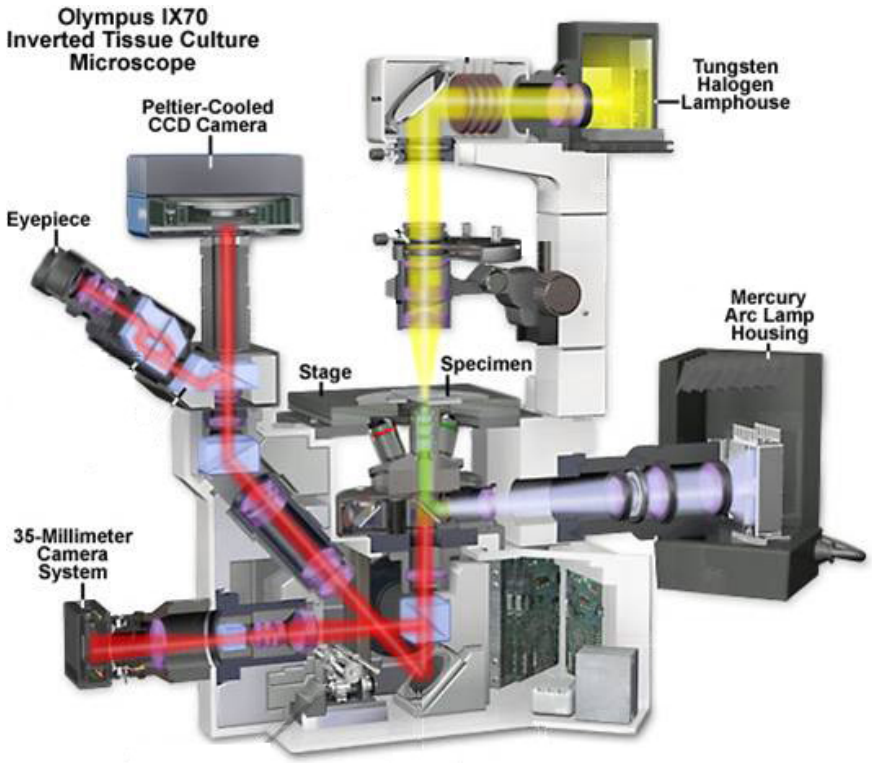

Figure 5.1: Image of a fluorescent microscope and its labeled components [96].

By integrating our MEMS spectroscopy system with a fluorescence microscope, we enable unique detection capabilities. The detection system facilitates fast spectral measurements under 1 ms with sufficient sensitivity for most fluorescence detection. These measurements are taken with a single PMT detector. Other spectroscopy systems described in Section 2.1 either utilize CCD camera systems with reduced speeds, high powered and costly CCD cameras, or multiple detectors placed in a complex optical series. Multicolor discrimination with a single high speed, highly sensitive PMT detector is now possible. This detection setup allows for the mentioned applications of fluorescence microscopes to be more readily available and allow for a higher throughput of experimentation.

The fluorescence microscope setup also provides several convenient advantages. The microscope is ideal for focusing onto small samples and collecting low intensity light. Small samples such as cells and microfluidic channels can be observed and aligned through the microscope eyepieces. Changing samples for measurement is as simple as replacing slides on the microscope stage.

Another important advantage is that the microscope provides the necessary optics to focus excitation light and collect emission light through the objective. Excitation light is a key component to fluorescence measurements. It provides the optical energy required for particles to fluoresce, and a microscope can focus this light to a confined region. This focusing ensures that fluorescent tags or particles are only excited at the correct time and location, which reduces any quenching, or reduction of the excited signal over time. Several types of excitation sources exist such as xenon arc lamps, quartz-tungsten halogen lamps, argon-ion lasers, helium-neon lasers, and LEDs [1]. Each type provides a different light source wavelength, and selecting the correct wavelength is necessary for optimal excitation. In Figure 5.1, a mercury arc lamp is illustrated as the excitation source, which is the source used for our experiments. The microscope is also ideal for maximum emission light collection. The same objective used for excitation can collect the fluorescent light and direct it to the eyepieces or a detector. Most microscopes have connection ports to attach various detectors. One of these ports makes a convenient way to output the light signal from the microscope to our spectroscopy setup.

The microscope chosen for experimentations is an inverted fluorescent microscope (Nikon Eclipse TS100, Nikon Inc.) with a Hg 100 W arc lamp (LH-M100CB-1, Nikon Inc.), similar to the microscope shown in Figure 5.1. With the addition of our spectroscopy setup as the fluorescence detection system, quality spectral measurements with a dramatic reduction in detector technology may finally be realized.

5.2 Optical System Design

The optical setup combining the fluorescent microscope with the MEMS spectrometer involves several optical components. Some components are interchangeable within the fluorescent microscope, and others are custom additions. Along the optical path, these components include an excitation source, excitation filter, dichroic mirror, fluorescent sample, microscope objective, emission filter, focusing lens, fiber optic, collimating lens, MEMS grating, detector slit, and detector. Figure 5.2 displays the layout of these components.

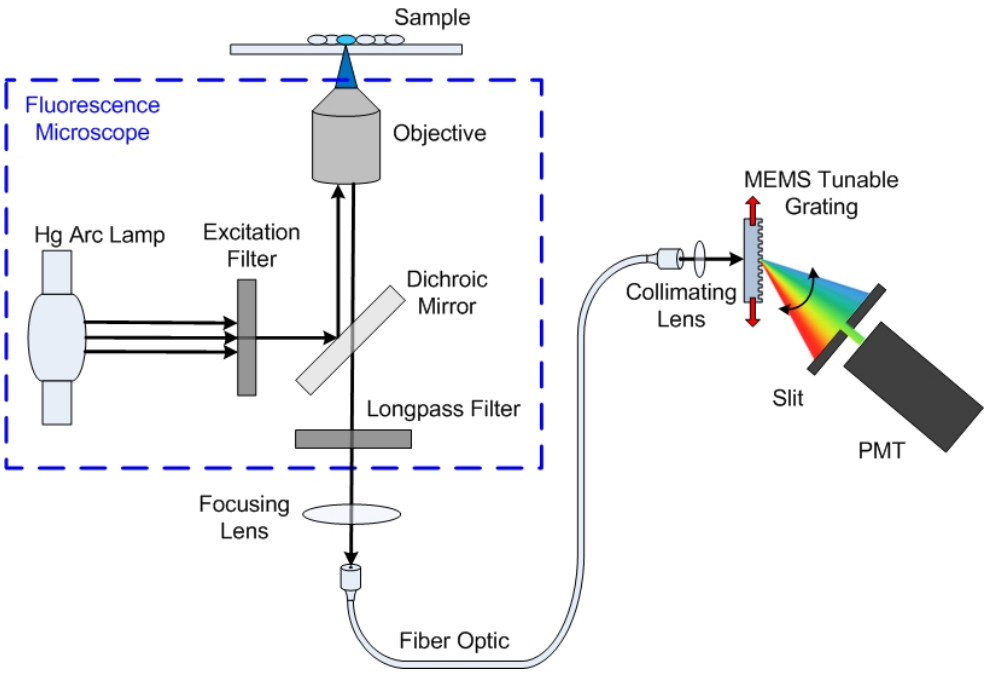

Figure 5.2: Schematic of the optical system setup integrating a fluorescent microscope with the MEMS spectroscopy system.

The system's overall ability to measure fluorescent signals depends on the detector's sensitivity and the multiple optical system efficiencies within the system. Each efficiency determines how much of the useful optical signal can be collected and how much is lost at that step. Some interfaces of the system can be optimized with calculations, some can be enhanced at the price of more expensive and complex optics, and others have a definitive trade-off that makes partial signal loss unavoidable. The optical system's overall sensitivity can be broken down into the following efficiencies and specifications:

1. Fluorescent Emission Efficiency
2. Fluorescent Collection Efficiency
3. Emission Filter Efficiency
4. Fiber Optic Focusing Efficiency
5. Fiber Transmission Efficiency
6. Collimation Efficiency
7. Grating Efficiency
8. Detector Slit Efficiency
9. Detector sensitivity

5.2.1 Fluorescent Emission Efficiency

Emission efficiency is the amount of light a fluorescent sample emits relative to its maximum possible emission. To generate maximum fluorescence, the excitation source should have a peak at the fluorophore's excitation spectrum peak. An excitation spectrum is a plot showing how effectively a range of wavelengths induce fluorescent emission. Typically, the excitation spectrum is recorded by measuring the emission maximum while the excitation light source is scanned through the absorption bands of the fluorophore [1]. The excitation light source should provide ample light at the excitation spectrum peak. The excitation filter must also correspond to the excitation peak and allow the correct range of the light source to pass. The excitation filter is responsible for blocking any excitation light that overlaps with the emission wavelength range, ensuring that any detected signal is the sample emission and not the excitation source. Figure 5.3 is an example setup showing the spectrum of enhanced cyan fluorescent protein (ECFP), a mercury arc lamp excitation source, and corresponding excitation filter [102].

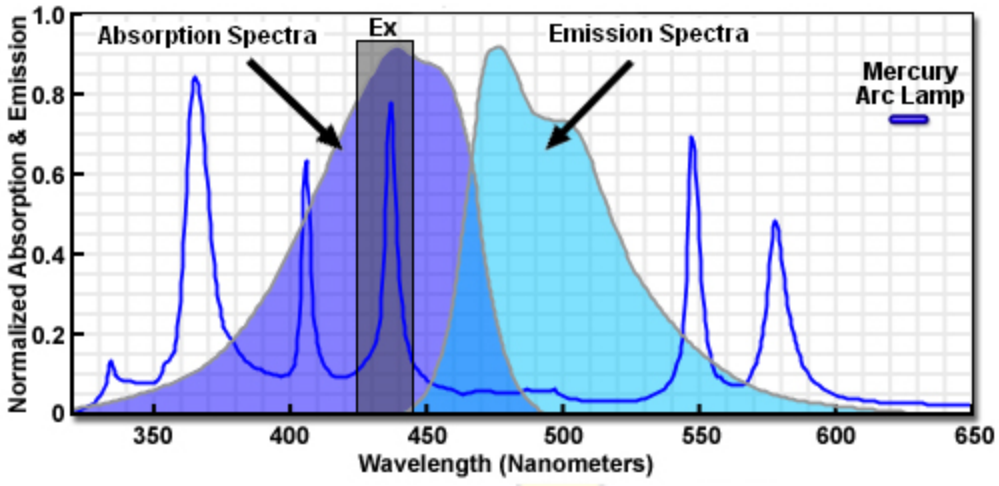

Figure 5.3: Spectral plot of mercury arc lamp excitation, absorption and emission spectra of ECFP, and transmission of an appropriate emission filter [102].

5.2.2 Fluorescent Collection Efficiency

Collection efficiency is the amount of emitted fluorescence light collected with the microscope objective. Fluorescence emission from a sample is diffuse and emits in all

directions. The objective is able to collect a cone shaped section of the diffuse light. The amount of light it collects is determined by the objective's numerical aperture (NA). An objective with a large NA is desirable in order to collect as much of the fluorescent signal as possible. The NA of an objective or other optical component is defined as the following:

$$NA_i = n_i \sin\theta_i, \tag{5.1}$$

where n is the refractive index of the media between the objective and sample, θ is one-half the angular aperture of the collected cone of light, and i is an integer referencing a certain part of the optical system. An oil immersion lens with a NA value greater than 1.25 is optimal for collecting as much fluorescence as possible from a larger cone of light. Figure 5.4 illustrates how a larger NA value is able to collect more fluorescent light from the sample. The objective to the left has the lowest NA value and collects the smallest cone of light from the sample. The objective to the right uses oil immersion to collect significantly more fluorescence. The objective used in our fluorescent measurement experiments is either an extra long focal length objective with $NA_1 = 0.6$ (Plan Fluor ELWD 40x/0.60, Nikon Inc.) or an oil immersion objective with $NA_1 = 1.4$ (Plan Apo 60xA/1.4 oil, Nikon Inc.).

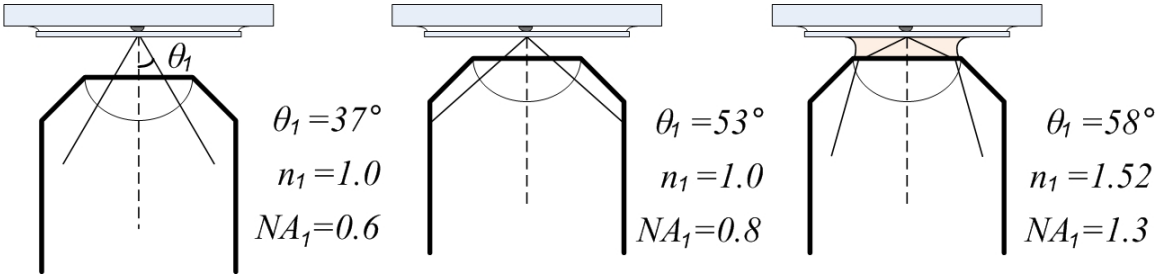

Figure 5.4: Illustration of three objectives with varying NA values demonstrating the increased amount of light collected with a higher NA.

5.2.3 Emission Filter Efficiency

The emission filter efficiency is the amount of signal able to pass through the filter relative to the incident light. The filter helps block all undesirable light in the excitation wavelength range and allows the relevant fluorescent signal to pass. It is necessary for the emission filter band-pass range to coincide with the fluorescence emission profile.

The emission filter will also determine what range of wavelengths is detectable with the MEMS spectroscopy setup.

5.2.4 Fiber Optic Focusing Efficiency

The percentage of light that can be focused into the fiber optic is the fiber optic focusing efficiency. The implementation of a fiber optic is the most practical and convenient technique to integrate the fluorescent microscope with the MEMS spectroscopy setup. Some signal losses, however, occur with the integration of the fiber optic. For these applications, the two important parameters are the fiber optic core size and NA value. A larger core size allows more light to be focused into the fiber with fewer constraints on alignment. The NA determines the angle at which light can enter and be transmitted through the fiber. Figure 5.5 illustrates the interface between the focusing objective and fiber. The angle θ_2 is the angle in which the light is focused determined by the NA of the objective. The angle θ_3 is the fiber optic's acceptance angle determined by the NA of the fiber.

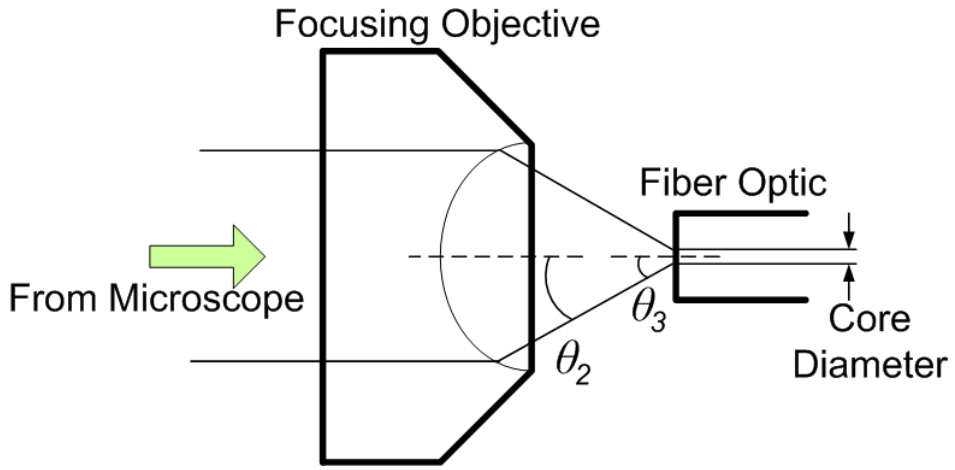

Figure 5.5: Schematic of the optical path for the interface of the fluorescent microscope to the fiber optic.

In order to focus into the fiber, another microscope objective is implemented at the output of the fluorescent microscope. For the minimal loss to occur, the objective NA must match the fiber NA. Any light that is focused at a wider angle than what the fiber can transmit is lost. An objective with a larger NA can also collect more light from the

relatively wide beam of the microscope output. Therefore, for the best fiber optic focusing efficiency, an objective with a large NA should be implemented with a fiber optic with a matching NA and large core size. The problem, however, occurs at the output of the fiber optic. The fiber core size and NA along with the collimating element determine the minimum collimated beam diameter. The smallest beam diameter is desired, and a larger core size and NA increase the minimum diameter. A fiber optic and focusing objective must be selected carefully to minimize the losses at both the input and output of the fiber. The components determined to be best suited for the setup are an objective with $NA_2 = 0.25$ (10x/0.25, Nikon Inc.) and a fiber with $NA_3 = 0.22$ and core size of 50 μm (59341, Edmund Optics).

5.2.5 Fiber Transmission Efficiency

The fiber optic also has losses from attenuation traveling through the fiber and reflections at the core-air interface at the entrance and exit. With a fiber optic of ~1 m, the losses traveling through the fiber optic are minimal. Some loss comes from the connector ends, but also relatively low. A typical patch cable fiber optic has <0.3 dB insertion loss, referring to the light loss when the fiber optic is inserted into another connector [103]. The optical power drops 6.7% if the insertion loss is the maximum 0.3 dB. The fiber optic for this application is not necessarily attached to another connector, but the insertion loss gives a reasonable estimate at the loss due to absorption, air-core interface, and misalignment.

Another important specification of the fiber optic is the wavelength range. Losses can increase significantly if the fiber optic is not suited to the wavelength range of interest. It is necessary that the proper fiber be chosen to fit the particular fluorescent measurement experiment.

5.2.6 Collimation Efficiency

The collimation efficiency refers to the percentage of light that is collimated from the fiber optic exit and incident onto the MEMS grating. This interface is illustrated in Figure 5.6. Because of the MEMS grating's small size, the collimated beam should be as small as possible. Most spectrometers with a fiber optic input use a reflective parabolic collimator to eliminate minor chromatic aberrations. However, a reflective collimator is unable to fold the optical path and generate a small enough beam diameter, so a collimating lens is utilized instead. The collimating lens must have a NA value equal or larger than the fiber optic and the working distance should be as short as possible. Moving the lens as close as possible to the fiber optic reduces the increase in diameter of the optical signal exiting from the fiber core. The fiber's NA and core diameter should be as small as possible to collimate the signal to a small beam diameter. However, a larger NA and core is desirable to increase the fiber optic focusing efficiency. The fiber's specifications must be balanced in order to accommodate both efficiencies. The collimating lens implemented is a fiberport collimator with an effective focal length of 2 mm and $NA_4 = 0.5$ (PAF-X-2-A, ThorLabs Inc.).

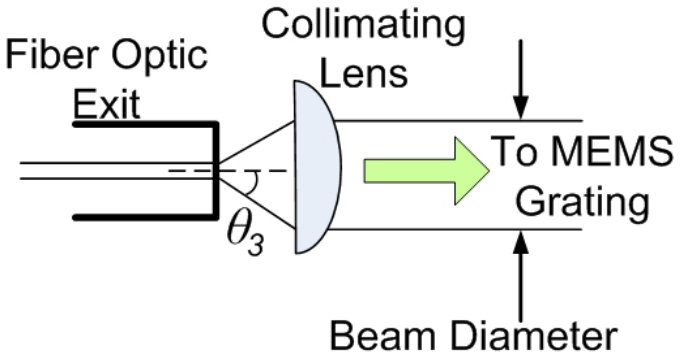

Figure 5.6: Schematic of the optical path for the interface of the fiber optic to the MEMS grating.

After the collimating lens the MEMS grating should be placed as close as possible. Due to optical dispersion, a beam can never be perfectly collimated, and it increases in diameter with distance traveled. Keeping the MEMS grating close reduces the dispersion of the optical signal. The efficiency of the collimation then comes from the amount of signal incident onto the grating compared to the entire signal. If the beam diameter is larger than the grating, the light not incident onto the grating either passes through the

MEMS device into the 0^{th} order or is reflected off the bottom surface of the silicon actuator. It is clearly desirable to design the MEMS grating to be large enough to not lose any significant amount of the optical signal.

5.2.7 Grating Efficiency

The grating efficiency determines the percentage of light that is diffracted into the 1^{st} order of diffraction. The grating efficiency is discussed previously in design of the MEMS device in Section 3.2.5. The estimated grating efficiency for the current grating is 15-20%.

5.2.8 Detector Slit Efficiency

The slit in front of the PMT allows only a small bandwidth of the optical spectrum to pass, but must also be large enough to allow enough light to be detectable. The slit width and distance from the grating to detector can be optimized to further improve the minimum detectable signal. To calculate the slit dimension, we can look to the optical setup illustrated in Figure 5.7 (illustration is dramatically not to scale in order to visualize the geometry more clearly).

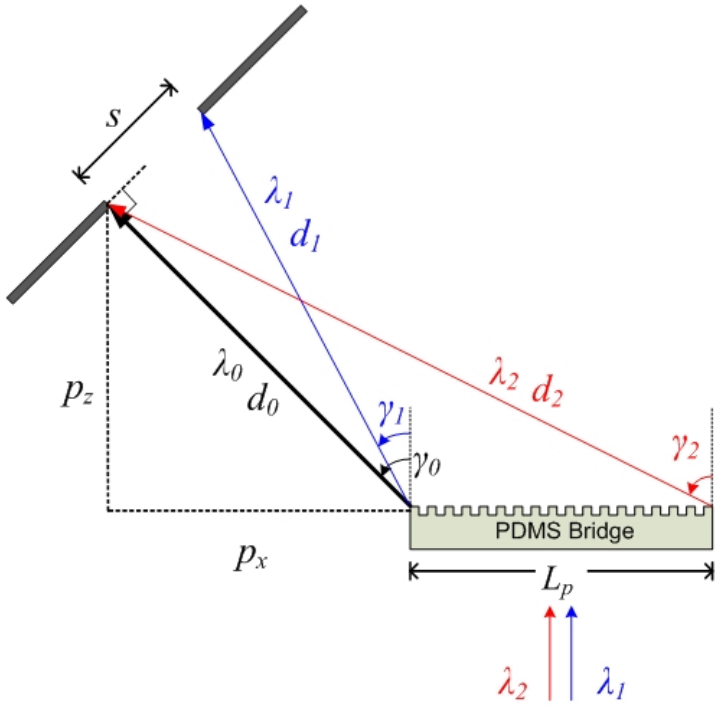

Figure 5.7: Geometry of the optical setup in order to calculate the best slit size. Illustration is not to scale.

For any slit size, s, and PDMS bridge length, L_p, a range of wavelengths can be incident onto the slit, with λ_1 being the shortest and λ_2 being the longest and travelling the paths d_1 and d_2 respectively. The slit must also be a certain distance from the grating in order to ensure Fraunhofer diffraction (far field optics) instead of Fresnel diffraction [77]. This minimal distance, d_0, is given by the Raleigh distance equation

$$d_0 = \frac{N_g{}^2 a^2}{\lambda_0} = \frac{L_p{}^2}{\lambda_0} \tag{5.2}$$

where N_g is the number of grating grooves, a is the grating period, and λ_0 is the shortest wavelength of interest. For our grating size, the distance to the slit is on the order of several centimeters. If the slit size is decreased, a smaller range of wavelengths is allowed to pass, which increases the spectral resolution. However, the resolution cannot surpass the theoretical limit of $R = N_g$ for the 1st order of diffraction. Therefore, the optimal slit size can be found from the equation

$$R = N_g = \frac{\lambda}{\Delta\lambda} = \frac{\lambda_0}{\lambda_2 - \lambda_1}. \tag{5.3}$$

Rearranging this equation and replacing N_g with L_p/a gives

$$\frac{\lambda_0 a}{L_p} = \lambda_2 - \lambda_1 . \tag{5.4}$$

The variables λ_1 and λ_2 can next be replaced with known values and the unknown slit size using trigonometry and the grating equation. The grating equations for the three different wavelengths are

$$\lambda_0 = a \sin \gamma_0 \tag{5.5}$$

$$\lambda_1 = a \sin \gamma_1 \tag{5.6}$$

$$\lambda_2 = a \sin \gamma_2 \tag{5.7}$$

where γ_0, γ_1, and γ_2 are the diffraction angles defined in Figure 5.7. From geometry we can see that

$$\gamma_1 = \gamma_0 - \arctan\left(\frac{s}{d_0}\right) \tag{5.8}$$

and

$$\gamma_2 = \arctan\left(\frac{p_x + L_p}{p_z}\right) \tag{5.9}$$

where the lengths p_x and p_z shown in Figure 5.7 are calculated as

$$p_x = d_0 \sin \gamma_0 = \frac{d_0 \lambda_0}{a} \tag{5.10}$$

and

$$p_z = d_0 \cos \gamma_0 = \frac{d_0 \sqrt{a^2 - {\lambda_0}^2}}{a} . \tag{5.11}$$

By substituting Equation 5.6 and 5.6 into Equation 5.4, we get

$$\frac{\lambda_0 a}{L_p} = a \sin \gamma_2 - a \sin \gamma_1 . \tag{5.12}$$

Inputting Equation 5.8 and 5.9 into this equation gives

$$\frac{\lambda_0}{L_p} = \sin\left[\arctan\left(\frac{p_x + L_p}{p_z}\right)\right] - \sin\left[\arcsin\left(\frac{\lambda_0}{a}\right) - \arctan\left(\frac{s}{d_0}\right)\right]. \tag{5.13}$$

Using some trigonomic rules and rearranging the terms gives

$$\frac{\lambda_0}{L_p} = \frac{p_x + L_p}{\sqrt{{p_z}^2 + \left(p_x + L_p\right)^2}} + \frac{s\sqrt{a^2 - {\lambda_0}^2} - \lambda_0 d_0}{a\sqrt{{d_0}^2 + s^2}}. \tag{5.14}$$

This equation can now be solved for the optimal slit size *s* using the known values L_p, *a*, and λ_0. For the values $L_p = 200\,\mu\text{m}$, $a = 700$ nm, and $\lambda_0 = 550$ nm, the slit size is ~200 μm and placed a distance of 7.27 cm from the grating. If the smallest wavelength of interest is 500 nm, then the optimal slit would be 146 μm placed a distance of 8 cm. This calculation ensures the maximum signal allowed through the slit without affecting the spectral resolution.

For the optical spectrometer setup, an adjustable width slit (M-SV-0.5, Newport) is implemented before the detector. The slit can be set to any size between 0 and 2 mm with a resolution of 1 μm. Equation 5.14 is used to calculate the optimal slit size for each individual experiment. The slit can then be opened further if greater sensitivity is needed at the cost of a decrease in spectral resolution.

5.2.9 Detector Sensitivity

The final specification of the optical setup is the detector sensitivity. The optical detector is the transducer that converts the optical signal to a measureable voltage or current. It is an integral part in determining the setup's sensitivity and also the spectral resolution. The detector's speed must be fast enough to measure rise and falls of possible peaks within each spectral sweep. The maximum bandwidth at least 10 times as fast as the MEMS actuation is typically sufficient.

For these applications a PMT is the optimal detector. A PMT's photodetection physics allow for extremely high sensitivity as well as very high speeds. A PMT also has a wavelength dependent sensitivity and the correct detector must be selected for the wavelength range of interest. Figure 5.8 shows the detector sensitivity and signal gain for the Hamamatsu PMT selected for the spectrometer setup [104]. As seen on the graph of Figure 5.8(a) (-20 Type) the sensitivity is relatively constant for the wavelength range of 500-700 nm. For the wavelength of 600 nm and the PMT gain at maximum, the detector sensitivity is 0.14 V/pW. The detector frequency bandwidth is 20 kHz. Other PMT

models offer different tradeoffs between sensitivity and speed that can be utilized to fit the fluorescent measurement's speed and resolution requirements.

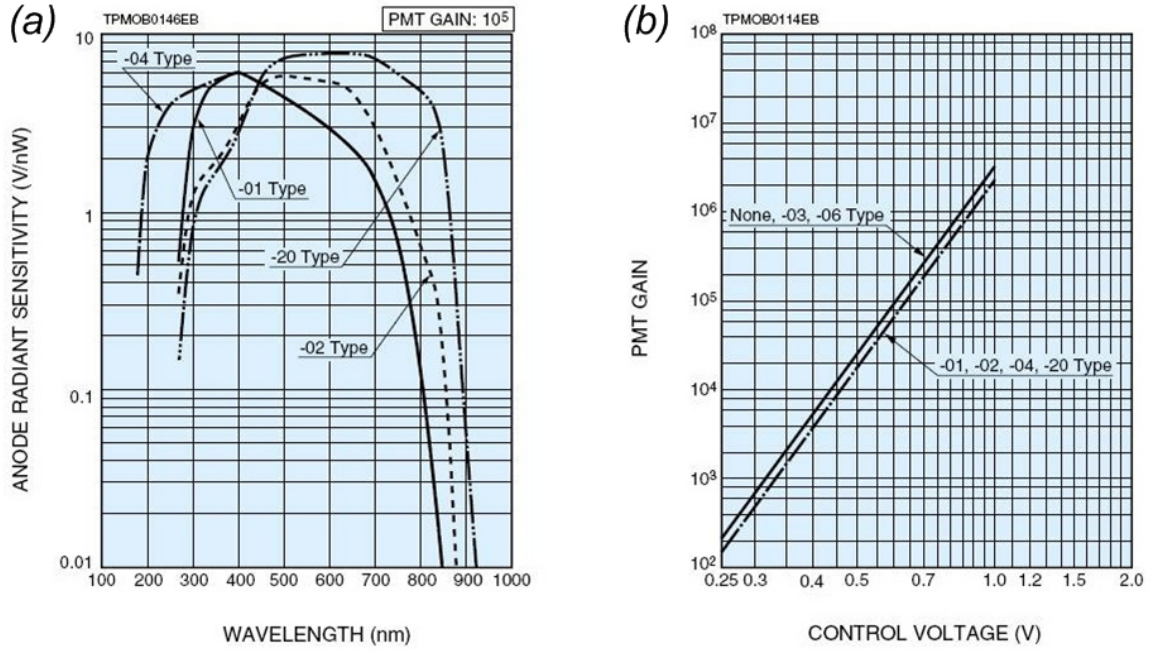

Figure 5.8: Plots of the PMT specifications [104]. (a) Sensitivity of the PMT for a range of wavelengths. The PMT used in the setup is a -20 Type. (b) The built-in gain of the PMT with respect to the control voltage.

5.2.10 Overall Efficiency Summary

With the MEMS spectroscopy setup integrated with a fluorescent microscope, spectral measurements are possible at high speeds and high sensitivity. The system's sensitivity, or overall ability to detect faint fluorescence, depends on all the factors described above. To further improve the sensitivity of the spectral measurements, some changes can be made to the factors that have the most dramatic impact on the system. Factors of the most importance include selecting the correct excitation source and filters for the fluorescence sample of interest. The excitation filter, dichroic mirror, and emission filter are typically all packaged into one interchangeable component called a filter cube. A filter of almost any wavelength range in the visible spectrum can be purchased commercially in order to fit the experiment of choice.

Another component that can drastically improve the sensitivity is the MEMS device. Changes to the MEMS device can have a significant effect on the sensitivity, as well as

spectral range, resolution, and speed. To increase the sensitivity, the grating bridge should be as large as possible in order to diffract as much of the collimated beam as possible. Increasing the bridge size, however, has impacts on the strain range and MEMS maximum speed. A system is needed in order to custom build a MEMS tunable grating specifically for different applications. Fortunately, due to the inherent nature of MEMS fabrication, multiple devices with different designs can be simultaneously fabricated on one chip. The optimal design can then be chosen to fit the correct experiment criteria, and all that is needed is a simple change in alignment onto the appropriate grating. The following section describes the design of this new type of customizable MEMS device.

5.3 Customizable MEMS Design

When integrated into the fluorescent microscope setup, the MEMS device plays a critical role in the system's overall sensitivity, spectral range, measurement speed, and spectral resolution. Because many of the spectral measurement applications have significantly varying requirements, an array of different MEMS devices can be designed in order to properly fit the particular experiment's specifications. A new device design is created in order to allow for a varying range of specifications.

The device design described previously proved the use of the tunable MEMS grating for spectroscopy and helped characterize the effects of high strain and strain rate on PDMS. The design's straight silicon beams are rigid and ideal for the fabrication process, but the spring constant is not linear with deflection and limits the maximum displacement. Furthermore, the PDMS grating is 200 um long and 100 um wide, which may not be ideal if very high sensitivity is an application requirement. Collimating a broad range of wavelengths to a small beam size with minimal loss is difficult due to optical dispersion. With a beam diameter larger than the bridge, the grating only diffracts a fraction of the collimated beam and the rest either passes through the device or is reflected off the bottom surface. A larger grating would diffract more light and hence increase the overall sensitivity of spectroscopy measurements. The spectral resolution will also increase due to an increase in number of grating lines diffracting the signal. The

downside is a larger grating also requires more force to strain and less strain range for the same amount of displacement.

The customizable MEMS design is specifically built for these microscope integration criteria. The silicon springs are a tilted folded-beam suspension, ideal for long displacements. The larger movement of the suspended silicon allows either the PDMS bridge to be initially larger for increased sensitivity, or kept small for increased spectral range. Larger displacements also require more consideration on the snap-in failure of the comb-drive, and the device must be designed for stable actuation. Figure 5.9 displays the layout of the new MEMS design in the initial and actuated positions. The design of the MEMS devices involves setting the dimensions of the PDMS bridge, silicon suspension, and comb-drive fingers. Calculations are made for the maximum silicon displacement, PDMS strain, speed of the device, and electrostatic stability.

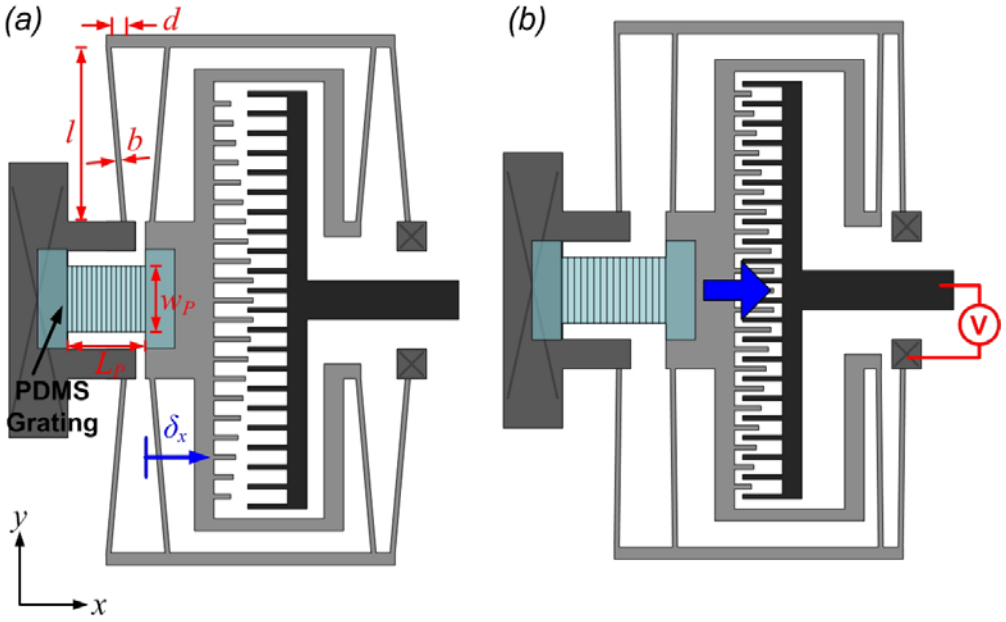

Figure 5.9: Illustration of the redesigned MEMS device with labeled dimensions. (a) The device in its initial position. (b) The device in its actuated position.

5.3.1 Design Calculations

The MEMS design starts with the strain of the PDMS bridge. Similar to the previous device, the strain directly relates to the change in grating period. The strain of the bridge is calculated as

$$\varepsilon_P = \frac{\delta_x}{L_P}, \tag{5.15}$$

where ε_P is the strain of the PDMS bridge, δ_x is the displacement in the *x*-direction, and L_P is the initial length of the PDMS bridge in the *x*-direction. The coordinates of the design are given in Figure 5.9. The *x*-direction is the direction of desired actuator displacement, and the *y*-direction is perpendicular to comb-drive fingers. The dimension L_P is one of the design parameters, and the displacement δ_x is calculated by

$$\delta_x = \frac{F_{ex}}{k_x}, \tag{5.16}$$

where F_{ex} is the force generated in the *x*-direction by electrostatic actuation, and k_x is the spring constant in the *x*-direction. The spring constant of the device is a combination of the silicon beams and PDMS bridge both resisting displacement. The springs act in parallel, and k_x is the summation of the individual spring constants calculated as

$$k_x = k_{Sx} + k_{Px}, \tag{5.17}$$

where k_{Sx} is the spring constant in *x*-direction for the silicon suspension, and k_{Px} is the spring constant in the *x*-direction for the PDMS bridge. Determining the individual spring constants using structural mechanics and replacing the values in Equation 5.17 yields

$$k_x = \frac{2E_S t b^3}{l^3} + \frac{E_P w_P t_P}{L_P}, \tag{5.18}$$

where E_S is the Young's Modulus of silicon, t is the height of the silicon structure, b is the width of the silicon beams, l is the length of the silicon beams, E_P is the modulus of PDMS, and w_P, t_P, and L_P are the width, thickness, and length of the PDMS bridge, respectively. For the silicon springs, the spring constant for the folded beam is independent of δ_x up to 10% of *l*, which typically covers the entire displacement range [83]. The PDMS strain profile is not perfectly linear as seen in Section 4.2, but Equation 5.18 is still a good approximation of PDMS's high elastic strain range and sufficiently accurate for design purposes.

The actuation force of the comb-drive actuator, F_{ex}, has been derived in other literature and is given by [85]

$$F_{ex} = \frac{\varepsilon_0 tn(\delta_x)}{g} V^2, \tag{5.19}$$

where ε_0 is the permittivity of air (8.854e-12 F/m), $n(\delta_x)$ is the number comb-drive teeth engaged as a function of δ_x, g is the gap between comb-drive teeth, and V is the actuation voltage. For this new comb-drive design, the number of engaged teeth is designed to not be constant. The variable $n(\delta_x)$ increases with displacement, δ_x. When stretching the PDMS bridge, the force required increases with displacement. The comb-drive is designed to increase the generated electrostatic force with displacement to coincide with the force required. Having teeth only engaging when needed helps reduce overall teeth overlap area which improves stability.

A closer look at the engagement profile of the comb-drive teeth is illustrated in Figure 5.10, where the left structure is suspended, and the right structure is fixed. As labeled in the figure, N is the total number of teeth on the moving structure, N_1 is the number of teeth made at maximum length, N_2 is the number of teeth initially engaged, N_3 is the number of teeth not initially engaged, L_o is the initial engagement overlap, and P is the distance between the shortest teeth and engagement.

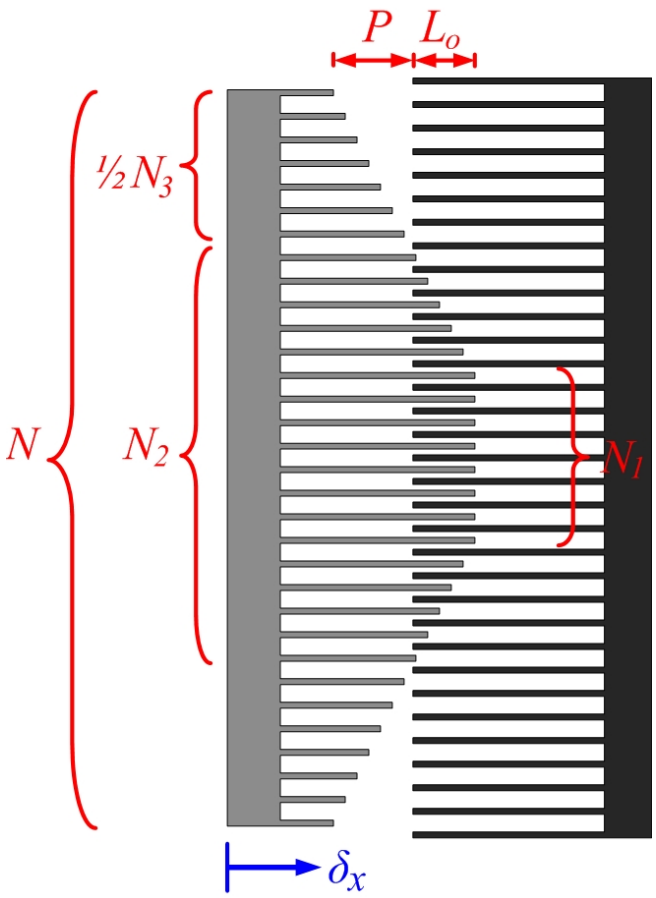

Figure 5.10: Illustration of the comb-drive teeth engagement profile.

In designing the comb-drive actuator, these variables are selected to create the appropriate force profile. Typical design iteration first sets N to obtain enough maximum force. The distance P is set to be just less than maximum displacement. The overlap L_o should be as small as possible and depends on the fabrication tolerance. The number N_1 affects the nonlinearity of the force as a function of V^2. If N_1 is equal to N, then all teeth are the same length, the number of engaged teeth remains constant, and force is linear with V^2. A N_1 value of one, or having all the teeth reduced linearly, will yield max displacement before instability, but almost all movement will come at the end of the voltage ramp [82]. For the tunable grating application, it is desirable to have the movement more gradual over a voltage ramp. A more gradual tuning cycle reduces the required speed of the photo sensor and can reduce any effects on spectral resolution. For

these applications, a suitable N_1 value is 20-50% of N. With the teeth after N_1 reduced linearly, N_2 and N_3 can be estimated from geometry and are given by

$$N_2 = \frac{N + \frac{P}{L_o} N_1}{1 + \frac{P}{L_o}} \tag{5.20}$$

and

$$N_3 = N - N_2 . \tag{5.21}$$

The number of fingers engaged as the comb-drive moves can now be given by

$$n(\delta_x) = \begin{cases} N_2 + \frac{N_3}{P}\delta_x & for \quad \delta_x < P \\ N & for \quad \delta_x \geq P \end{cases} . \tag{5.22}$$

These equations along with various design parameters can be used to calculate the displacement for a given voltage ramp.

5.3.2 Instability

Because of the compliance of the folded silicon springs, high displacements are possible. However, with the large movements, the comb-drive displacement is limited by electrostatic instability. Capacitance between overlapping fingers creates attractive forces in the undesirable *y*-direction. These forces pull at both sides of each finger and cancel each other out, but small vibrations or minor differences in symmetry can cause the force on one side to be larger than the other side. The electrostatic forces then want to pull the fingers of the suspended and fixed structure together, and the silicon springs must resist. When electrostatic force becomes larger than spring resistance force, the stability failure known as snap-in occurs.

The force that causes snap-in is calculated by the change in energy with small *y*-displacements. According to Legtenberg et al. [83], the electrostatic force in the *y*-direction is given by

$$F_{ey} = -\frac{\partial}{\partial \delta_y}\left(\tfrac{1}{2} C V^2\right), \tag{5.23}$$

where δ_y is the displacement in the *y*-direction and *C* is the capacitance difference between comb-drive fingers. The capacitance is estimated as

$$C = \frac{\varepsilon_o A}{g - \delta_y} + \frac{\varepsilon_o A}{g + \delta_y}, \tag{5.24}$$

where *A* is the total comb-drive finger overlap area. The overlap area can be broken down into two components given by

$$A = tq(\delta_x), \tag{5.25}$$

where $q(\delta_x)$ is the total comb-drive finger overlap length that varies as a function of δ_x. Using the comb-drive engagement profile seen in Figure 5.10, the total length of the engaged fingers as a function of δ_x is calculated through geometry and given by

$$q(\delta_x) = \begin{cases} \frac{1}{2}\frac{N_3}{P}\delta_x{}^2 + N_2\delta_x + \frac{1}{2}L_o\left(N_1 + N_2\right) & for \quad \delta_x < P \\ N\left(\delta_x - P\right) + \frac{1}{2}N_3 P + N_2 P + \frac{1}{2}L_o\left(N_1 + N_2\right) & for \quad \delta_x \geq P \end{cases}. \tag{5.26}$$

These equations show that the electrostatic force in the *y*-direction, F_{ey}, grows with *x*- and *y*-displacement, δ_x and δ_y. To calculate the device instability, this force is modeled as a negative spring in the *y*-direction. According to Zhou et al. [85], the electrostatic spring constant in the *y*-direction is calculated by

$$k_{ey} = \left.\frac{\partial F_{ey}}{\partial \delta_y}\right|_{\delta_y = 0} = \frac{2\varepsilon_o tq(\delta_x)}{g^3} V^2. \tag{5.27}$$

The folded silicon springs resist this force and are also modeled as a spring constant in the *y*-direction. Derived in [85], the tilted folded-beam suspension has a spring constant dependent on δ_x and given by

$$k_{Sy} = \frac{1}{\frac{1}{k'_{Sy}} + \frac{1}{k''_{Sy}}}, \tag{5.28}$$

where

$$k'_{Sy} = \frac{2E_S tb}{l} \tag{5.29}$$

and

$$k''_{Sy} = \frac{50E_S tb^3}{(3\delta_x - 5d)^2 l}. \tag{5.30}$$

The value k'_{Sy} represents the Hooke's Law term, while the value k''_{Sy} represents the displacement dependent term for calculating k_{Sy} in Equation 5.28. The value *d* is the initial projection of silicon beams in the *x*-direction giving the beams a tilted shape, as seen in Figure 5.9.

For the comb-drive to be stable, the resistive springs must be larger than the attractive negative springs, or k_{Sy} must be greater than k_{ey}. An instability term can be defined as the ratio of the spring constants and given by

$$J = \frac{k_{ey}}{k_{Sy}}. \tag{5.31}$$

When *J* is greater than 1, comb-drive snap-in is imminent. Research has shown that actuators in practice have a likely chance for snap-in around $J = 0.65$ due to minor external disturbances, and $J = 0.2$ is a good design parameter [82]. For our designs, comb-drives are designed so that the silicon spring constant is at least five times the electrostatic spring constant at the max displacement, shown by $k_{Sy} \geq 5k_{ey}$ or $J \leq 0.2$.

5.3.3 Device Speed

Maximum speed of the MEMS device is determined by resonant frequency in the *x*-direction [83]. The resonant frequency is calculated by

$$f_0 = \frac{1}{2\pi}\sqrt{\frac{k_x}{m_{shuttle} + \frac{1}{2}m_{truss} + \frac{96}{35}m_{beam}}}, \tag{5.32}$$

where $m_{shuttle}$ is the mass of comb-drive moving structure, m_{truss} is the mass of one truss connecting the silicon springs, and m_{beam} is the mass of one silicon beam of the suspension. The mass of the shuttle is given by

$$m_{shuttle} = tA_{shuttle}\rho_S , \tag{5.33}$$

where $A_{shuttle}$ is the top area of comb-drive shuttle determined by mask layout, and ρ_S is the density of the single crystal silicon (~2330 kg/m^3). The mass of the truss and beam are calculated in the same manner.

5.3.4 Design Results

Equations 5.15 through 5.33 are used to design a tunable grating device and calculate the device's maximum stable displacement, strain profile of the PDMS bridge, and maximum speed. An example of a new comb-drive design made to be implemented with the microscope setup is given in Table 5.1. The PDMS bridge is 300 μm long and 300 μm wide, a significant increase from older designs. Figure 5.11(a) shows a graph of the comb-drive's instability as displacement of the actuator increases. The dotted line marks the design limit of $J = 0.2$ and the displacement at which this value occurs. Figure 5.11(b) shows the amount of strain created in the PDMS bridge as the actuation voltage increases. The dotted line again marks an instability value of 0.2. The maximum strain of the PDMS bridge is calculated to be just above 20% for a 200 V actuation.

Table 5.1: Dimensions and design values for one of the comb-drive designs.

PDMS Bridge	**Silicon Suspension**	**Comb-drive Teeth**
$L_P = 300$ μm	$b = 6$ μm	$N = 504$
$w_P = 300$ μm	$l = 800$ μm	$N_1 = 0.4N$
$t_P = 20$ μm	$t = 50$ μm	$L_o = 10$ μm
	$d = 27$ μm	$P = 50$ μm
		$g = 5$ μm

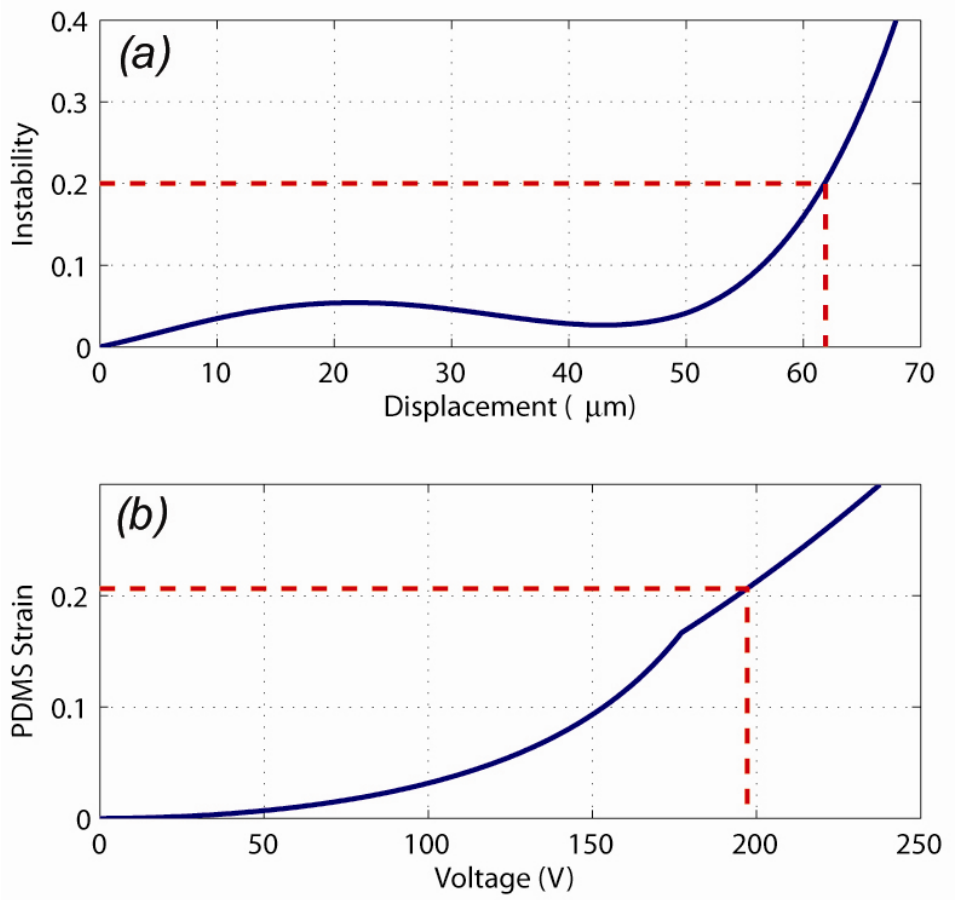

Figure 5.11: Graphs of the instability and PDMS strain with device actuation. (a) Instability of the comb-drive for silicon actuator displacement. Dotted line marks the design limit of 0.2 for instability. (b) PDMS strain for the actuation voltage. Dotted line again marks an instability value of 0.2.

The maximum speed of this device is also calculated. From Equation 5.32, the frequency value calculated is $f_0 = 1.748$ kHz. This device is an example of improved maximum strain of an increased PDMS bridge while keeping sufficient maximum speed. Other devices are also designed with variations in the device dimensions to accommodate for different experiment specifications.

5.3.5 Fabrication

The fabrication of the device is the same process as described in Section 4.1, with the exception of a few modified steps. A metal layer is sputtered and patterned onto the SOI wafer before silicon etching to create contact pads for wire bonding. The backside of the

SOI wafer is also etched before the assembly of the PDMS and actuators. This switch in the order of steps helps preserve the optical quality of the PDMS, since it is no longer bonded during silicon etching steps. As shown in the previous Figure 4.2, the alignment and bonding of the PDMS microstructures to silicon actuators requires a drop of deionized water between the structures. The water creates surface tension that aids in aligning the structures and also delays the PDMS-Si permanent bonding, allowing contact of the structures without sticking. However, with suspended structures the water surface tension also pulls the comb teeth together. This type of stiction moves the suspended silicon structures in the *x*-direction and prevents PDMS alignment. Previous comb-drive designs had single beam suspension, and their stiffer suspension made this stiction unlikely. With the more compliant suspension of folded silicon beams, the pull-in stiction is unavoidable. An additional fabrication step is added to constrain the suspended structures and prevent the snap-in stiction when water is added.

The new fabrication assembly is shown in Figure 5.12. The SOI suspended comb-drive is fabricated as before and shown in Figure 5.12(a). The die is then flipped and placed on a PDMS slab (Dow Corning Corporation, 10:1 base-curing agent ratio) shown in Figure 5.12(b). The PDMS and silicon form a reversible bond that immobilizes the suspended silicon [89]. The etched out backside of the die is filled with photoresist (AZ 9260, MicroChemicals) and hard baked to form a solid structure, as seen in Figure 5.12(c). The die is flipped over again and the PDMS slab is peeled off the silicon die leaving the suspended silicon held in place by the photoresist from the backside, shown in Figure 5.12(d). Oxygen plasma is used for surface activation of the silicon and top mold PDMS microstructures, and water is implemented for alignment and bonding, shown in Figure 5.12(e) and 5.12(f). The top mold is then released by dissolving the photoresist, and the suspended silicon restraint is dissolved in the same process. The final fabricated device is shown in Figure 5.12(g). These new steps along with the rest of the fabrication recipe are given in full detail in Appendix A.

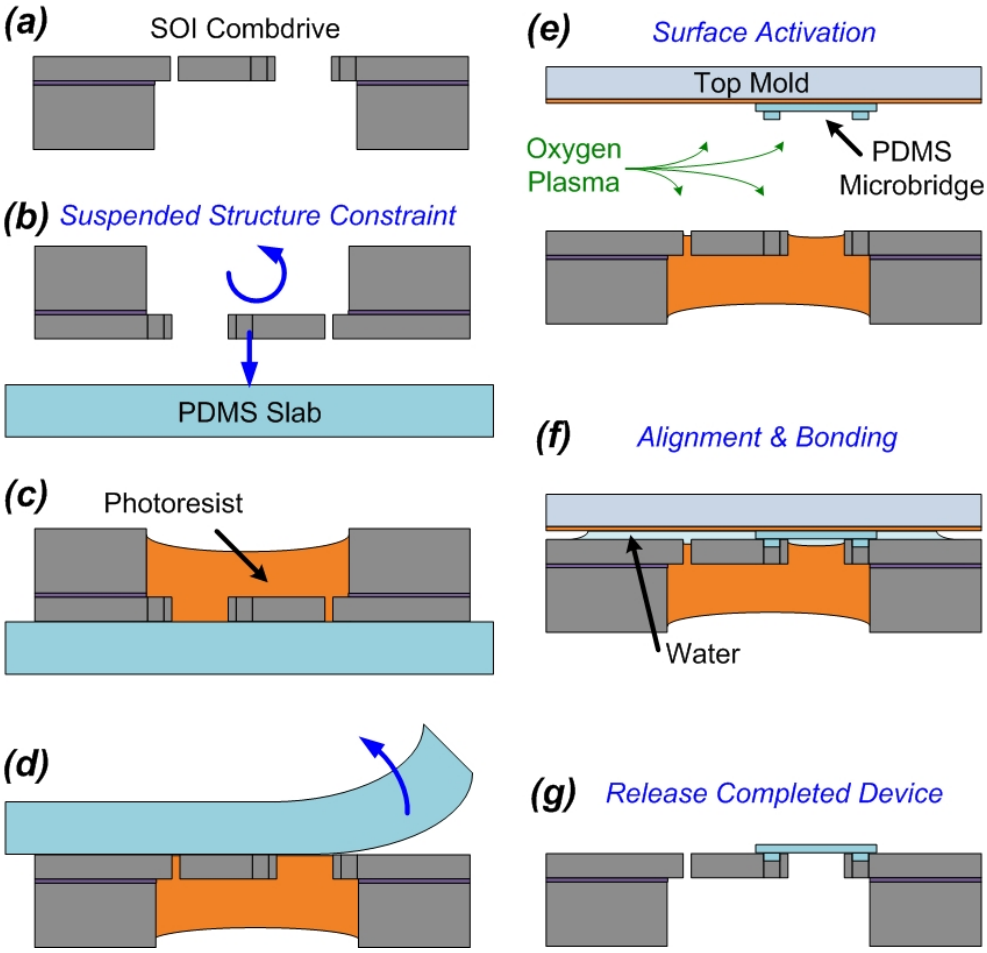

Figure 5.12: New fabrication steps for the assembly of the devices. (a) The suspended silicon actuators made from an SOI wafer. (b) Constraining the suspended structure by flipping the die and placing it on PDMS to form a reversible bond. (c) Photoresist is added to the backside etch through holes and hard baked to hold the suspended structures. (d) The PDMS slab is peeled from the front side of the device. (e) The SOI die and top mold die are treated with oxygen plasma. (f) The PDMS microstructures and silicon actuators are aligned and bonded using water surface tension assistance. (g) The photoresist of the top mold and backside constraint are dissolved with solvent leaving the completed device.

A completed device is shown in the SEM image of Figure 5.13. The inset image shows a closer look at the surface grating pattern. The PDMS bridge of this device is 200 μm long and 100 μm wide. The bridge has the dimensions of the original design, and this particular device is built for maximum strain.

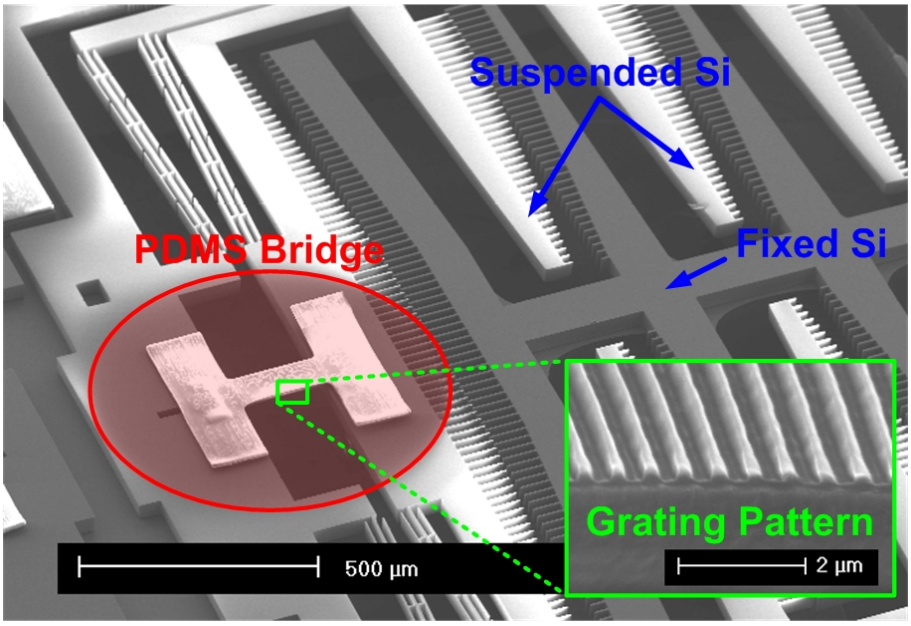

Figure 5.13: SEM image of a completed device. Inset image is of the grating pattern on the top surface of the PDMS bridge.

Optical images of a device during actuation are taken. The strain is calculated by measuring the change in length from the images. The images seen in Figure 5.14 show an increase in length of 30%. The image in Figure 5.14(a) is the device's initial position, and the image in Figure 5.14(b) is the displaced position with a voltage actuation of 200 V. It is clear that the new customizable MEMS design allows for a large strain range for certain device designs.

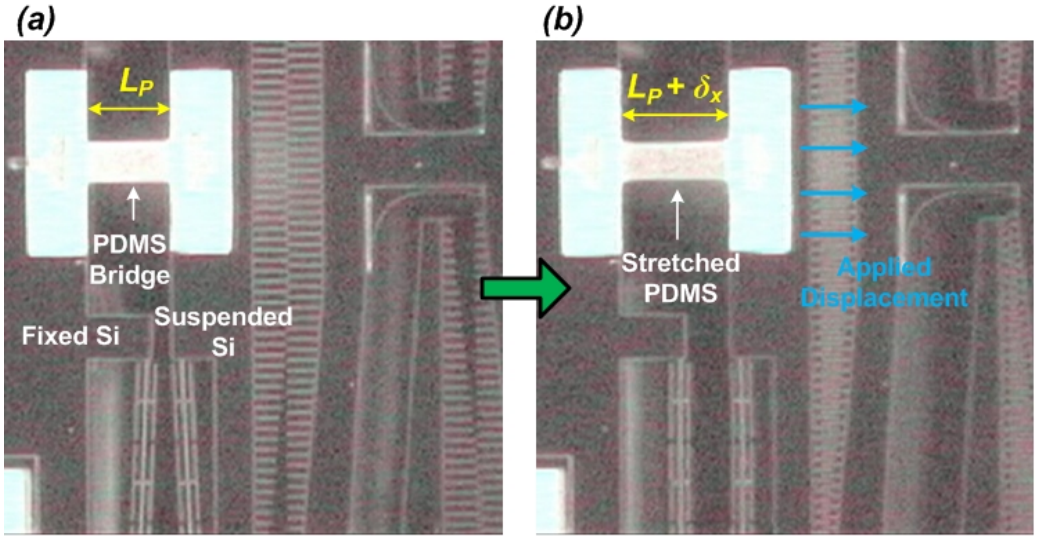

Figure 5.14: Optical images taken of a device. (a) The device at its initial position. (b) The device in its actuated position with the PDMS bridge stretched 30%.

5.3.6 Carrier Wafer Mounting

The final step in prepping the MEMS device for integration with the fluorescent microscope is mounting the device to a carrier wafer. A custom designed printed circuit board is made, and a center hole is cut in order to allow the optical signal to enter from the backside, as seen in Figure 5.15(a). The 2 by 2 cm die is mounted onto the carrier board with special double stick tape and wire bonded to the leads. Wires are soldered onto the carrier board to allow easy voltage actuation of several different devices. The completed device mounted to the carrier wafer is shown in Figure 5.15(b). The MEMS device is now ready for implementation with the optical setup.

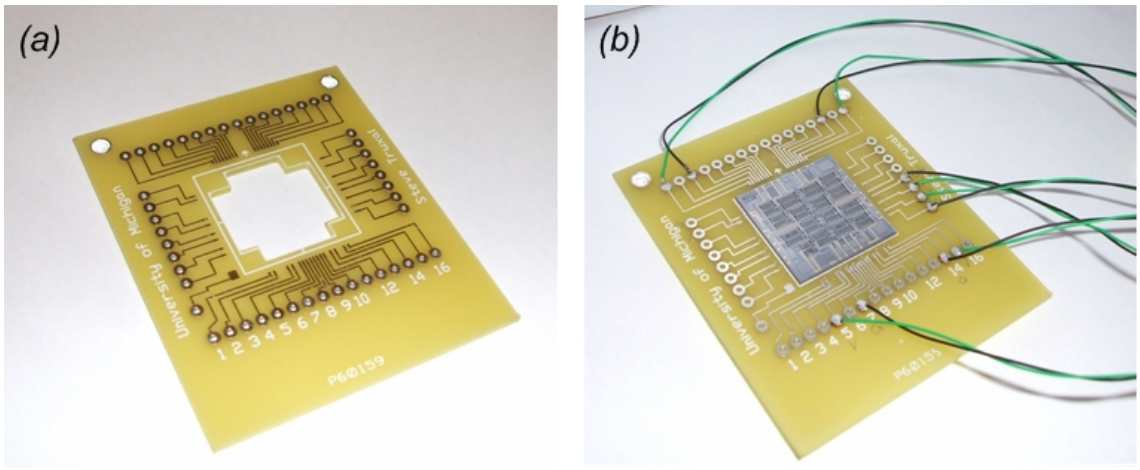

Figure 5.15: Images of the device mounted to a carrier wafer. (a) A printed circuit board with a center cut hole. (b) A die mounted and wire bonded to the carrier board.

5.4 Dynamic Fluorescence Measurements

5.4.1 Characterization Measurement

With the MEMS device completed, the tunable grating can now be implemented with the fluorescent microscope setup. The fiber optic output is aligned to the PDMS bridge as described in Section 5.2. Before integrating the PMT sensor and slit for spectral measurements, a PSD sensor is used to calibrate the change in grating period for voltage actuation, similar to measurements taken in Section 4.2.2. A 200 Hz sine wave is applied

to the MEMS device for voltage actuation. A green laser of 533 nm is directed through a 50 μm pinhole placed on the microscope stage, and the monochromatic light is fed through the optical system. As the MEMS device actuates, the change in diffraction angle is measured with the PSD. The change in grating period is then calculated using the grating equation, given in Equation 3.2. Figure 5.16 shows the results of the data. Figure 5.16(a) is one cycle of the voltage actuation, and Figure 5.16(b) is the corresponding change in grating period.

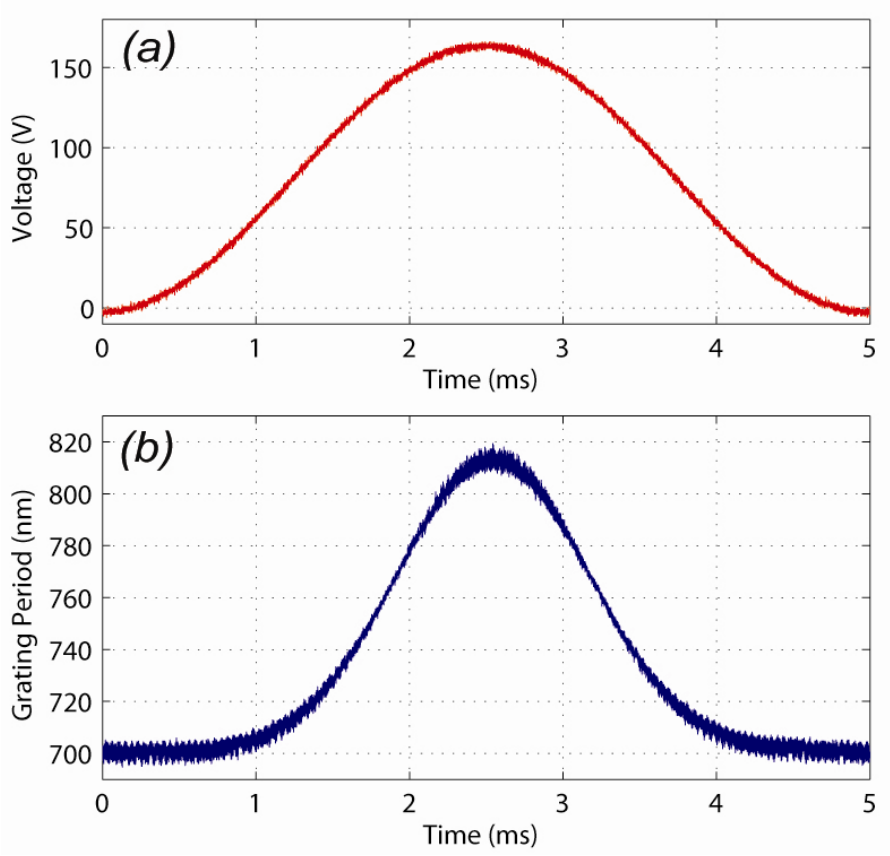

Figure 5.16: Characterization measurement of a MEMS device. (a) Once cycle of the MEMS voltage actuation. (b) The corresponding change in period of the PDMS grating.

After the measurement, the PSD is replaced with the PMT and slit. With the characterization data and the placement angle of the PMT, the wavelength incident onto the detector is calculated as a function of the voltage cycle. The setup is now ready for spectral measurements.

5.4.2 Microfluidic Cytometry Implementation

To demonstrate the setup's capabilities, the system is implemented with a microfluidic cytometer. Flow cytometry is a valuable tool and has become the standard in many medical research fields, most notably in cell biology. Cells or other forms for fluorescent tags are run single file through a fluidic channel and measurements of the fluorescence are taken of each individual sample. As the field of flow cytometry is continuously growing with new applications, more efforts are being directed towards simultaneous measurements of multiple fluorescent colors [7]. Another field of research in cytometry is dedicated to using microfluidics for the fluidic focusing of the sample [31]. Previous work within our research group has also implemented a microfluidic platform for proof of concept flow cytometry measurements [105]. This microfluidics chip is an ideal device for the demonstration of the measurement capabilities. A fluorescent sample can be fluidically focused to pass through the microscope interrogation zone at programmable speeds.

The microfluidic cytometer implemented is illustrated in Figure 5.17. The channel design is described in previous research by our group [105]. The channel is fabricated from PDMS using soft lithography replication of patterned photoresist. The PDMS is then bonded to a 200 μm thick glass slide to form the bottom wall of the channel. A full description of the fabrication steps is given in Appendix B. To demonstrate the spectroscopy's multiwavelength detection capabilities, two types of fluorescent beads are loaded into the sample syringe pump. Green fluorescent beads (35-8, Duke Scientific Corp.) 35-50 μm in diameter are mixed with red fluorescent beads (36-6, Duke Scientific Corp.) 20-30 μm in diameter. According to the specifications, the green and red beads have fluorescent peaks at 530 nm and 610 nm, respectively.

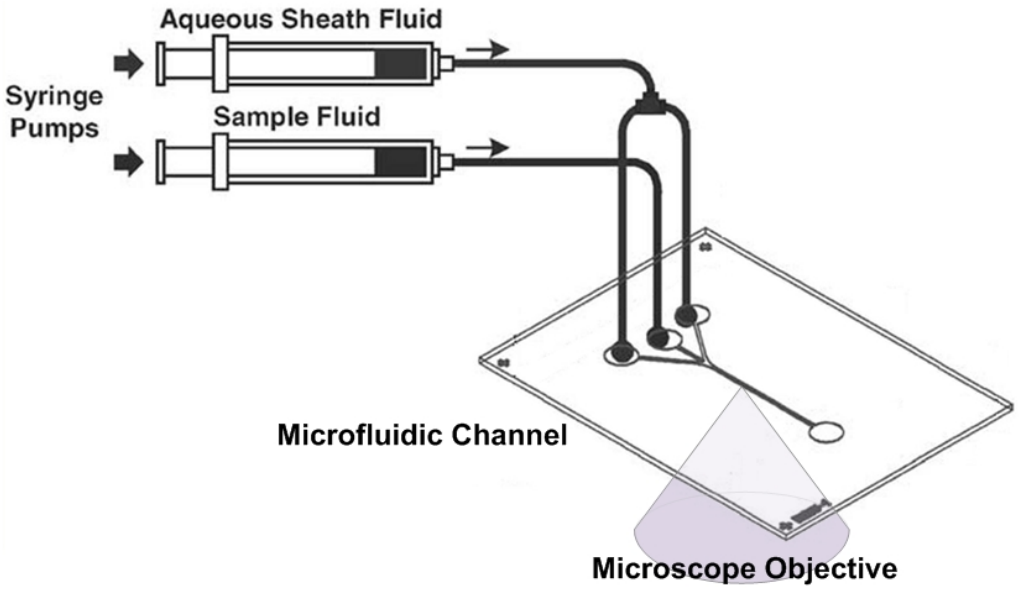

Figure 5.17: Illustration of the microfluidic device placed on the microscope stage for spectral cytometry measurements.

For this experiment a filter cube (B-3A, Nikon) is placed into the microscope with an excitation filter of 420-490 nm, dichroic mirror of 505 nm, and a long pass emission filter of 520 nm. The mercury arc lamp is used for excitation, and the filter cube allows an excitation peak at 438 nm. This peak is not optimal for either type of bead but still works for fluorescent excitation. The result is the green beads are not as bright as their maximum fluorescence, and the red beads even farther from their optimal excitation are significantly less intense than the green beads.

The microfluidic channel is placed onto the microscope stage and run at a constant flow rate of 10 μL/min. The arc lamp excites the passing fluorescent beads and the fluorescence is collected through the same objective. The light signal is then passed through a fiber optic and focused onto our MEMS grating, and the diffracted signal is detected by the PMT as seen in Figure 5.18(a). The MEMS device is simultaneously being actuated with a voltage sine wave at a frequency of 200 Hz. The MEMS voltage actuation signal and prior MEMS characterization are used to determine the continuously changing wavelength passing through the slit and incident onto the PMT. As the beads pass the detection zone, multiple spectral sweeps are taken. The beads pass through the 200 μm detection zone in approximately 0.1 s. Measurements in Figure 5.18(b) and 5.18(c) show the spectral sweeps taken of a red bead and green bead, respectively. The

spectral data correctly shows a peak for the green bead near 530 nm and a peak for the red bead near 610 nm. The data also correctly measures the difference in intensity between the two types of beads, with the green beads over 10 times brighter than red beads.

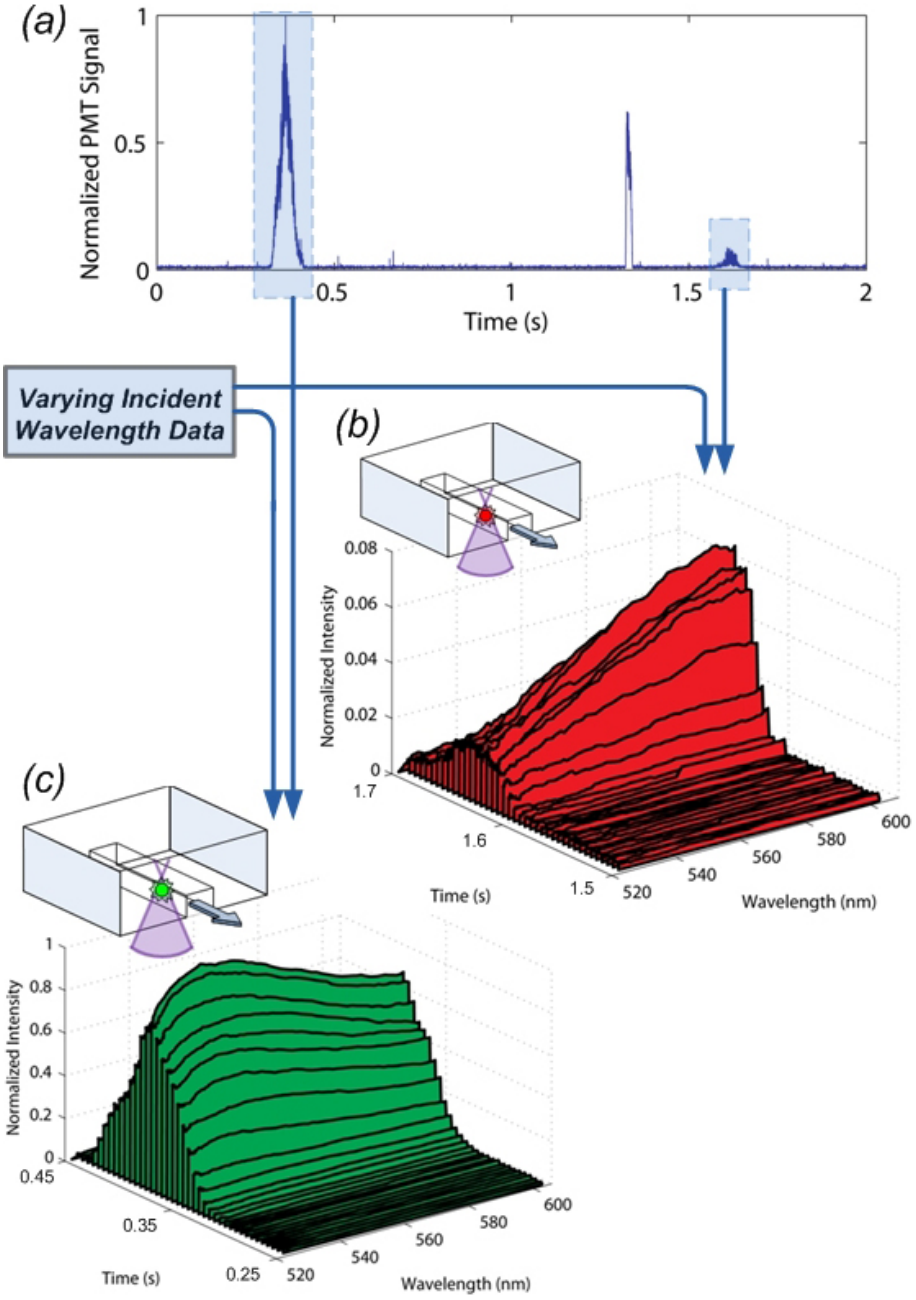

Figure 5.18: Results of spectral cytometry measurements taken with the microfluidic cytometer, microscope setup, and MEMS device. (a) PMT signal as several fluorescent beads pass through the microfluidic channel. (b) Spectral measurements of a red fluorescent bead passing through the microfluidic detection zone. Each plane is a spectral sweep taken with the MEMS device. (c) Spectral measurements of a green fluorescent bead.

These results prove the setup's usefulness for measuring weak fluorescent signals at a rapid pace. As the beads pass by the detection region, multiple spectral sweeps are taken, and the rise and fall of the beads' signals passing through the interrogation zone can be seen. The spectral measurements are able to distinguish the type of bead by its wavelength peak regardless of its relative intensity.

The optical system is next implemented with the cytometry setup with an increase in bead speed and throughput. A solution containing red and green fluorescent beads is again loaded into the sample syringe of the microfluidic cytometer. The sample flow rate and sheathing flow rate are increased so that beads pass through the optical interrogation zone in a time of 5 to 10 ms. The bead concentration is increased in order to raise the number of beads that pass for a given time. The MEMS actuation voltage is set to 1 kHz so that a spectral sweep is taken every millisecond. A calibration measurement is taken using the techniques described previously. A data acquisition system (PCI-6111, National Instruments) is connected to the setup and simultaneously measures the PMT signal and actuation voltage. Figure 5.19 shows the measured PMT signal for one second of cytometry data at a data acquisition scan rate of 1 MS/s. The data shows 22 peaks that each correspond to a passing fluorescent bead.

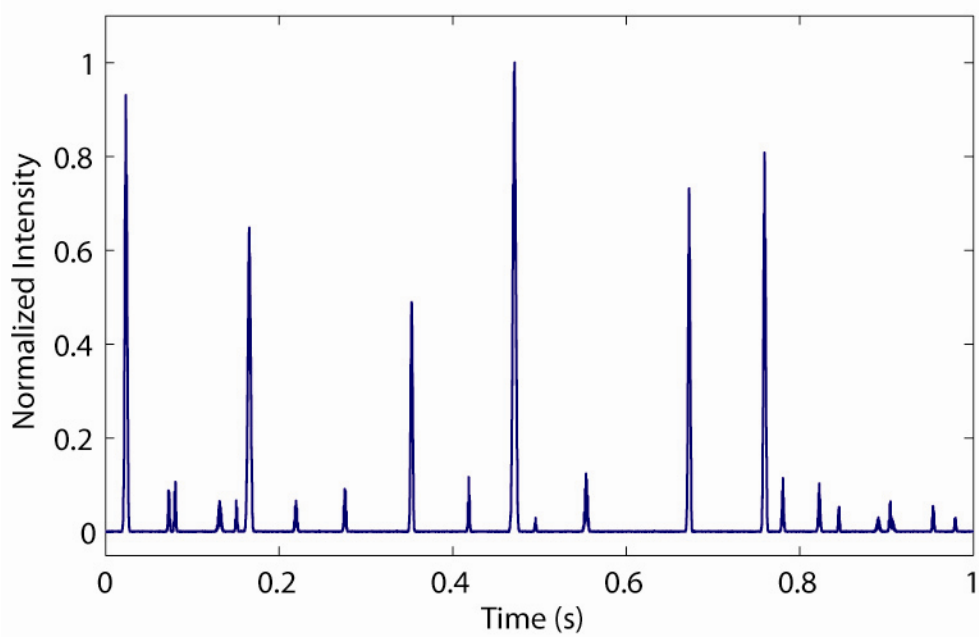

Figure 5.19: Signal from the PMT detector for the high concentration cytometry experiment measured with the data acquisition system.

A closer look at these peaks shows how the actuation of the MEMS device varies the detected signal as the beads pass through the detection region. Figure 5.20 graphs the measured PMT signal from Figure 5.19 for four smaller time increments. Each graph also plots the corresponding MEMS actuation voltage. Units are labeled in the bottom left graph and are the same for all four plots. The data shows that the PMT signal has fluctuations corresponding to the MEMS voltage for each bead that is detected. Figure 5.20(a) has two beads detected with fluctuation peaks corresponding to the maximum of the actuation voltage. Figure 5.20(b) shows a similar detected bead along with a much larger bead signal with fluctuation peaks found near the middle of each voltage ramp. Figure 5.20(c) and (d) show similar detected beads. These fluctuations are due to the spectral sweeps of the MEMS device.

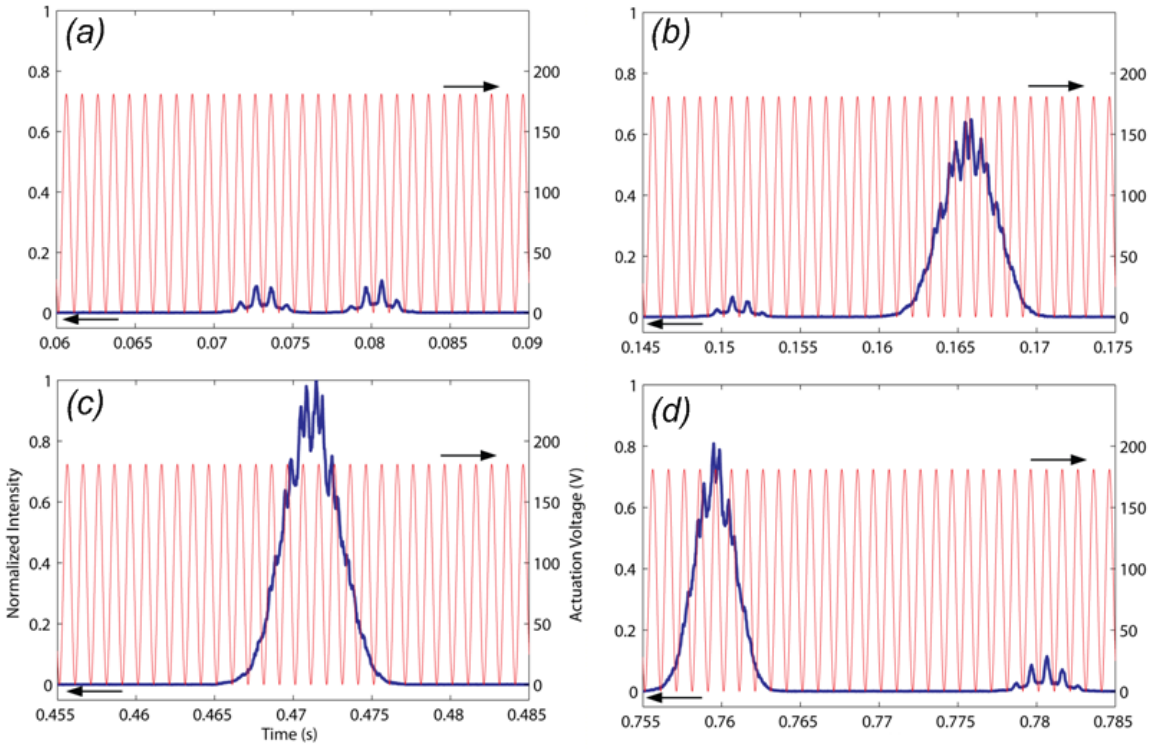

Figure 5.20: PMT data plotted with simultaneous MEMS actuation voltage for four smaller time intervals. PMT signal corresponds to left vertical axis, voltage sine wave corresponds to right vertical axis, units labels are given in bottom left graph and are the same for all four plots. (a) Data for 0.06-0.09 s where two smaller beads pass the interrogation zone of the flow cytometer. (b) Data for 0.145-0.175 s where a small and large bead pass the interrogation zone. (c) Data for 0.455-0.485 s. (d) Data for 0.755-0.785 s.

The incident wavelength is calculated using the voltage signal and characterization data, and the PMT signal is plotted against the incident wavelength to create the spectral plots. The spectral plots are graphed against time to generate three-dimensional graphs that display how the detected spectral signal varies with time. Figure 5.21 shows two of the smaller bead signals and the spectral data reveals that the beads are the weaker red beads as expected. Figure 5.22 shows the continuation of the data for a later time period. The data shows a smaller red bead and a larger green bead with the corresponding spectral signal of each.

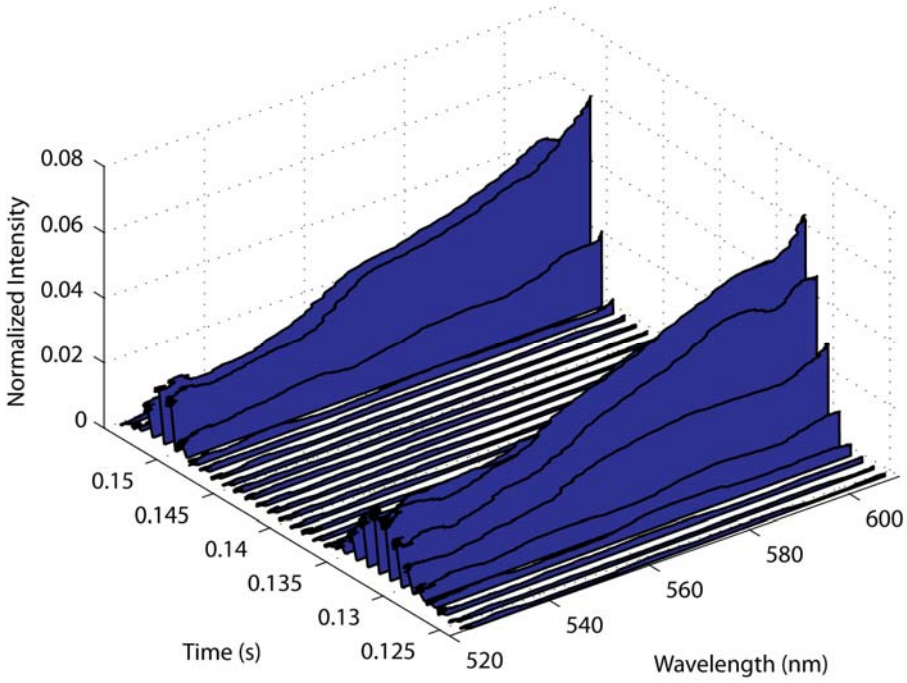

Figure 5.21: Spectral data for two red beads passing through the microfluidic cytometer. Each plane is a spectral sweep taken with the MEMS device and PMT setup.

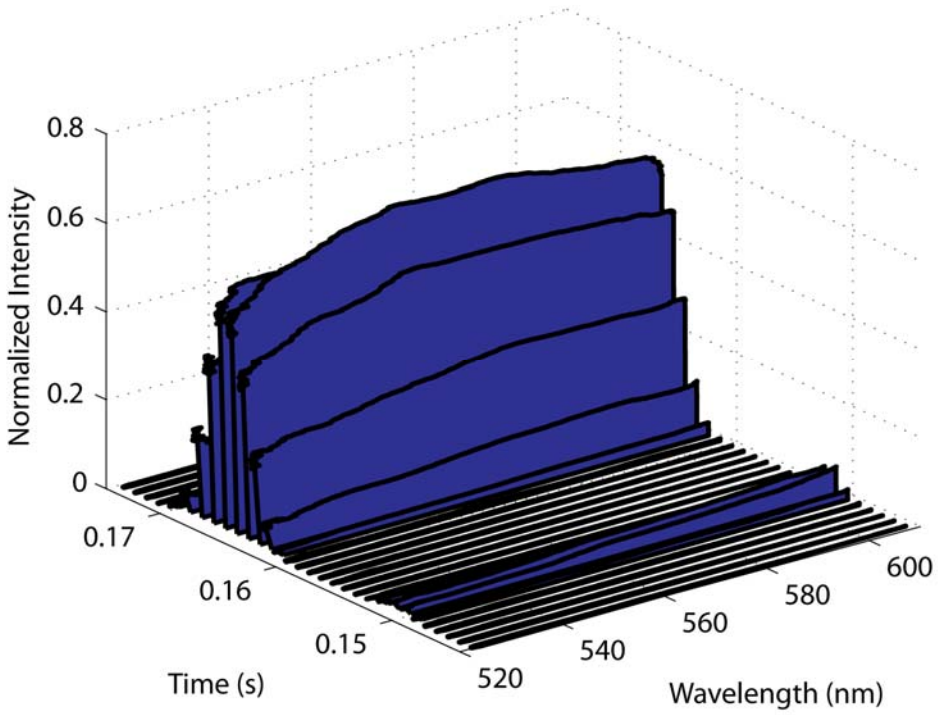

Figure 5.22: Spectral data for a red and larger green bead passing through microfluidic cytometer.

This data further demonstrates the abilities of the optical system in spectral flow cytometry for distinguishing two types of beads using high speed spectral measurements. The different types of beads are distinguishable by the shape of their spectral profile. One side affect seen in this application is the lack of sharp peak detection in the spectral signals. As the beads pass, a background signal is present and generates the overall rise and fall peak shape of the PMT signal for each bead. This is particularly evident in Figure 20(b), (c), and (d) for the larger green beads. With higher bead speeds, this rise and fall of background signal approaches the speed of the spectral sweeps and can interfere with the spectral plot construction. The spectral sweeps only create fluctuation spikes transposed onto a larger rise and fall peak. This background signal is likely due to small inaccuracies of the optical system and distorts the spectral signal by widening the peak with respect to wavelength. However, the fluctuation spikes created by the spectral sweeps are still very repeatable and reliable. In many applications the spectral shapes of the fluorescence tags are already known, and only the discrimination between tags is important. For these applications the general spectral shape measured is sufficient information to identify the fluorescence tag. Following this concept, four or five

fluorescent tags with varying wavelength peaks could be implemented. The spectral plot may be slightly distorted, but the differentiation between tags is still very feasible.

Chapter VI

Conclusions and Future Work

6.1 Summary of Thesis

The research work in this thesis successfully developed a new type of MEMS device and demonstrated its usefulness for optical measurements. The optical system developed around the MEMS device is capable of spectral fluorescence measurements without the dependency on costly detectors and complex optical systems. Several applications exist in fields of cell biology and biomedical engineering. A summary of all the presented achievements are given in the following sections.

6.1.1 Development of Hybrid Microsystems

One of the goals achieved through this research is the further development of incorporating elastic polymer structures within microsystems. Elastic materials have unique material properties and utilizing their capabilities on the microscale in MEMS is a largely undeveloped field of research. This thesis fully details the fabrication steps to PDMS microstructure integration with silicon structures. The capabilities of this technology are explained in detail, and the developed device is a demonstration of the advantages of the polymer utilization. Characteristic measurements also demonstrate the precautions and material properties that need to be fully understood when working with polymers. Unlike materials such as silicon, polymer properties can be highly dependant on factors such as strain rate and the strain history. The development of this unique field

of elastomer hybrid microsystems is an important step in developing more unique and advantageous MEMS devices.

6.1.2 Design and Analysis of Tunable MEMS Optical Grating

The central MEMS device developed in this thesis is an elastic tunable optical grating powered by MEMS electrostatic actuators. This device utilizes the unique capabilities of the PDMS-silicon integration. The PDMS microbridge is highly flexible and can strain elastically much higher than other materials. PDMS is also ideal for reprinting nanometer sized features cost effectively. By exploiting the advantages of both PDMS and silicon, the MEMS device surpasses the capabilities of other similar MEMS devices. The tunable grating period is demonstrated to change from 700 to 820 nm at kHz speed. Other tunable gratings, both MEMS and macro scale, cannot incorporate the high speed, large range, and high line density demonstrated with our device.

This thesis also details an in-depth analysis of this tunable grating. The strain profile is modeled and measured experimentally. Analytical models include both structural mechanics and electrostatic calculations. The polymer properties of creep, stress-softening, and strain drift were also measured and taken into consideration for device implementation. Using a multiwavelength laser signal, the device's high speed and highly sensitive spectral capabilities were demonstrated. Other specifications such as spectral resolution and range were measured and analyzed. The developed MEMS tunable grating has unique properties, and this thesis fully analyzes these advantageous capabilities and less desirable precautions.

6.1.3 Integration of Fluorescent Measurement System

The final major accomplishment of this thesis is the achievement of the primary goal of this thesis. The integration of the MEMS device as the spectral detection system of a fluorescent microscope reduces the detection difficulties presently found in multicolor fluorescence detection. The system is capable of the same high speed, highly sensitive

measurements demonstrated with the MEMS device for any sample used in fluorescence microscope applications. A fluorescence microscope is customized with a fiber optic output that integrates the MEMS spectroscopy setup. All of the possible signal losses and factors affecting the overall system sensitivity are analyzed. As a demonstration of the system speed and sensitivity capabilities, a microfluidic flow cytometer is implemented onto the microscope stage. A sample consisting of two different types of fluorescent beads are run through the microfluidic channel, and multiple spectral sweeps are taken of each passing bead. The system is able to distinguish the beads' different spectral profiles regardless of the relative fluorescent intensity.

The design of a new MEMS chip is also created. The new MEMS devices are designed specifically for the fluorescent microscope applications. The new design and its analysis allows for simple dimensional alterations of the MEMS actuator to custom fit an experiment's fluorescent measurement requirements.

In summary, this work has further developed a new field in MEMS technology, created a unique MEMS optical device that surpasses similar devices, and demonstrated its applications for spectral measurements with minimal detector requirements. The MEMS device and integrated optical system will have short- and long-term impacts in future MEMS and biomedical fields of study.

6.2 Future Research and Applications

The continued work on this research will have a prominent impact in several research fields. The most direct and immediate impact will be from future applications of the designed and fully operational optical system. With the MEMS device integrated with the fluorescent microscope, several applications are available. Fluorescent microscopes are already implemented for several fields of research, and this system can benefit biological studies where the detection of multiple fluorescent tags is restricted by the spectroscope's limited speed and sensitivity. One example of future experiments is the measurements of fluorescent resonant energy transfer (FRET) within tagged cell samples. Research on cellular processes use fluorescently labeled proteins to study certain cell

characteristics such as Ca^{2+} concentrations [97, 98]. The molecular workings of this FRET involve Ca^{2+} causing the emission of one fluorescent protein to excite another protein of different wavelength emission. The calcium ion concentration is then calculated from the change in ratio of the two fluorescent peaks. In short, the spectral profile of two fluorescent peaks must be measured for the same sample, and scientist are continuously looking for systems to make these measurements at a faster time resolution. Figure 6.1 shows an example of spectral measurements taken of a Ca^{2+} FRET experiment [97]. Each graph represents a different variant of a fluorescent protein at zero and saturated Ca^{2+} levels represented by the dotted and solid lines, respectively. The current standard system of a CCD camera and filter wheel yields multiwavelength measurements that take approximately one second per measurement. Applications of our system can dramatically increase these speeds for experiments where time resolution is critical.

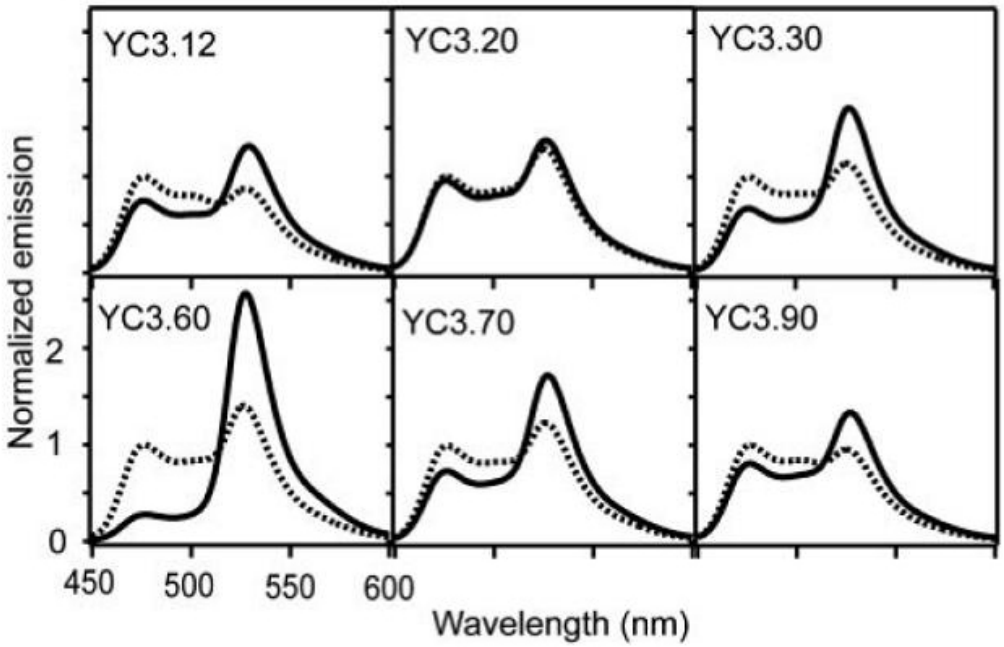

Figure 6.1: Example FRET measurements for determining Ca^{2+} within live cells. Each graph is a variant of a tested protein. Dotted line is at zero Ca^{2+}, and solid line is at saturated Ca^{2+} levels [97].

The designed tunable grating is not limited to potential applications with the microscope system setup. Applications also exist for different optical systems requiring high speed tuning of diffracted optical light. One possible application is the development of medical tools for *in vivo* cancer screening. Current preliminary research is exploring the possibility of a confocal microendoscopy tool for *in vivo* multispectral imaging.

Figure 6.2 shows a proposed setup for implementing the MEMS device with an endoscopic catheter. The results from expanding past white light observations to multiple wavelength detection can lead to better methods for colorectal cancer screening. One of the key components to this type of detection is a means to filter the optical signals at high speeds. The potential of this type of research is dramatic, and correct implementation of the tunable grating could lead to improved cancer detection processes.

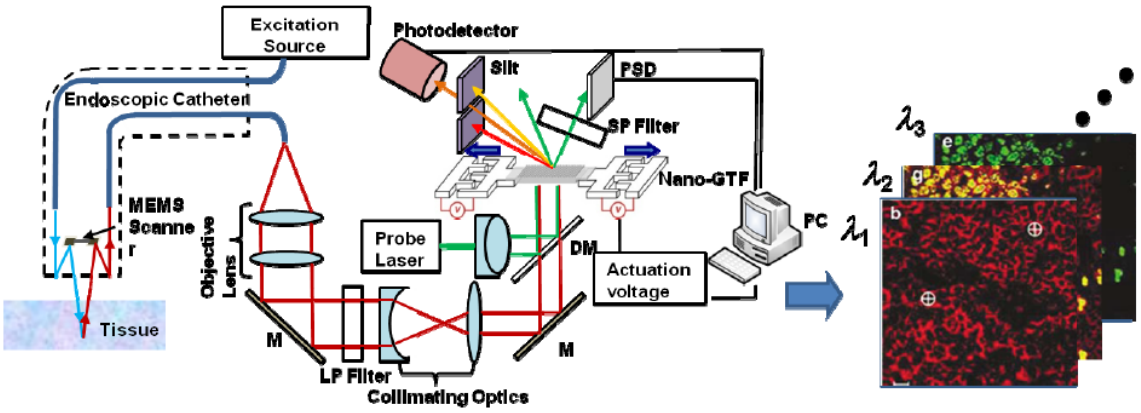

Figure 6.2: Optical schematic of a proposed multispectral confocal endoscopy system. An endoscope collects light from live tissue and directs the light towards the grating. The MEMS device operates as a nano grating tunable filter (Nano-GTF) in order to separate wavelength signals for spectral imaging.

Another potential implementation of the tunable grating is for high speed tuning at the front end of fluorescent measurements. The grating could have applications altering the excitation light at high speeds instead of the emission light. A large concern for cytometry and other fluorescent measurement systems is having an optimal excitation light source. Many cytometers implement up to four different lasers for excitation light, and a specific optimal wavelength is not always easy to create [106]. The tunable grating could be used with a white light source such as a high intensity LED to vary the wavelength of the excitation source. This implementation could reduce the optics and allow for high speed switching to any desirable wavelength within the device's range.

The third branch of future applications of this research is the implementation of the developed PDMS-silicon integration process for other MEMS devices. The potential of this research extends beyond tunable optical gratings, and other types of MEMS can benefit from the integration of elastic materials. The use of PDMS is well established in the microfluidics community, and the implementation of this research could lead to new microfluidic advances. Several microfluidic applications already exploit PDMS's

flexibility to create pneumatically actuated pumps or valves within channels. With the integration of our PDMS-silicon technology, new pumps and valves that operate at much faster speeds using MEMS actuators could be possible. As an example of a recent microfluidic design that may benefit from our research, Beech et al. [107] created a microfluidic sorter that is tunable through mechanically straining the device. Figure 6.3 shows an illustration of the microfluidic channel stretched by a mechanical clamp in order to change the spacing between posts within the channel. A clever design of our integration technology would allow this mechanical tuning to be fast, precise, and voltage actuated.

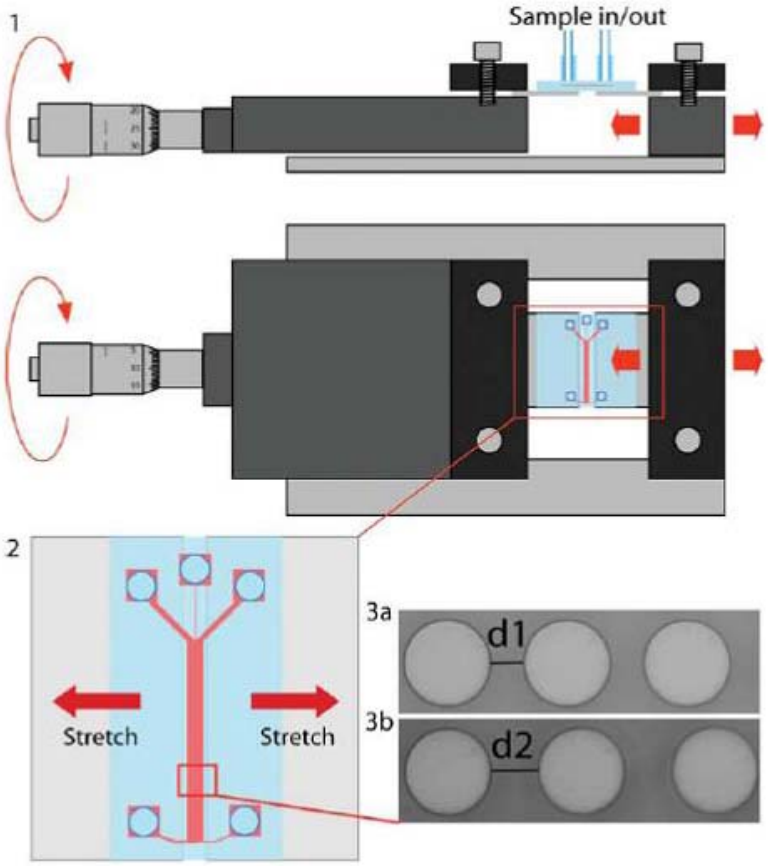

Figure 6.3: A microfluidic sorter that is tunable through mechanical strain. The customized micrometer stretches the PDMS material and changes the spacing between interior posts, a critical dimension for the sorter [107].

To summarize, the future of this research has potential in three distinct branches. The first and most immediate impact can be made through further fluorescent measurement experiments with the developed optical system. The second branch of applications

comes from new, extended implementations of the developed tunable MEMS grating. The final branch of possible future research is the application of the developed PDMS-silicon technology for new, advantageous MEMS devices. In closing, the potential of this research is far reaching, and clever applications may help the smallest of microfabrication problems all the way up to the development of new techniques for cancer detection.

Appendix A

Tunable Grating Fabrication

A.1 SOI Comb-Drive Actuator

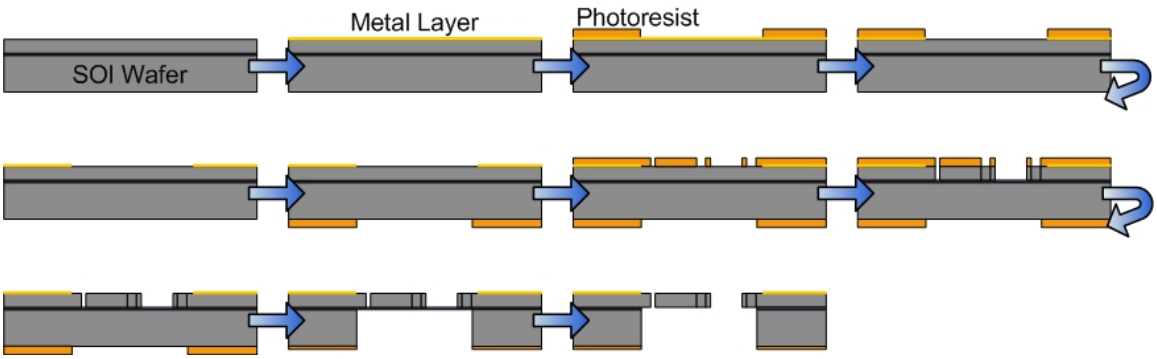

Figure A.1: Fabrication steps for the SOI Actuator.

1. SOI Wafer Clean

    Piranha Clean (H_2SO_4 : H_2O_2 = 1 : 1): 10 min

    BHF Dip: 1 min

    DI Water Rinse: 10 min

    Spin Rinse Dry

2. Dehydration Bake

    Bake on Hotplate: 120°C, 5 min

3. Frontside Metal Deposition

    Enerjet Sputter Coater: Cr 100 Å, Au 1500 Å

4. Photoresist Patterning – Contact Pads

    Photoresist: PR 1827, ~2.7 μm

    Spin: 500 rpm, 4 s + 4000 rpm, 30 s

Soft Bake on Hotplate: 110°C, 1 min 10 s

Cool Down in Ambient: >5 min

Exposure (MA6 Mask Aligner): 11 s

Development (MF-319): 1 min

DI Water Rinse: 5 min

Descum in March Asher: O_2, 80 W, 250 mT, 1 min

5. Metal Etching

Gold Etchant: Eye Inspection (~1 min)

Cr Etchant: Eye Inspection (~1 min)

6. Photoresist Removal

PRS-2000 Soak: >10 min

Acetone Rinse: 1 min

IPA Rinse: 1 min

DI Water Rinse: 5 min

Spin Rinse Dry

7. Backside Patterning – Backside Through Wafer Etch Pattern

Photoresist: SU-8 2015, ~17 μm

Spin: 500 rpm, 10 s + 2500 rpm, 30 s

Soft Bake on Hotplate: 95°C, 3 min 45 s

Cool Down in Ambient: >10 min

Backside Alignment and Exposure (MA6 Mask Aligner): 13.5 s

Post Exposure Bake on Hotplate: 95°C, 4 min 15 s

Cool Down in Ambient: >10 min

Development (SU-8 Developer): 2 min

Visual Inspection, Develop Further if Needed

IPA Rinse: 1 min

Descum in March Asher: O_2, 80 W, 250 mT, 1 min

Hard Bake on Hotplate: 65°C to 150°C + 150°C, 10 min + 150°C to 65°C

8. Frontside Clean

Acetone Rinse: 1 min

IPA Rinse: 1 min

9. Frontside Photoresist Patterning – Comb-Drive Actuator Patterns

Photoresist: AZ 9260, ~6.7 μm

HMDS Spin: 4000 rpm, 10 s

Photoresist Spin: 500 rpm, 8 s + 4000 rpm, 30 s

Soft Bake on Hotplate: 110°C, 3 min 30 s

Cool Down in Ambient: >5 min

Frontside Alignment and Exposure (MA6 Mask Aligner): 28 s

Development (AZ 400K : DI = 1 : 3): 1 min 15 s

Visual Inspection, Develop Further if Needed

DI Water Rinse: 5 min

Descum in March Asher: O_2, 80 W, 250 mT, 1 min

10. Frontside DRIE

DRIE in STS ICP Machine: Recipe TYC-HR2, 46 min

Visual Inspection, Ensure Etch to Buried Oxide Layer

11. Frontside Photoresist Removal

BHF Dip: 30 s

Acetone Soak: 30 min

IPA Rinse: 1 min

DI Water Rinse: 10 min

Spin Rinse Dry

Ashing in March Asher: O_2, 200 W, 250 mT, 10 min

12. Frontside Photoresist for Dicing Protection

Photoresist: AZ 9260

HMDS Spin: 4000 rpm, 10 s

Photoresist Spin: 500 rpm, 8 s + 4000 rpm, 30 s

Soft Bake on Hotplate: 110°C, 3 min 30 s

13. Wafer Dicing

Dicing with MA 1006 Dicing Saw: Blade 42525

14. Carrier Wafer Mounting

Spin AZ 9260 Photoresist onto Si Carrier Wafer

Place SOI Die onto Carrier Wafer, Backside Facing Up

Soft Bake on Hotplate: 110°C, 3 min 30 s

15. SOI Backside Etching

Backside DRIE in STS ICP Machine: Recipe TYC-TH1, 2 hr 30 min

Backside DRIE in STS ICP Machine: Recipe TYC-HR2, 10 min

Repeat Etch until Buried Oxide Layer Fully Exposed

16. Carrier Wafer and Photoresist Removal

Acetone Soaking: Until SOI Die Released from Carrier Wafer

PRS-2000 Soak: 20 min

DI Water Soak: 10 min

Methanol Soak: 10 min

Dry on Hotplate: 120°C, 5 min

Frontside Ashing in March Asher: O_2, 200 W, 250 mT, 10 min

17. Buried Silicon Dioxide Etch

BHF SiO_2 Etching: 25 min

DI Water Soak: 5 min

Methanol Soak: 10 min

Dry on Hotplate: 120°C, 5 min

A.2 Top Mold Fabrication

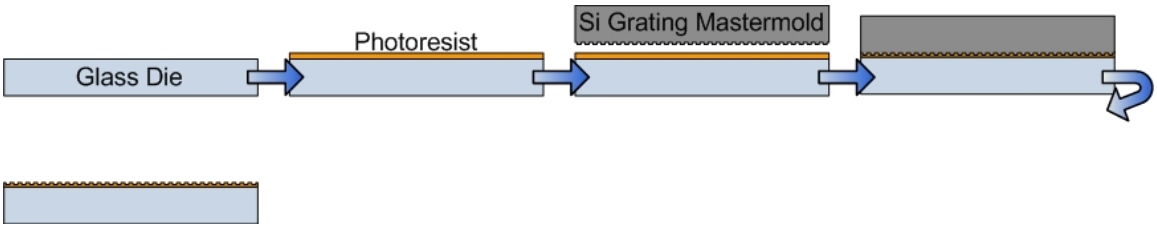

Figure A.2: Fabrication steps for the Top Mold.

1. Pyrex Glass Wafer Clean

Piranha Clean (H_2SO_4 : H_2O_2 = 1 : 1): 10 min

DI Water Rinse: 10 min

Spin Rinse Dry

2. Metal Deposition

EnerJet Sputter Coater: Cr 100 Å, Au 1500 Å

3. Dehydrate Bake

Bake on Hotplate: 120°C, 5 min

4. Photoresist Patterning – Top Mold Dicing Line Pattern

Photoresist: PR 1827, ~2.7 μm

HMDS Spin: 4000 rpm, 10 s

Photoresist Spin: 500 rpm, 4 s + 4000 rpm, 30 s

Soft Bake on Hotplate: 110°C, 1 min 10 s

Cool Down in Ambient: >5 min

Exposure (MA6 Mask Aligner): 11 s

Development (MF-319): 1 min

5. Metal Etching

Gold Etchant: Eye Inspection (~1 min)

Cr Etchant: Eye Inspection (~1 min)

6. Photoresist Removal

PRS-2000 Soaking: >10 min

Acetone Rinse: 1 min

IPA Rinse: 1 min

DI Water Rinse: >10 min

Spin Rinse Dry

7. Dehydrate Bake

Bake on Hotplate: 120°C, 5 min

8. Photoresist for Nanoimprinting

Photoresist: AZ 9260, ~6.7 μm

HMDS Spin: 4000 rpm, 10 sec

Photoresist Spin: 500 rpm, 8 sec + 4000 rpm, 30 sec

Hard Bake on Hotplate: 180°C, 11 min

9. Wafer Dicing

Dicing with MA 1006 Dicing Saw: Blade 777

10. Grating Pattern Imprinting

Nanoimprint Lithography (Nanonex Imprinter): 600 psi, 170°C, 5 min

A.3 Bottom Mold Fabrication

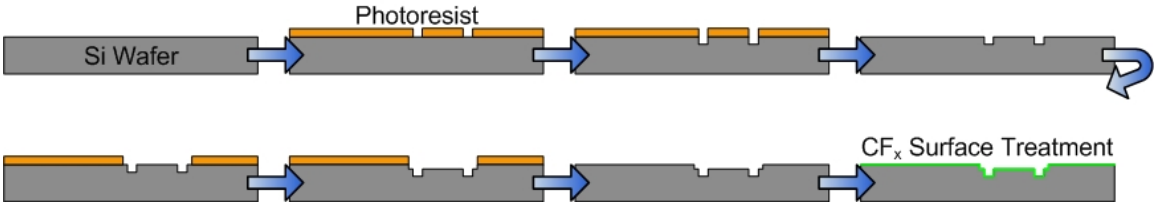

Figure A.3: Fabrication step of the Bottom Mold.

1. Silicon Wafer Clean

    Piranha Clean (H_2SO_4 : H_2O_2 = 1 : 1): 10 min

    BHF Dip: 1 min

    DI Water Rinse: 10 min

    Spin Rinse Dry

2. Dehydration Bake

    Bake on Hotplate: 120°C, 5 min

3. Photoresist Patterning – Bottom Mold Mask 1

    Photoresist: AZ 9260, ~6.7 μm

    Photoresist Spin: 500 rpm, 8 s + 4000 rpm, 30 s

    Soft Bake on Hotplate: 110°C, 3 min 30 s

    Cool Down in Ambient, 10 min

    Exposure (MA6 Mask Aligner): 28 s

    Development (AZ 400K : DI = 1 : 3): 1 min 15 s

    Visual Inspection, Develop Further if Needed

    DI Water Rinse, 5 min

    Descum in March Asher: O_2, 80 W, 250 mT, 1 min

4. Bottom Mold Layer 1 DRIE

    DRIE on STS ICP machine: Recipe TUNGY1, ~2 μm/min

5. Photoresist Removal

    PRS-2000 Soaking: >10 min

    BHF Dip: 1 min

    DI Water Rinse: 10 min

    Spin Rinse Dry

6. Dehydration Bake

Bake on Hotplate: 120°C, 5 min

7. Photoresist Patterning – Bottom Mold Mask 2

Photoresist: SU-8 2015, ~17 μm

Spin: 500 rpm, 10 s + 2500 rpm, 30 s

Soft Bake on Hotplate: 95°C, 3 min 45 s

Cool Down in Ambient: >10 min

Frontside Alignment and Exposure (MA6 Mask Aligner): 13.5 s

Post Exposure Bake on Hotplate: 95°C, 4 min 15 s

Cool Down in Ambient: >10 min

Development (SU-8 Developer): 2 min

Visual Inspection, Develop Further if Needed

IPA Rinse: 1 min

Descum in March Asher: O_2, 80 W, 250 mT, 1 min

8. Bottom Mold Layer 2 DRIE

DRIE on STS ICP machine: Recipe TUNGY1, ~2 μm/min

9. Photoresist Removal

Piranha Clean (H_2SO_4 : H_2O_2 = 1 : 1): 20 min

BHF Dip: 1 min

DI Water Rinse: 10 min

Spin Rinse Dry

10. Frontside Photoresist for Dicing Protection

Photoresist: AZ 9260

HMDS Spin: 4000 rpm, 10 s

Photoresist Spin: 500 rpm, 8 sec + 4000 rpm, 30 s

Soft Bake on Hotplate: 110°C, 3 min 30 s

11. Wafer Dicing

Dicing with MA 1006 Dicing Saw: Blade 42525

12. Protection Photoresist Removal

PRS-2000 Soaking: >10 min

Acetone Rinse: 1 min

IPA Rinse: 1 min

DI Water Rinse : 10 min

13. Bottom Mold Surface Treatment

CF_x Layer Deposition on STS ICP machine: Recipe TUNGY2, 30 s

Anneal on Hotplate: 150°C, 5 min

A.4 PDMS Microstructure Fabrication

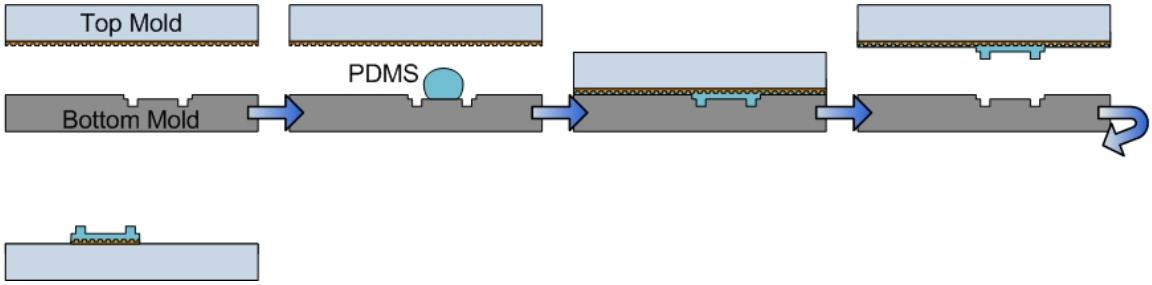

Figure A.4: Fabrication steps of PDMS microstructure molding.

1. PDMS Precursor Preparation

PDMS Precursor Mixing: Sylgard 184 (Base : Curing Agent = 10 : 1)

Degas in Desiccator: 30 min

2. PDMS Micro-Molding

Dispense a Drop of PDMS Precursor on Bottom Mold

Place Top Mold onto Bottom Mold with Photoresist Grating Pattern Facing Down

Cure PDMS in HP Press: 600 psi, 150°C, 1 hr

Remove Bottom Mold

3. Residual PDMS Layer Removal

Etching in Plasmatherm 790: Recipe sct_2, 45 min

Eye Inspection, Continue Etch if Needed

A.5 PDMS Structure/SOI Comb-Drive Assembly and Release

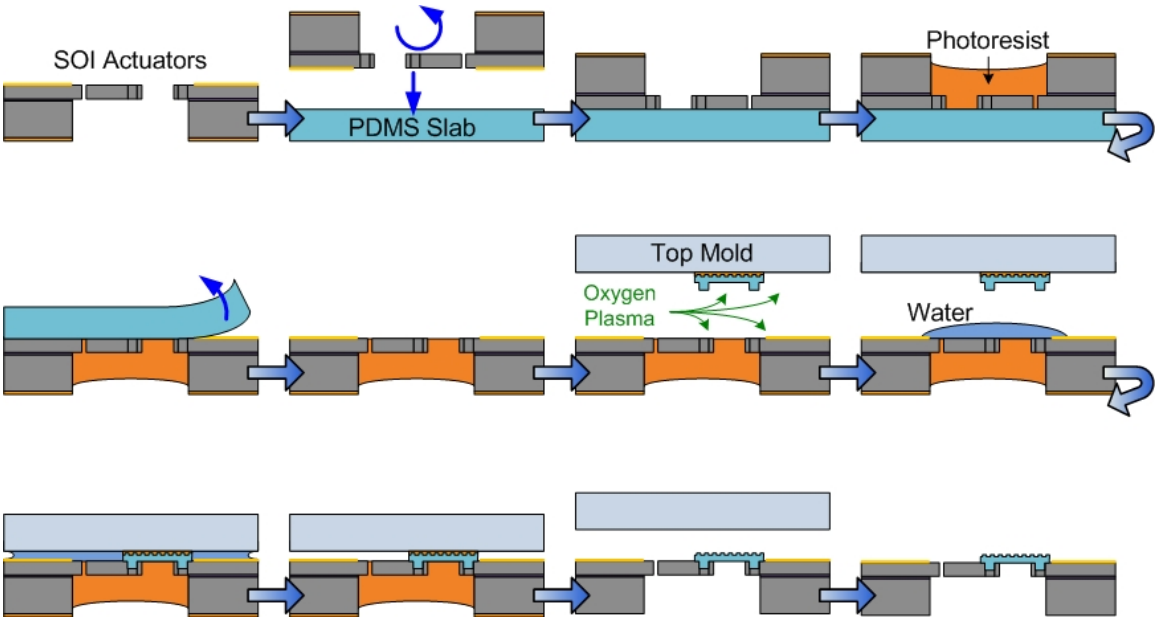

Figure A.5: Fabrication steps for the final device assembly.

1. Immobilizing Suspended Comb-Drive Structures

    Cure PDMS Slab 2 mm Thick and Cut into 2.5 x 2.5 cm Squares

    Place SOI Die onto PDMS Slab with Comb-Drive Structures Facing Down

    Fill Backside Through Holes with Drops of AZ 9260 Photoresist

    Bake on Hotplate: 110°C, 15 min

    Cool Down in Ambient, >10 min

    Peel PDMS Slab from SOI Die

2. Grafting of PDMS Microstructure onto SOI Patterns

    Oxygen Plasma Surface Treatment in March Asher: O_2, 80W, 250 mT, 45 s

    Dispense a Drop of DI Water on SOI Patterns

    Place Top Mold onto SOI Patterns with PDMS Microstructures Facing Down

    Align PDMS Microstructure under Stereo-Microscope

    Evaporate DI Water on Hotplate: 60°C, 30 min

    Add Weight (~1 kg) While on Hotplate for Pressure Assisted Bonding

3. Device Release

PRS-2000 Soak for Top Mold Release: Eye Inspection

PRS-2000 Soak: Additional 60 min After Top Mold Release

DI Water Soak: 20 min

Methanol Soak: 20 min

Evaporate Methanol on Hotplate: 120°C, 5 min

Appendix B

Microfluidic Cytometer Fabrication

B.1 Microfluidic Channel Mold Fabrication

1. Silicon Wafer Clean

    Piranha Clean (H_2SO_4 : H_2O_2 = 1 : 1): 10 min

    BHF Dip: 1 min

    DI Water Rinse: 10 min

    Spin Rinse Dry

2. Dehydration Bake

    Bake on Hotplate: 120°C, 5 min

3. Photoresist Patterning – Microfluidic Cytometry Mask

    Photoresist: SU-8 2050, ~70 μm

    Spin: 500 rpm, 10 s + 2000 rpm, 30 s

    Soft Bake on Hotplate: 65°C, 3 min + 95°C, 9 min

    Cool Down in Ambient: >10 min

    Exposure (MA6 Mask Aligner): 20 s

    Post Exposure Bake on Hotplate: 65°C, 2 min + 95°C, 7 min

    Cool Down in Ambient: >10 min

    Development (SU-8 Developer): 7 min

    Visual Inspection, Develop Further if Needed

    IPA Rinse: 1 min

    Hard Bake on Hotplate: 65°C to 160°C + 160°C, 10 min + 160°C to 65°C

B.2 PDMS Channel Fabrication

1. PDMS Precursor Preparation

    PDMS Precursor Mixing: Sylgard 184 (Base : Curing Agent = 10 : 1)

    Degas in Desiccator: 30 min

2. PDMS Soft Lithography

    Place Wafer Containing Microfluidic Channel Mold in Petri Dish

    Pour PDMS Over Mold, ~4 mm thick

    Degas in Desiccator: 30 min

    Cure PDMS on Hotplate: 150°C, 10 min

    Cool Down in Ambient: >20 min

    Peel PDMS from Si Wafer and Mold

3. Inlets/Outlet Fabrication

    Cut Holes Through PDMS Using Biopsy Punch, 1.5 mm

B.3 Microfluidic Channel Assembly

1. Pyrex Glass Wafer Clean (200 μm thick)

    Piranha Clean (H_2SO_4 : H_2O_2 = 1 : 1): 10 min

    DI Water Rinse: 10 min

    Spin Rinse Dry

2. Wafer Dicing

    Dicing with MA 1006 Dicing Saw: Blade 777

3. Channel Assembly from PDMS Mold and Glass Die

    Oxygen Plasma Surface Treatment in March Asher: O_2, 80W, 250 mT, 45 s

    Place PDMS Mold onto Glass Die with Channel Facing Down

    Apply Weight (~1 kg) to Assist Bonding: 30 min

    Remove Weight

References

[1] J. R. Lakowicz, *Principles of Fluorescence Spectroscopy*, Third ed. Baltimore, MD: Springer Science+Business Media, 2006.

[2] J. F. James and R. S. Sternberg, *The Design of Optical Spectrometers*. London: Chapman and Hall LTD, 1969.

[3] S. Grabarnik, R. Wolffenbuttel, A. Emadi, M. Loktev, E. Sokolova, and G. Vdovin, "Planar double-grating microspectrometer," *Optics Express,* vol. 15, pp. 3581-3588, Mar 2007.

[4] M. C. Moreno-Bondi, J. P. Alarie, and T. Vo-Dinh, "Multi-analyte analysis system using an antibody-based biochip," *Analytical and Bioanalytical Chemistry,* vol. 375, pp. 120-124, Jan 2003.

[5] T. M. Phillips, "Multi-analyte analysis of biological fluids with a recycling immunoaffinity column array," *Journal of Biochemical and Biophysical Methods,* vol. 49, pp. 253-262, Oct 2001.

[6] M. Bossi, J. Folling, V. N. Belov, V. P. Boyarskiy, R. Medda, A. Egner, C. Eggeling, A. Schonle, and S. W. Hell, "Multicolor far-field fluorescence nanoscopy through isolated detection of distinct molecular species," *Nano Letters,* vol. 8, pp. 2463-2468, Aug 2008.

[7] P. K. Chattopadhyay, D. A. Price, T. F. Harper, M. R. Betts, J. Yu, E. Gostick, S. P. Perfetto, P. Goepfert, R. A. Koup, S. C. De Rosa, M. P. Bruchez, and M. Roederer, "Quantum dot semiconductor nanocrystals for immunophenotyping by polychromatic flow cytometry," *Nature Medicine,* vol. 12, pp. 972-977, Aug 2006.

[8] I. L. Medintz, H. T. Uyeda, E. R. Goldman, and H. Mattoussi, "Quantum dot bioconjugates for imaging, labelling and sensing," *Nature Materials,* vol. 4, pp. 435-446, Jun 2005.

[9] X. Michalet, F. F. Pinaud, L. A. Bentolila, J. M. Tsay, S. Doose, J. J. Li, G. Sundaresan, A. M. Wu, S. S. Gambhir, and S. Weiss, "Quantum dots for live cells, in vivo imaging, and diagnostics," *Science,* vol. 307, pp. 538-544, Jan 2005.

[10] T. K. Kerppola, "Bimolecular fluorescence complementation: Visualization of molecular interactions in living cells," in *Fluorescent Proteins, Second Edition*. vol. 85 San Diego: Elsevier Academic Press Inc, 2008, pp. 431-+.

[11] M. Schieker, C. Pautke, F. Haasters, J. Schieker, D. Docheva, W. Bocker, H. Guelkan, P. Neth, M. Jochum, and W. Mutschler, "Human mesenchymal stem cells at the single-cell level: simultaneous seven-colour immunofluorescence," *Journal of Anatomy,* vol. 210, pp. 592-599, May 2007.

[12] L. C. Hwang, M. Gosch, T. Lasser, and T. Wohland, "Simultaneous multicolor fluorescence cross-correlation spectroscopy to detect higher order molecular interactions using single wavelength laser excitation," *Biophysical Journal,* vol. 91, pp. 715-727, Jul 2006.

[13] M. Gad-el-Hak, *The MEMS Handbook*. New York: CRC Press, 2002.

[14] P. T. Mather, "Soft answers for hard problems," *Nature Materials,* vol. 6, pp. 93-94, Feb 2007.

[15] M. Shahinpoor, "Ionic polymer-conductor composites as biomimetic sensors, robotic actuators and artificial muscles - a review," *Electrochimica Acta,* vol. 48, pp. 2343-2353, Jun 2003.

[16] H. H. Yu and T. M. Swager, "Molecular actuators - Designing actuating materials at the molecular level," *IEEE Journal of Oceanic Engineering,* vol. 29, pp. 692-695, Jul 2004.

[17] C. Liu, H. Qin, and P. T. Mather, "Review of progress in shape-memory polymers," *Journal of Materials Chemistry,* vol. 17, pp. 1543-1558, 2007.

[18] R. Pelrine, R. Kornbluh, Q. B. Pei, and J. Joseph, "High-speed electrically actuated elastomers with strain greater than 100%," *Science,* vol. 287, pp. 836-839, Feb 2000.

[19] D. J. Beebe, J. S. Moore, J. M. Bauer, Q. Yu, R. H. Liu, C. Devadoss, and B. H. Jo, "Functional hydrogel structures for autonomous flow control inside microfluidic channels," *Nature,* vol. 404, pp. 588-+, Apr 2000.

[20] E. W. H. Jager, E. Smela, and O. Inganas, "Microfabricating conjugated polymer actuators," *Science,* vol. 290, pp. 1540-1545, Nov 2000.

[21] A. Athanassiou, M. Kalyva, K. Lakiotaki, S. Georgiou, and C. Fotakis, "Laser controlled mechanical actuation of photochromic-polymer microsystems," *Reviews on Advanced Materials Science,* vol. 5, pp. 245-251, 2003.

[22] E. Smela, "Conjugated polymer actuators for biomedical applications," *Advanced Materials,* vol. 15, pp. 481-494, Mar 2003.

[23] C. D. Dimitrakopoulos and P. R. L. Malenfant, "Organic thin film transistors for large area electronics," *Advanced Materials,* vol. 14, pp. 99-+, Jan 2002.

[24] G. Horowitz, "Organic thin film transistors: From theory to real devices," *Journal of Materials Research,* vol. 19, pp. 1946-1962, Jul 2004.

[25] L. J. Kricka, "Multianalyte Testing," *Clinical Chemistry,* vol. 38, pp. 327-328, 1992.

[26] Y. Hiraoka, T. Shimi, and T. Haraguchi, "Multispectral imaging fluorescence microscopy for living cells," *Cell Structure and Function,* vol. 27, pp. 367-374, 2002.

[27] A. Schonle and S. W. Hell, "Fluorescence nanoscopy goes multicolor," *Nature Biotechnology,* vol. 25, pp. 1234-1235, 2007.

[28] M. Bates, B. Huang, G. T. Dempsey, and X. W. Zhuang, "Multicolor super-resolution imaging with photo-switchable fluorescent probes," *Science,* vol. 317, pp. 1749-1753, 2007.

[29] S. P. Perfetto, P. K. Chattopadhyay, and M. Roederer, "Seventeen-colour flow cytometry: unravelling the immune system," *Nature Reviews Immunology,* vol. 4, pp. 648-U5, Aug 2004.

[30] E. I. Galanzha, E. V. Shashkov, V. V. Tuchin, and V. P. Zharov, "In vivo multispectral, multiparameter, photoacoustic lymph flow cytometry with natural cell focusing, label-free detection and multicolor nanoparticle probes," *Cytometry A,* vol. 73, pp. 884-94, 2008.

[31] D. A. Ateya, J. S. Erickson, P. B. Howell, L. R. Hilliard, J. P. Golden, and F. S. Ligler, "The good, the bad, and the tiny: a review of microflow cytometry," *Analytical and Bioanalytical Chemistry,* vol. 391, pp. 1485-1498, Jul 2008.

[32] C. Snow, "Flow cytometer electronics," *Cytometry Part A,* vol. 57A, pp. 63-69, Feb 2004.

[33] X. Michalet, O. H. W. Siegmund, J. V. Vallerga, P. Jelinsky, J. E. Millaud, and S. Weiss, "Detectors for single-molecule fluorescence imaging and spectroscopy," *Journal of Modern Optics,* vol. 54, pp. 239-281, Jan 2007.

[34] W. E. Moerner and D. P. Fromm, "Methods of single-molecule fluorescence spectroscopy and microscopy," *Review of Scientific Instruments,* vol. 74, pp. 3597-619, 2003.

[35] A. K. Luong, G. C. Gradinaru, D. W. Chandler, and C. C. Hayden, "Simultaneous time- and wavelength-resolved fluorescence microscopy of single molecules," *Journal of Physical Chemistry B,* vol. 109, pp. 15691-15698, Aug 2005.

[36] D. S. Goldman, P. L. White, and N. C. Anheier, "Miniaturized spectrometer employing planar waveguides and grating couplers for chemical analysis," *Applied Optics,* vol. 29, pp. 4583-9, 1990.

[37] J. Mohr, B. Anderer, W. Ehrfeld, and Fu, "Fabrication of a Planar Grating Spectrograph by Deep-Etch Lithography with Synchrotron Radiation," *Sensors and Actuators A-Physical,* vol. 27, pp. 571-575, May 1991.

[38] D. Sander and J. Muller, "Self-focussing phase trasmission grating for an integrated optical spectrometer," *Sensors and Actuators A: Physical,* vol. 88, pp. 1-9, 2001.

[39] G. M. Yee, N. I. Maluf, P. A. Hing, M. Albin, and G. T. A. Kovacs, "Miniature spectrometers for biochemical analysis," *Sensors and Actuators A: Physical,* vol. 58, pp. 61-66, 1997.

[40] O. Schmidt, M. Bassler, P. Kiesel, C. Knollenberg, and N. Johnson, "Fluorescence spectrometer-on-a-fluidic-chip," *Lab on a Chip,* vol. 7, pp. 626-629, 2007.

[41] S. Traut and H. P. Herzig, "Holographically recorded gratings on microlenses for a miniaturized spectrometer array," *Optical Engineering,* vol. 39, pp. 290-298, Jan 2000.

[42] R. F. Wolffenbuttel, "State-of-the-art in integrated optical microspectrometers," *IEEE Transactions on Instrumentation and Measurement,* vol. 53, pp. 197-202, Feb 2004.

[43] R. F. Wolffenbuttel, "MEMS-based optical mini- and microspectrometers for the visible and infrared spectral range," *Journal of Micromechanics and Microengineering,* vol. 15, pp. S145-S152, Jul 2005.

[44] G. Minas, J. C. Ribeiro, R. F. Wolffenbuttel, and J. H. Correia, "On-chip integrated CMOS optical detection microsystem for spectrophotometric analyses in biological microfluidic systems," in *Industrial Electronics, ISIE 2005.*, pp. 1133-1138 vol. 3.

[45] G. Minas, R. F. Wolffenbuttel, and J. H. Correia, "An array of highly selective "Fabry-Perot optical channels for biological fluid analysis by optical absorption using a white light source for illumination," *Journal of Optics A-Pure and Applied Optics,* vol. 8, pp. 272-278, Mar 2006.

[46] N. Damean, S. K. Sia, V. Linder, M. Narovlyansky, and G. M. Whitesides, "Space- and time-resolved spectrophotometry in microsystems," *Proceedings of the National Academy of Sciences of the United States of America,* vol. 102, pp. 10035-10039, Jul 2005.

[47] G. M. Yee, N. I. Maluf, P. A. Hing, M. Albin, G. T. A. Kovacs, and Xj, "Miniature spectrometers for biochemical analysis," *Sensors and Actuators A-Physical,* vol. 58, pp. 61-66, Jan 1997.

[48] C. Palmer, *Diffraction Grating Handbook*, 5th Edition ed. Rochester, NY: Thermo RGL, 2002.

[49] Q. Y. Fang, T. Papaioannou, J. A. Jo, R. Vaitha, K. Shastry, and L. Marcu, "Time-domain laser-induced fluorescence spectroscopy apparatus for clinical diagnostics," *Review of Scientific Instruments,* vol. 75, pp. 151-162, Jan 2004.

[50] P. V. Butte, B. K. Pikul, A. Hever, W. H. Yong, K. L. Black, and L. Marcu, "Diagnosis of meningioma by time-resolved fluorescence spectroscopy," *Journal of Biomedical Optics,* vol. 10, p. 9, Nov-Dec 2005.

[51] A. Q. Liu, X. M. Zhang, J. Li, and C. Lu, "Single-/multi-mode tunable lasers using MEMS mirror and grating," *Sensors and Actuators A-Physical,* vol. 108, pp. 49-54, Nov 2003.

[52] Y.-S. Yang and C.-H. Liu, "Design and fabrication of pitch tunable blaze grating," in *Progress in Biomedical Optics and Imaging - Proceedings of SPIE, MEMS/MOEMS Components and Their Applications II*, San Jose, CA, United States, 2005, pp. 99-107.

[53] W. C. Shih, S. G. Kim, and G. Barbastathis, "High-resolution electrostatic analog tunable grating with a single-mask fabrication process," *Journal of Microelectromechanical Systems,* vol. 15, pp. 763-769, Aug 2006.

[54] M. Tormen, Y. A. Peter, P. Niedermann, A. Hoogerwerf, and R. Stanley, "Deformable MEMS grating for wide tunability and high operating speed," *Journal of Optics A-Pure and Applied Optics,* vol. 8, pp. S337-S340, Jul 2006.

[55] X. M. Zhang, Q. W. Zhao, T. Zhong, A. B. Yu, E. H. Khoo, C. Lu, and A. Q. Liu, "Variable Nano-Grating for Tunable Filters," in *Solid-State Sensors, Actuators and Microsystems Conference, 2007. TRANSDUCERS 2007. International*, 2007, pp. 2417-2420.

[56] C. W. Wong, Y. Jeon, G. Barbastathis, and S. G. Kim, "Analog piezoelectric-driven tunable gratings with nanometer resolution," *Journal of Microelectromechanical Systems,* vol. 13, pp. 998-1005, Dec 2004.

[57] J. F. Lo, S.-J. Chen, H. Yu, D. Chi, C.-Y. Lee, L. Marcu, E. S. Kim, and M. Gundersen, "Multi-Cantilever-Driven Rotational Micrograting for MOEMS Spectrometer," in *Solid-State Sensors, Actuators and Microsystems Conference, 2007. Transducers 2007. International*, 2007, pp. 2421-2424.

[58] K. Hosokawa, K. Hanada, and R. Maeda, "A polydimethylsiloxane (PDMS) deformable diffraction grating for monitoring of local pressure in microfluidic devices," *Journal of Micromechanics and Microengineering,* vol. 12, pp. 1-6, Jan 2002.

[59] M. Aschwanden and A. Stemmer, "Polymeric, electrically tunable diffraction grating based on artificial muscles," *Optics Letters,* vol. 31, pp. 2610-2612, Sep 2006.

[60] A. N. Simonov, O. Akhzar-Mehr, and G. Vdovin, "Light scanner based on a viscoelastic stretchable grating," *Optics Letters,* vol. 30, pp. 949-951, May 2005.

[61] M. A. Unger, H. P. Chou, T. Thorsen, A. Scherer, and S. R. Quake, "Monolithic microfabricated valves and pumps by multilayer soft lithography," *Science,* vol. 288, pp. 113-116, Apr 2000.

[62] D. Huh, K. L. Mills, X. Y. Zhu, M. A. Burns, M. D. Thouless, and S. Takayama, "Tuneable elastomeric nanochannels for nanofluidic manipulation," *Nature Materials,* vol. 6, pp. 424-428, Jun 2007.

[63] M. L. Chabinyc, D. T. Chiu, J. C. McDonald, A. D. Stroock, J. F. Christian, A. M. Karger, and G. M. Whitesides, "An integrated fluorescence detection system in poly(dimethylsiloxane) for microfluidic applications," *Analytical Chemistry,* vol. 73, pp. 4491-4498, Sep 2001.

[64] Y. C. Tung, M. Zhang, C. T. Lin, K. Kurabayashi, and S. J. Skerlos, "PDMS-based opto-fluidic micro flow cytometer with two-color, multi-angle fluorescence detection capability using PIN photodiodes," *Sensors and Actuators B: Chemical,* vol. 98, pp. 356-367, 2004.

[65] J. C. Lotters, W. Olthuis, P. H. Veltink, and P. Bergveld, "The mechanical properties of the rubber elastic polymer polydimethylsiloxane for sensor applications," *Journal of Micromechanics and Microengineering,* vol. 7, pp. 145-147, 1997.

[66] L. P. Lee and R. Szema, "Inspirations from biological, optics for advanced photonic systems," *Science,* vol. 310, pp. 1148-1150, Nov 2005.

[67] L. J. Guo, "Nanoimprint lithography: Methods and material requirements," *Advanced Materials,* vol. 19, pp. 495-513, Feb 2007.

[68] Y. Xia and G. M. Whitesides, "Soft lithography." vol. 28: Annual Reviews Inc, Palo Alto, CA, USA, 1998, pp. 153-184.

[69] A. C. Arsenault, T. J. Clark, G. Von Freymann, L. Cademartiri, R. Sapienza, J. Bertolotti, E. Vekris, S. Wong, V. Kitaev, I. Manners, R. Z. Wang, S. John, D. Wiersma, and G. A. Ozin, "From colour fingerprinting to the control of photoluminescence in elastic photonic crystals," *Nature Materials,* vol. 5, pp. 179-184, Mar 2006.

[70] W. Park and J. B. Lee, "Mechanically tunable photonic crystal structure," *Applied Physics Letters,* vol. 85, pp. 4845-4847, Nov 2004.

[71] D. Rezzonico, A. Guarino, C. Herzog, M. Jazbinsek, and P. Gunter, "High-finesse laterally coupled organic-inorganic hybrid polymer microring resonators for VLSI photonics," *IEEE Photonics Technology Letters,* vol. 18, pp. 865-867, Mar-Apr 2006.

[72] K. Hoshino and I. Shimoyama, "Analysis of elastic micro optical components under large deformation," *Journal of Micromechanics and Microengineering,* vol. 13, pp. 149-154, 2003.

[73] Y.-C. Tung and K. Kurabayashi, "A nanoimprinted strain-induced reconfigurable polymer micro-optical grating," in *Proceedings of the IEEE International Conference on Micro Electro Mechanical Systems (MEMS)*, Miami Beach, FL, United States, 2005, pp. 243-246.

[74] Y.-C. Tung, S. C. Truxal, and K. Kurabayashi, "Multi-scale soft-lithographic lift-off and grafting (MS-SLLOG) process for active polymer nanophotonic device fabrication," *Proceedings of SPIE - The International Society for Optical Engineering*, Sappora, Japan, 2005, p. 605002.

[75] Y.-C. Tung and K. Kurabayashi, "Nanoimprinted strain-controlled elastomeric gratings for optical wavelength tuning," *Applied Physics Letters,* vol. 86, p. 161113, 2005.

[76] E. Hecht, *Optics*, Third Edition ed. New York: Addison Wesley Longman, Inc., 1998.

[77] S. H. Kong and R. F. Wolffenbuttel, "Spectral performance of a micromachined infrared spectrum analyzer in silicon," *IEEE Transactions on Instrumentation and Measurement,* vol. 54, pp. 264-267, Feb 2005.

[78] M. Born and E. Wolf, *Principles of Optics*, 5 ed. New York: Pergamon, 1975.

[79] M. Golub, A. Friesem, and L. Eisen, "Bragg properties of efficient surface relief gratings in the resonance domain " *Optics Communications,* vol. 235 pp. 261-267, 2004.

[80] N. C. Tien and D. T. McCormick, "MEMS actuators for silicon micro-optical elements," *Proceedings of SPIE, MOEMS and Miniaturized Systems*, Santa Clara, CA, USA, 2000, pp. 256-69.

[81] C. C. Chen and C. Lee, "Design and modeling for comb drive actuator with enlarged static displacement," *Sensors and Actuators A-Physical,* vol. 115, pp. 530-539, Sep 2004.

[82] J. D. Grade, H. Jerman, and T. W. Kenny, "Design of large deflection electrostatic actuators," *Journal of Microelectromechanical Systems,* vol. 12, pp. 335-343, Jun 2003.

[83] R. Legtenberg, A. W. Groeneveld, and M. Elwenspoek, "Comb-drive actuators for large displacements," *Journal of Micromechanics and Microengineering,* vol. 6, pp. 320-329, Sep 1996.

[84] W. Huang and G. Y. Lu, "Analysis of lateral instability of in-plane comb drive MEMS actuators based on a two-dimensional model," *Sensors and Actuators A-Physical,* vol. 113, pp. 78-85, Jun 2004.

[85] G. Y. Zhou and P. Dowd, "Tilted folded-beam suspension for extending the stable travel range of comb-drive actuators," *Journal of Micromechanics and Microengineering,* vol. 13, pp. 178-183, Mar 2003.

[86] R. Frisch-Fay, *Flexible Bars*. Washington D.C.: Butterworth Inc., 1962.

[87] B. T. Chen and J. M. Miao, "Influence of deep RIE tolerances on comb-drive actuator performance," *Journal of Physics D-Applied Physics,* vol. 40, pp. 970-976, Feb 2007.

[88] S. Lee and S. Lee, "Shrinkage ratio of PDMS and its alignment method for the wafer level process," *Microsystem Technologies,* vol. 14, pp. 205-208, 2008.

[89] J. C. McDonald, D. C. Duffy, J. R. Anderson, D. T. Chiu, H. K. Wu, O. J. A. Schueller, and G. M. Whitesides, "Fabrication of microfluidic systems in poly(dimethylsiloxane)," *Electrophoresis,* vol. 21, pp. 27-40, Jan 2000.

[90] M. E. Hawley, D. A. Wrobleski, E. B. Orler, R. Houlton, K. E. Chitanvis, G. W. Brown, and D. E. Hanson, "Mechanical properties and filter distribution as a function of filler content in silica filled PDMS samples," *Mechanical Properties of Nanostructured Materials and Nanocomposites Symposium*, Boston, MA, USA, 2004, pp. 93-8.

[91] D. E. Hanson, M. Hawley, R. Houlton, K. Chitanvis, P. Rae, E. B. Orler, and D. A. Wrobleski, "Stress softening experiments in silica-filled polydimethylsiloxane provide insight into a mechanism for the Mullins effect," *Polymer,* vol. 46, pp. 10989-10995, Nov 2005.

[92] Z. Chen, J. L. Atwood, and Y. W. Mai, "Rate-dependent transition from thermal softening to hardening in elastomers," *Journal of Applied Mechanics-Transactions of the ASME,* vol. 70, pp. 611-612, Jul 2003.

[93] W. V. Mars and A. Fatemi, "Observations of the constitutive response and characterization of filled natural rubber under monotonic and cyclic multiaxial stress states," *Journal of Engineering Materials and Technology-Transactions of the ASME,* vol. 126, pp. 19-28, Jan 2004.

[94] I. M. Ward and D. W. Hadley, *An Introduction to the Mechanical Properties of Solid Polymers*. New York: John Wiley & Sons, 2000.

[95] R. J. Webster, "Minimum Detectable Signal for Spectrogram Displays," *IEEE Transactions on Signal Processing,* vol. 41, pp. 1724-1727, Apr 1993.

[96] M. Davidson and M. Abramowitz, "Introduction to Optical Microscopy, Digital Imaging, and Photomicrography," http://micro.magnet.fsu.edu/primer/index.html, 2008.

[97] T. Nagai, S. Yamada, T. Tominaga, M. Ichikawa, and A. Miyawaki, "Expanded dynamic range of fluorescent indicators for Ca2+ by circularly permuted yellow fluorescent proteins," *Proceedings of the National Academy of Sciences of the United States of America,* vol. 101, pp. 10554-10559, 2004.

[98] A. Miyawaki, J. Llopis, R. Heim, J. M. McCaffery, J. A. Adams, M. Ikura, and R. Y. Tsien, "Fluorescent indicators for Ca2+ based on green fluorescent proteins and calmodulin," *Nature,* vol. 388, pp. 882-887, 1997.

[99] D. T. Dicker, J. M. Lerner, and W. S. El-Deiry, "Hyperspectral image analysis of live cells in various cell cycle stages," *Cell Cycle,* vol. 6, pp. 2563-2570, 2007.

[100] R. A. Schultz, T. Nielsen, J. R. Zavaleta, R. Ruch, R. Wyatt, and H. R. Garner, "Hyperspectral imaging: A novel approach for microscopic analysis," *Cytometry,* vol. 43, pp. 239-247, 2001.

[101] C. X. Luo, Q. Fu, H. Li, L. P. Xu, M. H. Sun, Q. Ouyang, Y. Chen, and H. Ji, "PDMS microfludic device for optical detection of protein immunoassay using gold nanoparticles," *Lab on a Chip,* vol. 5, pp. 726-729, 2005.

[102] R. N. Day, A. Periasamy, M. J. Parry-Hill, A. M. Rainey, and M. W. Davidson, "Förster (Fluorescence) Resonance Energy Transfer with Fluorescent Proteins," http://www.microscopyu.com/tutorials/java/fluorescence/fpfret/index.html, 2008.

[103] Thorlabs, Inc., http://www.thorlabs.com/, 2008.

[104] Hamamatsu Photonics, http://sales.hamamatsu.com/, 2008.

[105] Y.-C. Tung, M. Zhang, C.-T. Lin, K. Kurabayashi, and S. J. Skerlos, "PDMS-based opto-fluidic micro flow cytometer with two-color, multi-angle fluorescence detection capability using PIN photodiodes," *Sensors and Actuators, B: Chemical,* vol. 98, pp. 356-367, 2004.

[106] V. Kapoor, F. V. Subach, V. G. Kozlov, A. Grudinin, V. V. Verkhusha, and W. G. Telford, "New lasers for flow cytometry: filling the gaps," *Nature Methods,* vol. 4, pp. 678-679, 2007.

[107] J. P. Beech and J. O. Tegenfeldt, "Tuneable separation in elastomeric microfluidics devices," *Lab on a Chip,* vol. 8, pp. 657-659, 2008.